The AM Canum Venaticorum Stars

Gijsbert Roelofs

(draft)

Contents

Chapter 1

Introduction

1.1 Compact stars

Stars are all born as objects quite similar to our Sun. They fuse hydrogen into helium in their cores, and the liberated heat provides sufficient outward pressure that the inward pressure due to gravity is balanced. Depending on the mass of the star, this hydrostatic equilibrium can be maintained for millions to billions of years. Inevitably though, the hydrogen fuel runs out and the equilibrium is disturbed.

The hydrogen-exhausted core, unable to provide enough heat to withstand the gravitational pull, will then contract until a new source of pressure is created that can once again hold the star in equilibrium. For sufficiently massive stars, the contracting core becomes hot enough that it starts to fuse helium into carbon and oxygen. The liberated heat then once again provides the necessary outward pressure to counteract gravity.

If helium cannot be ignited, the core continues to contract until the density becomes so high that electron degeneracy pressure becomes strong enough to create a new equilibrium. Degeneracy pressure is a quantum-mechanical effect which is caused by the requirement that two fermionic particles (e.g. two electrons, protons, or neutrons) be distinguishable as separate particles, while obeying Heisenberg's well-known uncertainty principle. The latter states that the uncertainty in the position Δx times the uncertainty in the momentum Δp of a particle be as least

$$\Delta x \Delta p \geq \frac{h}{4\pi} \tag{1.1}$$

where $h = 6.6 \times 10^{-34}$ m^2 kg/s is Planck's constant. In other words, the particles in for instance a star have to be separated by at least $\Delta x = h/4\pi\Delta p$ in order to remain two clearly separate particles. Now the uncertainty in the momentum, which classically is $\Delta p = m\Delta v$, cannot be higher than the value of the momentum itself. Since the velocity of a particle is limited by

the speed of light, the uncertainty in its momentum is likewise limited: $\Delta p_{\max} < mc$. We can thus expect degeneracy pressure to become important when the separation between the particles Δx becomes so small that the particles have to become relativistic at, say, ten per cent of the speed of light: $\Delta p = 0.1mc = 10^{-21}$ kg m/s. In the case of electron degeneracy pressure, this corresponds to a minimum distance between the atoms of $\Delta x = 10^{-12}$ m and thus to a density $\rho \sim 10^9$ kg/m^3 (recall that every electron is associated with one proton and one neutron in for instance helium, carbon and oxygen atoms).

Under normal circumstances, i.e. if the star does not lose its mantle, a shell of burning hydrogen keeps adding helium to the dense, degenerate helium core until the helium ignites after all, lifting the degeneracy in the *helium flash*. Like the more massive stars that ignited helium directly after core hydrogen burning, their source of pressure to balance gravity runs out as the helium in their cores is quickly fused into carbon and oxygen. The majority of stars are not massive enough that they can subsequently ignite their carbon-oxygen cores, so they contract until degeneracy pressure takes over and they end their evolution as a degenerate carbon-oxygen object.

Table 1.1 lists the different types of stars that we know, including their densities. We see that there is a common class of objects that are observed to have such high densities: the *white dwarfs*. They are about as massive as the Sun, but only about as large as the Earth. Since the degeneracy pressure which prevents their further collapse is independent of the temperature, these stars can live forever whilst cooling down slowly.

Only a very small fraction of all stars have masses $M_\star > 8\,M_\odot$. These stars are massive enough that they can fuse elements all the way up to iron, after which it is no longer possible to extract energy from nuclei by fusing elements into heavier ones. Gravitational collapse of the massive iron core is inevitable: it leads to a core-collapse supernova explosion in which the overlaying mantle of the star is ejected into the interstellar medium. If the mass of the collapsing core is not too high, a new equilibrium with the gravitational pull may be reached at extremely high densities due to neutron degeneracy pressure. This is essentially the same story as with the electron degeneracy pressure in the white dwarf stars above: neutrons, when closely packed, repel each another. But since neutrons are about a thousand times heavier than electrons, their Δp can be a thousand times larger and their Δx a thousand times smaller, meaning that they can be packed a thousand times closer together. This means a density that is yet another factor of a billion or so higher than for the white dwarf stars. And indeed, we know of such neutron stars that are about as massive as the Sun, but only as large as the city of Nijmegen (see table 1.1).

If the mass of the star is too high ($M_\star > 20\,M_\odot$) even neutron degeneracy pressure is unable to counteract gravity. Gravity will pull the star together beyond the reach of the observer, in a so-called black hole.

Type of star	Average density (kg/m^3)	Fraction of stars at $t = 13.6$ Gyr
Sun-like	10^3	Most
White dwarf	10^9	Many
Neutron star	10^{17}	Few
Stellar-mass black hole	10^{18}	Fewer

TABLE 1.1: Most ubiquitous stellar objects in the Universe today, all with similar masses of order $1M_\odot \sim 10^{30}$ kg but with quite different densities.

1.2 Accretion in compact binaries

Although neutron stars and black holes are almost invisible by themselves, they make themselves known via *accretion*. When put into orbit with a sufficiently nearby star, matter is drawn from the star to the neutron star or black hole. The strong gravity field around a neutron star or black hole causes a lot of potential energy to be released as heat and we see the neutron star or black hole light up brightly in X-rays (e.g. Prendergast & Burbidge 1968).

Although it would seem rather coincidental that two stars end up so close together that mass is transferred from one to the other, considering that the star nearest to the Sun is several lightyears away, there are a few effects in nature that actually cause this to be quite common. First of all, many stars are born in pairs (binaries). Furthermore, stars tend to change dramatically in size during their evolution. Two Sun-like stars that are initially far apart live their lives as if they were truely alone. But once the more massive of the two has burned up its hydrogen in its core, the core contracts and becomes hotter. The mantle surrounding the core is now subject to a larger temperature gradient between the hotter core and the ouside world: its response is to expand since the conditions for convection put an upper limit to the steepness of the temperature gradient that can be maintained. During this phase the mantle swells up to giant dimensions, causing a hundredfold increase in the radius of the star. All of a sudden, the star that used to be comfortably far away now finds itself engulfed by the mantle of this red giant star.

What happens exactly during this *common-envelope* phase is as yet unknown due to the complicated 3-D hydrodynamical nature of the problem. The large ranges of time and distance scales involved put it outside the reach of current computer simulations. What we do know is that friction between the mantle of the giant and the (still small) other star leads to a loss of mass and angular momentum from the system: the mantle is expelled while the other star spirals in towards the core of the giant star. What is left is a *compact binary*: two stars in an orbit of only a few hours or less (Paczynski, 1976).

Once a binary star has reached such short orbital periods, the gravitational waves that are generated by the orbiting masses start to drive the further evolution of the binary. These waves, which carry away both energy and angular momentum, drive the two detached stars closer together,

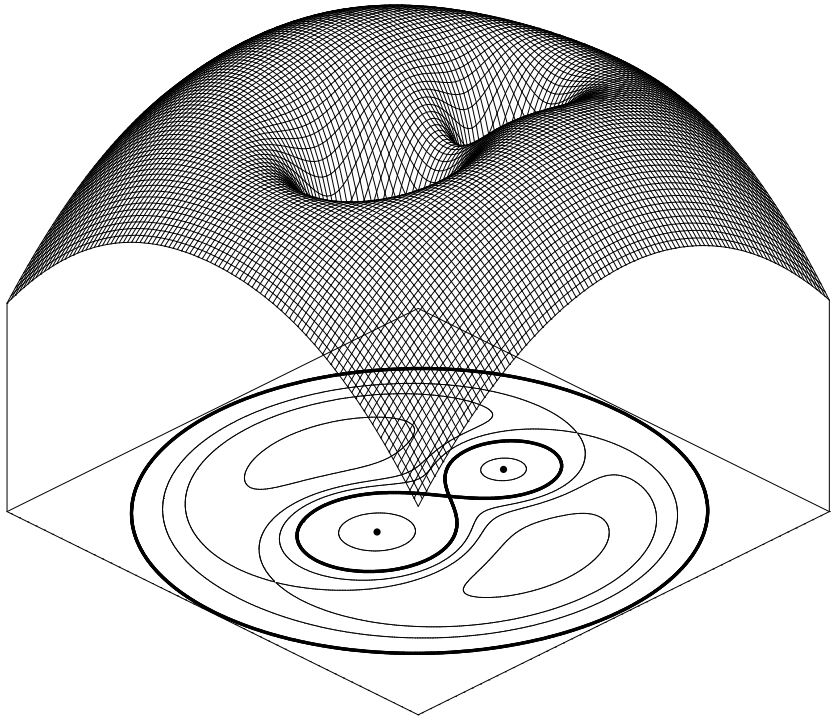

FIGURE 1.1: The gravitational *Roche potential* of two synchronously rotating stars, and the projection of equipotential contours onto the orbital plane. The two 'dips' in the potential surface are caused by the masses of the stars; the outward decrease is due to the centrifugal potential. The saddle point in between the stars is the *inner Lagrange point*; the figure-of-eight shape given by the equipotential contour passing through the inner Lagrange point represents the *Roche lobes*. If one of the two stars becomes too big to fit inside its Roche lobe, mass will flow to the other star at the inner Lagrange point. (Figure by Martin Heemskerk.)

until ultimately they 'touch' and matter starts to flow from one star to the other.

If we draw a picture of the gravitational potential of two stars in synchronous orbits, we see that there is a saddle point between the two stars where the derivative of the potential vanishes, the *inner Lagrange point*. See figure 1.1. If one of the stars is large enough that it extends to this saddle point, the matter at the surface is no longer bound to this particular star but free to flow to the other (so-called *Roche-lobe overflow*). If the other star is a compact object – a white dwarf, neutron star or black hole – the matter flowing through the inner Lagrange point will enter a freefall (Lubow & Shu, 1975) and initially miss the compact object completely due to the deflecting Coriolis force. See figure 1.2. This fictitious force is just conservation of angular momentum in a rotating frame: the matter cannot be accreted by the compact object directly;

instead it will circle the object at a larger orbit corresponding to its specific angular momentum.

In order to be accreted, a particle has to lose angular momentum. Since it is impossible to apply a torque to an almost dimensionless particle, the only solution is that particles share angular momentum with other particles through viscosity. Some particles can then lose angular momentum and be accreted onto the compact object, while others gain angular momentum and move outwards: the matter spreads and an *accretion disc* forms (see figure 1.2).

For the particles making up the outer edge of the accretion disc, there are two options: either leave the binary completely, thereby removing from the system the angular momentum that they carry, or enter a macroscopic non-circular disc configuration to which torques can be applied by the mass-losing star outside the disc. Such a configuration would allow a constant feedback of angular momentum from the particles in the disc to the orbiting stars, and thereby a constant accretion of particles from the inner edge of the disc onto the compact object.

As it turns out, such non-circular discs are observed in many compact accreting binaries, albeit not directly. They are thought to give rise to the *superhump* phenomenon, by which lightcurves of accretion discs show variations on periods a few per cent longer than the orbital period. The traditional picture is that of an elliptical disc that precesses very slowly (and progradely) in the observer's frame, such that the orientation of the two stars with respect to the accretion disc is restored after one orbital period plus a bit due to the presumed slight advancement of the precessing disc over the course of the orbital revolution (Patterson et al., 1993). In this picture, the superhump period is the beat between the orbital period and the precession period of the disc.

Numerical simulations of accretion discs using smoothed-particle hydrodynamics have indicated, however, that this picture of a static, slowly precessing disc is probably not entirely correct: rather, the disc is expected to rapidly change shape over the course of an orbital period, only to return to its 'original' shape after slightly more than one orbital period (Simpson & Wood, 1998). This is probably the correct causal connection between the short orbital and superhump periods and the long 'disc precession' period: the 'precession period' is the beat period between the superhump and orbital periods which are intrinsic to the disc and act on the natural timescale of the binary, namely (approximately) one orbital period.

Either way, however, the predictions are that the disc should be very much non-circular. Existing numerical studies suggest eccentricities of order $e = 0.2$ or more. To test these models I present in chapter 4 a method to measure the level of non-circularity, or eccentricity, of the physical edge of the accretion disc in such a superhump system using a technique called *Doppler tomography*.

1.3 Doppler tomography

Doppler tomography (Marsh & Horne, 1988) is a powerful technique for making two-dimensional images of unresolved ('point') sources, such as compact binaries. At a typical distance of 100 parsecs, and a typical separation of 100,000 km between two white dwarfs in an interacting binary (see figure 1.2), the binary subtends an angle of about 10^{-6} arcseconds

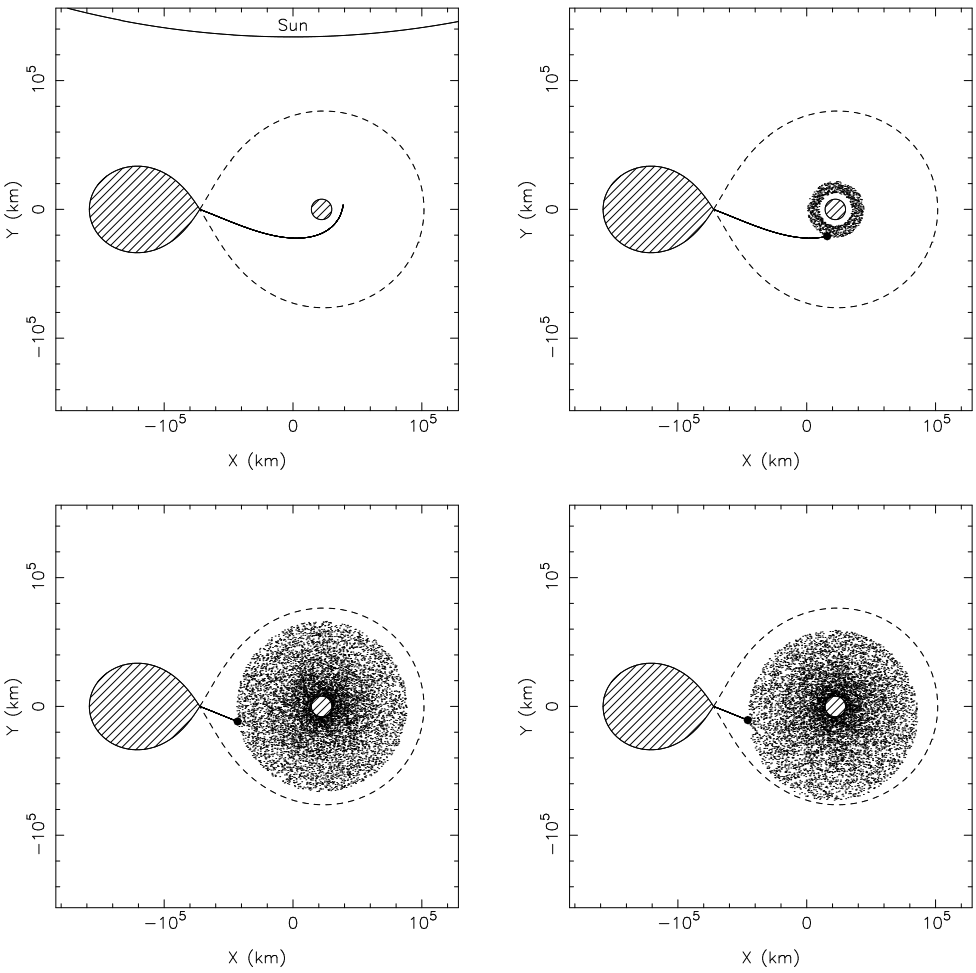

FIGURE 1.2: Disc accretion model. Top left: the donor star (teardrop-shaped) starts to overflow its Roche lobe; matter from the inner Lagrange point goes in freefall towards the accretor. Top right: the matter has too much angular momentum and cannot be accreted directly, but stays in orbit. Bottom left: viscosity transports angular momentum (and particles) outwards, allowing matter on the inside of the disc to lose angular momentum and be accreted. Bottom right: the tidal effect of the donor star can cause the disc to become asymmetric (and variable). The impact of the accretion stream into the edge of the disc (black dot) is often observed as a 'bright spot' in interacting binaries, presumably due to enhanced dissipation in this region.

on the sky. The sharpest images taken with the *Hubble Space Telescope*, or using adaptive optics on for instance the Very Large Telescope, have an angular resolution of worse than 10^{-2} arcseconds. We therefore have to resort to indirect imaging techniques to produce resolved images of such systems.

Two such techniques were developed in the 1980s: *eclipse mapping* (Horne, 1985) and *Doppler tomography* (Marsh & Horne, 1988). Eclipse mapping relies on the observer being in the orbital plane of a binary star, so that once every orbital period the stars are aligned with the observer. As the mass-losing star moves in front of the accreting star and the accretion disc, it obscures variable parts of the disc and accretor, causing variations in the intensity of the light (and as a function of wavelength) that reaches Earth. With the proper inversion algorithm, a spatial reconstruction of the accretion disc and the accretor can be made from these variations.

The disadvantage of eclipse mapping is that it relies on eclipses, which most interacting binaries do not exhibit. What is common to all binary stars, however, is that they rotate and therefore that light from a certain region in the system is redshifted and blueshifted by variable amounts during the course of an orbital revolution. Doppler tomography uses this information to reconstruct an image of the accreting binary star, albeit not in spatial coordinates but in velocity coordinates. Figure 1.3 shows how this works: a series of spectra taken at different orbital phases are projected onto a two-dimensional map in velocity coordinates. Emission features that are fixed in the binary frame, such as those shown in the example, add up constructively at their true radial velocities and phases in the Doppler map, while their signals are diluted at other radial velocities and phases in the map.

Although it is basically just an alternative representation of data, a Doppler tomogram is very convenient for measuring radial velocity amplitudes and phases of emission regions in a binary star, which allows one to derive important parameters such as the mass ratio of the binary. Especially in data with poor signal-to-noise ratios or complicated spectral line profiles, back-projection of time-series spectra in a Doppler tomogram is often necessary for accurately measuring radial velocity amplitudes and phases in binary stars and deducing physical parameters from them. In this thesis I make extensive use of the Doppler tomography technique to derive physical parameters of the rare, ultracompact *AM CVn binaries* in chapters 2, 3, 4 and 6.

1.4 The AM Canum Venaticorum stars

The specific type of objects studied in this thesis are the AM Canum Venaticorum stars. Variable star number AM in the constellation Canes Venatici, the Hunting Dogs, was first catalogued as a faint blue star by Humason & Zwicky (1947) under the name 'HZ 29'. Its spectrum showed exclusively helium absorption lines, whose peculiar broad and shallow shape could not readily be explained, earning it the classification as 'peculiar DB (=helium atmosphere) white dwarf' (Greenstein & Matthews, 1957).

The detection of 18-minute variations in the lightcurve of AM CVn (Smak, 1967) supported the picture that AM CVn is an ultracompact binary star consisting of two degenerate objects.

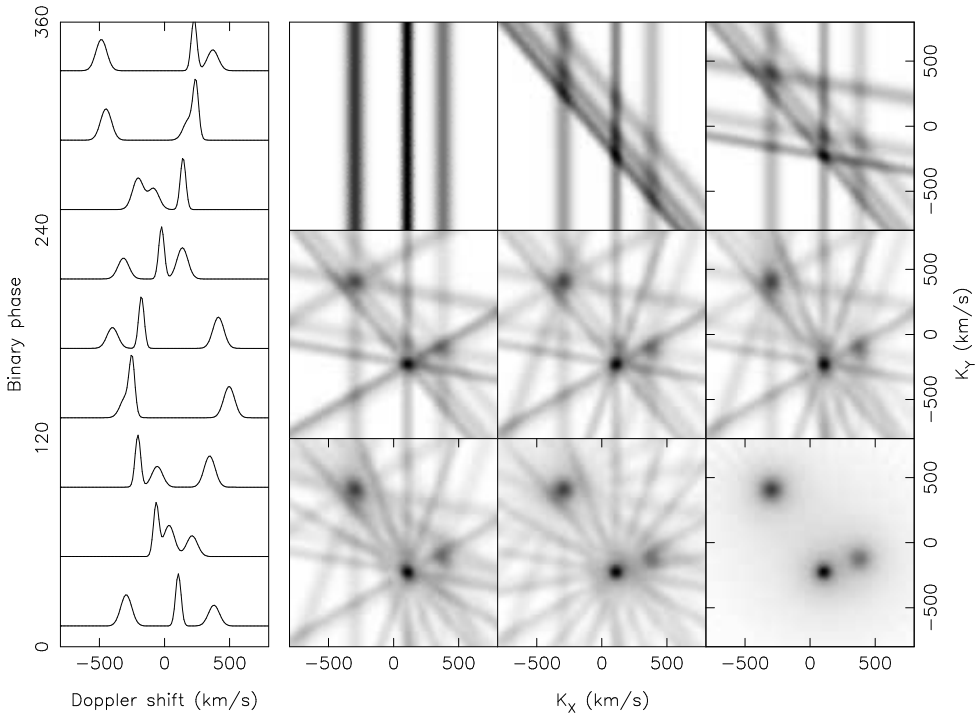

FIGURE 1.3: Back-projection of spectra in a Doppler tomogram. To the left is a series of spectra taken as a function of orbital phase, each containing intensity versus wavelength (where the latter has been converted to Doppler shift). These are projected one by one onto a two-dimensional velocity map; the bottom spectrum at phase zero is projected onto the top left Doppler map. In the top middle map, the second spectrum is added at the angle given by its phase, and so forth. If one has about twice as many phase bins as resolution elements across the Doppler map, the artefacts vanish and one ends up with a clean two-dimensional reconstruction of the emission regions in the binary system, in velocity coordinates denoted K_X and K_Y. This is shown in the bottom right map, which was reconstructed from 31 phase bins.

However the picture of AM CVn as a mass-transferring binary was first proposed by (Warner & Robinson, 1972) when they discovered rapid 'flickering' in lightcurves of AM CVn, which is thought to be directly related to the accretion of clumpy matter from the inner accretion disc onto the white dwarf. In hindsight, the fast variations were probably completely unrelated to flickering (Warner, private communication) but the suggestion that AM CVn is an interacting binary was correct.

A long discussion as to the true orbital period of AM CVn ensued, fed by the many different periodicities found in AM CVn's lightcurves (Solheim et al., 1998; Harvey et al., 1998; Provencal et al., 1995; Patterson et al., 1993, 1992). In the meantime, several stars were discovered that shared some of the properties of AM CVn: GP Com, an apparent peculiar white dwarf showing exclusively helium emission lines (Burbidge & Strittmatter, 1971) and a 46-minute orbital period (Nather et al., 1981); CR Boo, an object that apparently moved between bright, AM CVn-like and faint, GP Com-like states and displayed photometric variability on periods of about 25 minutes (Wood et al., 1987); and V803 Cen, a similar variable with 27-minute oscillations (O'Donoghue et al., 1987).

Convincing evidence for the binary nature of AM CVn and for its true orbital period was obtained only as recently as 2001 from Doppler tomography, which revealed the 'bright spot': the common hallmark of accretion in binary stars, associated with the free-falling stream of matter from the donor star crashing into the edge of the accretion disc (figure 1.2; Nelemans et al. 2001). The dominant photometric periods in AM CVn, which were consistently longer than the orbital period by about 2%, are thus thought to be associated with the superhump phenomenon (section 1.2).

1.5 Binary evolution of AM CVn stars

The theory of the evolution of binary stars progressed rapidly in the last few decades of the twentieth century, as more and more exotic interacting binary stars were discovered using state-of-the-art telescopes and instruments. For the AM CVn stars, three theoretical formation channels have been proposed. In all cases the accretor is a white dwarf, but the nature of the donor star at the onset of Roche-lobe overflow is quite different in the three proposed channels.

In the first formation channel, the 'white dwarf channel' (e.g. Nather et al. 1981; Tutukov & Yungelson 1996; Nelemans et al. 2001), the donor star evolves to a low-mass helium white dwarf through a common-envelope phase. Gravitational-wave radiation drives the resulting pair of white dwarfs closer together until the less massive helium white dwarf overflows its Roche lobe. Since mass is flowing from the lighter to the heavier star, and is thus moving closer to the centre-of-mass, conservation of angular momentum implies that the binary should widen. The mass loss thus counteracts the gravitational-wave radiation that drives the two stars closer together. Depending on the donor star's response to the mass loss, an equilibrium is reached in which the mass transfer rate is at all times proportional to the angular momentum losses due to the emission of gravitational waves. Degenerate stars become larger upon mass loss, so that

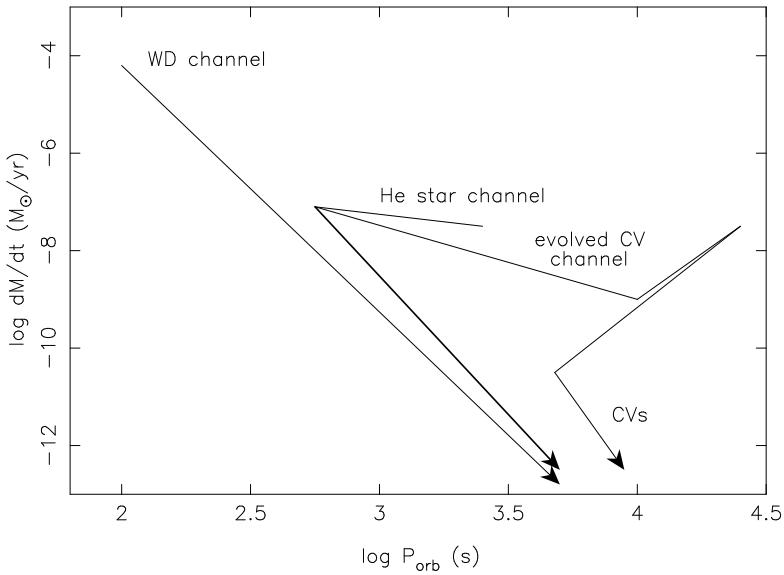

FIGURE 1.4: Schematic evolution of the mass transfer rate and the orbital period in the proposed white dwarf (WD) channel, the helium (He) star channel, and the evolved-Cataclysmic-Variable (evolved-CV) channel. Binaries with a normal, hydrogen-rich star, such as the Cataclysmic Variables shown on the right, cannot reach orbital periods below about 80 minutes because their average densities are too low to fit in a more compact configuration. Binary stars that do reach shorter orbital periods are therefore called *ultracompact binaries*. (Figure after Nelemans 2005.)

in the case of two white dwarfs an equilibrium can only be reached in a widening binary. After Roche-lobe overflow has commenced the two white dwarfs evolve indefinitely towards larger separations, i.e. towards longer orbital periods.

In the second formation channel, the 'helium star channel' (e.g. Tutukov & Fedorova 1989; Iben & Tutukov 1991; Nelemans et al. 2001), the donor star upon Roche-lobe overflow is a non-degenerate helium star. It is formed in a second common-envelope phase, like in the white dwarf channel, but the difference is that the core of its progenitor star was massive enough to ignite helium. After ejection of this progenitor's hydrogen (common-)envelope one is thus left with a non-degenerate helium star orbiting the white dwarf. Gravitational waves again push the two stars together, and Roche-lobe overflow inevitably starts from the relatively large helium star to the white dwarf. Since the non-degenerate helium star becomes smaller as it loses mass, equilibrium between gravitational-wave radiation and mass transfer is reached in a binary of shrinking orbit. But as always, the nuclear burning inevitably stops. In the case of a mass-losing helium star it is not so much the helium fuel running out; rather, the mass loss from the surface causes the temperature and pressure in the star's core to decrease, which slows down the fusion reaction dramatically. The heat production decreases enough that after the helium star has been

stripped to $0.2 M_{\odot}$, degeneracy pressure becomes an important pressure source. The helium star becomes *semi-degenerate*: its radius now starts to increase upon mass loss, which means that the further evolution of the binary has to be one of ever-increasing orbital separation. At this point the binary is expected to look very similar to a binary produced in the white dwarf channel.

In the third, and so far last proposed formation channel (Podsiadlowski et al., 2003), the 'evolved-Cataclysmic-Variable channel', the donor star upon Roche-lobe overflow is a slightly evolved, hydrogen-burning star. It would thus initially look like a normal hydrogen-rich Cataclysmic Variable. If properly fine-tuned however, a high level of hydrogen depletion can be reached in the core of the donor star. When the mass loss has progressed all the way to the helium-rich core of the donor star (which by now has become degenerate, since helium burning never started), the binary once again starts to evolve towards longer orbital periods and, depending on the level of hydrogen depletion, it may look similar to a binary produced in the above two channels.

Figure 1.4 shows a graphical representation of the three proposed evolutionary scenarios in terms of the orbital periods and the mass transfer rates. Despite the progress in theoretical models of how to make such AM CVn stars, there are a few long-standing questions:

1. Which of these proposed formation channels contribute to the AM CVn population? – and –
2. How many AM CVn stars do these formation channels actually produce?

These are the two most important questions I try to answer in this thesis. Underlying are several open questions in binary evolution theory, such as how the elusive common-envelope exactly works, and what is the stability criterion for mass transfer between white dwarfs. The most important results are concentrated in chapters 4, 5 and 8.

1.6 Gravitational waves

Gravity is one of at least four fundamental forces in nature. The gravitational force has many analogies with the electromagnetic force, by which electrically charged bodies attract or repel one another. It is clear that two such charged bodies in different places can only be attracted to one another if they somehow communicate their existence to each other. In other words, the charges need to send out messenger particles to spread the word of their existence. We know these messenger particles, and we see them every day: photons, or in other words, light waves.

The same is expected for the gravitational force: there should be messenger particles that communicate to the Universe that there is a large mass somewhere that we should be attracted to. And one of the intrinsic properties of such messenger particles is that they can be detected. However, the gravitational force is very weak: one needs a large mass (or 'charge') to get a strong attraction. The *gravitational waves* are thus expected to be very weak and much more difficult to detect than their electromagnetic counterparts, the light waves, which after all can be seen

with the naked eye. This is the reason that they have not yet been detected directly, even though their existence has been deduced from indirect effects such as their ability to change the orbital period of two stars (Hulse & Taylor, 1975), as mentioned above.

An extremely sensitive instrument has been proposed by NASA and ESA to detect and measure gravitational waves directly: the *Laser Interferometer Space Antenna*, or *LISA*. It will be able to measure gravitational waves with frequencies in the millihertz regime. In order to produce such gravitational waves, i.e. waves with frequencies of 10^{-3} Hz, one needs a gravitational system with a certain density. Kepler's well-known third law tells us that in order to make a gravitational system with frequency f (in Hz), one needs a system density ρ (in kg/m^3) of

$$f^2 = \frac{1}{P^2} = \frac{G}{4\pi}\frac{M+m}{a^3} = 10^{-12}\rho. \tag{1.2}$$

To produce gravitational waves with frequency $f = 10^{-3}$ Hz, one thus needs an average system density $\rho = 10^6$ kg/m^3. It is then a matter of looking at table 1.1 to see which objects are going to be the best candidates for detection with *LISA*. Normal Sun-like stars are the most ubiquitous objects in our Universe, but their densities fall short by quite a large factor. The next-most important group of objects are the white dwarfs, and we see that their densities are high enough that they can form gravitational systems with the right density that can produce gravitational waves with the right frequencies! Compact binary stars with two white dwarfs in orbit, such as the AM CVn stars, are thus expected to be the most ubiquitous *LISA* sources. In chapters 4 and 5 of this thesis I give the expected gravitational-wave signals of four AM CVn stars and show that they are the first good candidates for detection with *LISA*.

If *LISA* works as planned, it will be able to see things that are impossible to see in light waves. Unhindered by light-absorbing dust and gas in our Galaxy, *LISA* will be able to see white dwarf binaries throughout the Galaxy, and most importantly: the *LISA* sample will be *complete* at orbital period below about ten minutes. Such a valuable sample would be impossible to obtain from light waves.

Chapter 2

SDSS J124058.03−015919.2: A new AM CVn star with a 37-minute orbital period

G. H. A. Roelofs, P. J. Groot, T. R. Marsh, D. Steeghs, S. Barros and G. Nelemans

MNRAS, 361, 487 (2005)

Abstract. We present high time resolution VLT spectroscopy of SDSS J124058.03−015919.2, a new helium-transferring binary star identified in the Sloan Digital Sky Survey. We measure an orbital period of 37.355 ± 0.002 minutes, confirming the AM CVn nature of the system. From the velocity amplitudes of the accretor and the accretion stream–disc impact, we derive a mass ratio $q = 0.039 \pm 0.010$. Our spectral coverage extends from $\lambda\lambda$3700–9500Å and shows the presence of helium, nitrogen, silicon and iron in the accretion disc, plus the redshifted, low-velocity "central spikes" in the helium lines, known from the low-state AM CVn stars GP Com and CE 315. Doppler tomography of the helium and silicon emission lines reveals an unusual pattern of two bright emission sites in the tomograms, instead of the usual one emission site identified with the impact of the mass stream into the accretion disc. One of the two is preferred as the conventional stream–disc impact point in velocity space, at the 3σ confidence level. We speculate briefly on the origin of the second.

2.1 Introduction

The AM CVn stars are thought to be white dwarfs accreting helium from another low-mass helium white dwarf (e.g. Nelemans et al., 2001), a semi-degenerate low-mass helium star (Iben & Tutukov, 1991) or, possibly, from an initially hydrogen-rich evolved-main-sequence star (Podsiadlowski et al., 2003). Their observed orbital periods range from 65 down to 10 or possibly even 5.3 minutes (Ruiz et al., 2001; Warner & Woudt, 2002; Ramsay et al., 2002; Israel et al., 2002). Their evolution is expected to be governed entirely by loss of angular momentum through emission of gravitational wave radiation (GWR) (Paczynski, 1967). Once mass transfer has started, the mass transfer rate is determined by the loss of angular momentum from the orbit due to GWR. The mass transfer in turn determines the increase in orbital period. Since the rate of angular momentum loss due to GWR is a sensitive function of binary separation (Landau & Lifschitz, 1971), an exponential decline in mass transfer rate and orbital frequency will ensue.

The small sample of about ten known systems seems to conform to this picture rather well. It can be divided in three groups of different optical signature: (1) the short-period, high-state systems, that are believed to be in a stable state of high mass transfer. Their optical spectra are dominated by helium absorption lines, probably from the (optically thick) accretion disc; (2) the longest-period, low-state systems that are believed to be in a stable state of low mass transfer. Their optical spectra are dominated by strong helium emission lines from the (optically thin) accretion disc plus an underlying blackbody, attributed to the accreting primary white dwarf, and (3) the intermediate-period outbursting systems, whose optical signature more or less varies between that of the high and that of the low state systems, accompanied by variations in brightness of several magnitudes.

Unfortunately, it is as yet unknown which of the three suggested formation channels contribute to the AM CVn population, and in what numbers. In order to improve our overview of the population, and in particular to test its homogeneity, we started various searches for these objects. This included a search in the spectroscopic database of the Sloan Digital Sky Survey (SDSS), from which we extracted AM CVn candidates by filtering out helium emission line systems. This resulted in the discovery of SDSS J124058.03−015919.2 (hereafter SDSS J1240): a faint ($V = 19.7$) but obvious mass-transferring binary with its characteristic strong, broad helium emission lines giving away the presence of an accretion disc (Roelofs et al., 2004).

In addition to the helium emission, the object shows a characteristic DB white dwarf continuum with broad helium absorption lines, which fits well with a single 17,000 K blackbody (Roelofs et al., 2004). Recent work by Bildsten et al. (in preparation) predicts that the evolution of these systems towards longer orbital periods goes hand in hand with a continuous cooling of the accretor, which is ultimately due to the plummeting accretion rate. GP Com, which has an orbital period of 46 minutes, shows a continuum which is compatible with a ∼11,000 K blackbody, which Bildsten et al. attribute to the accreting white dwarf. The accretor in the new system appears to be considerably hotter, suggestive of a higher mass transfer rate. An inventory of previous observations of the new AM CVn star (see table 2.1) shows that it has been observed on quite a few occasions, where it was always close to $V = 19.7$, suggestive of a somewhat lower

Dates	Survey/reference or observer	Type
1979/05/19	SSS/DSS1	image
1991/05/05	SSS/DSS2	image
1999/03/12	2QZ	spectrum
2000/03/03	SDSS	image
2001/03/31	SDSS	spectrum
2003/12/12,13	Roelofs et al. (2004)	spectrum
2004/02/14,16,19–21	Woudt & Warner (2004)	photometry
2004/02/17	Ramsay & Hakala	photometry
2004/12/17,18,19,30	Roelofs	image

TABLE 2.1: Summary of previous (serendipitous) observations of the new AM CVn star. On all occasions, the star was close to $V = 19.7$. (SSS = SuperCOSMOS Sky Survey; DSS = Digitised Sky Survey; 2QZ = 2-degree Field QSO Redshift Survey).

mass transfer rate than that of the longest-period outbursting AM CVn star, 'SN2003aw' at ∼34 minutes (Woudt & Warner 2003 and Roelofs et al. in prep.), although the observations do not rule out that the star exhibits outbursts just as well as 'SN2003aw'.

A first attempt to measure the orbital period of the new AM CVn candidate was carried out by Woudt & Warner (2004) at the South African Astronomical Observatory through white-light photometry. However, no periodic modulation of the object's brightness was detected. A similar time-series taken independently by Ramsay & Hakala (private communication) on the Nordic Optical Telescope gave the same results. Photometrically, SDSS J1240 thus behaves just like the two low-state AM CVn stars GP Com and CE 315 (Woudt & Warner, 2002). To uncover the orbital period of SDSS J1240, as well as probe the basic kinematics of the system, we obtained time-resolved spectroscopy.

2.2 Observations and data reduction

We obtained phase-resolved spectroscopy of SDSS J1240 during March, April and May of 2004 on the Very Large Telescope of the European Southern Observatory with the FORS2 spectrograph. The largest part of the observations consists of 338 high time and spectral resolution spectra in the red (grism 1200R, effective resolution ∼2–3Å depending on seeing conditions) with the aim of carrying out Doppler tomography on the strong helium emission lines in the red, to measure beyond doubt the orbital period of the binary. We furthermore obtained a series of 16 lower-resolution spectra in the blue and 6 spectra in the far-red (grisms 600B and 600I, resolution ∼6Å). Our spectral coverage thus extends from $\lambda\lambda$3800–9500Å. A summary of the observations is given in table 2.2.

Date	UT	Exposure time (s)	Exposures
FORS2/600B			
2004/03/18	06:37–07:48	240	16
FORS2/600I			
2004/03/19	07:56–08:24	300	6
FORS2/1200R			
2004/04/19	04:08–05:01	90	22
2004/04/20	00:41–01:34	90	22
	04:27–06:12	90	44
2004/05/10	23:16–01:13	90	44
2004/05/11	01:56–02:53	90	23
2004/05/13	23:23–04:06	90	114
2004/05/17	23:08–02:07	90	69

TABLE 2.2: Summary of our VLT observations. 600B, 600I and 1200R denote the FORS2 grisms used in the set-up.

All observations were done with a $1''$ slit. The detector was the FORS2 MIT CCD mosaic of which only chip 1 was used; binning was standard 2×2 pixels. Low read-out speed and high gain minimized the read-out and digitisation noise, respectively. In order not to add more noise to the spectra, we subtracted a constant bias level from the CCD frames. The bias level was determined per observing block of typically 22 spectra from the overscan regions on the CCD. A normalised flatfield frame was constructed from 5 incandescent lamp flatfield frames each night, which ensured a cosmic-ray-free final flatfield. For the observations taken with the 1200R grism, we used the combined flatfields taken 2004/04/19, 2004/05/10 and 2004/05/13 for all observations as suitable flatfield frames were not available for the other three nights.

All spectra were extracted using IRAF's implementation of optimal (variance-weighted) extraction. The read-out noise and photon gain, necessary for the extraction, were calculated from the bias and flatfield frames, respectively. Wavelength calibration was done with standard HeHgCd and HeNeAr arcs for the 600B and 600I spectra, respectively. A total of around 40 arc lines could be fitted well with a cubic spline of order 1 and 0.14 Å root-mean-square residual. The 1200R spectra, taken on different nights, were calibrated per observing block using 42 night sky lines, which were selected to minimize the possibilities of blending or confusion. We thus achieved a good fit on 42 sky lines, again with a cubic spline of order 1, and 0.064 ± 0.015 Å root-mean-square residuals. All spectra were transformed to the heliocentric rest-frame prior to analysis.

The red average spectrum of SDSS J1240 was corrected for instrumental response using spectroscopic standard star EG 274. For the blue and far-red spectra, the instrumental response was removed using the flux-calibrated spectrum of SDSS J1240 from the Sloan Digital Sky Survey

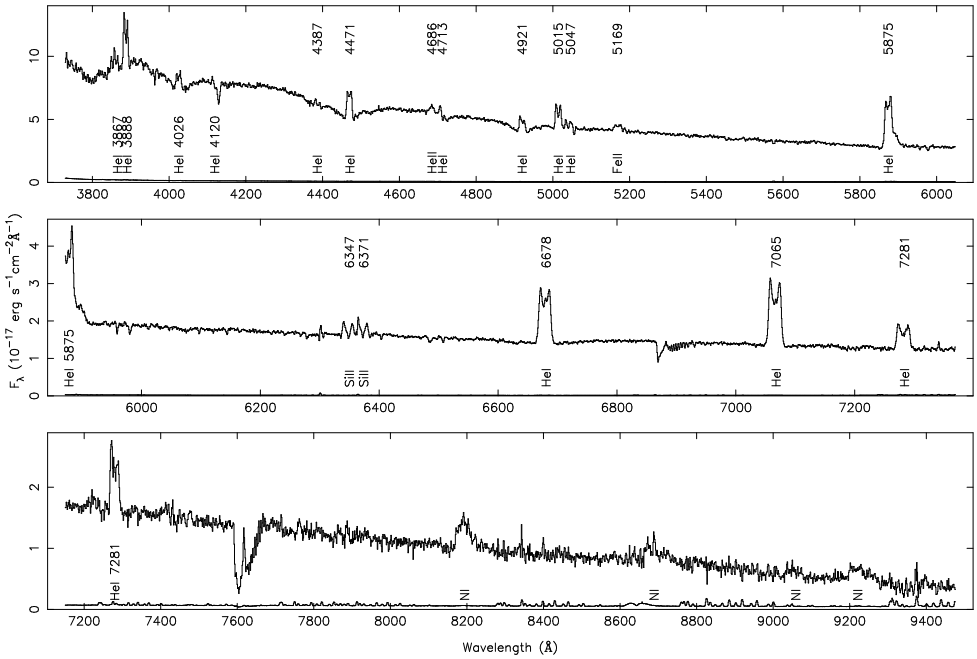

Figure 2.1: Average spectra of SDSS J1240 with the 600B, 1200R and 600I grisms, top to bottom. The most prominent lines are labelled.

as a suitable flux standard was not available. In this paper, the flux calibration is mainly intended to show the continuum slope of the spectrum.

2.3 Results

2.3.1 Average spectrum

The average spectra in the blue, red and far-red are shown in figure 2.1. The blue spectrum shows the familiar double-peaked helium emission lines and the aforementioned broad DB white dwarf absorption lines. In the far-red, we notice several N I line complexes, which are quite similar to those seen in GP Com (e.g. Morales-Rueda et al., 2003) and CE 315 (Ruiz et al., 2001). Both the blue and the red spectra, however, reveal features which clearly distinguish SDSS J1240 from GP Com and CE 315, namely strong Si II emission at λ6346Å and λ6371Å, as well as Fe II emission at λ5169Å. These silicon features have also been observed in a low-state spectrum of CP Eri (Groot et al., 2001), after model predictions by Marsh et al. (1991) that they should show up in an optically thin helium accretion disc with solar abundances of heavy metals.

Line	$\gamma_{\rm disc}$ (km/s)	$\gamma_{\rm cs} - \bar{\gamma}_{\rm disc}$ (km/s)	K_Y (km/s)	K_X (km/s)
He I 5876	–	28.4±4.2	-17.8 ± 5.3	5.6 ± 5.3
He I 6678	35.5±1.7	31.5±4.2	-20.8 ± 5.1	1.3 ± 5.1
He I 7065	33.1±1.9	55.0±4.2	-10.2 ± 4.7	-5.6 ± 4.7

TABLE 2.3: Parameters for three helium lines showing a central spike: the systemic velocity as derived from the wings of the lines ($\gamma_{\rm disc}$), the intrinsic redshifts of the central spikes relative to the average systemic redshift ($\gamma_{\rm cs} - \bar{\gamma}_{\rm disc}$), and the velocities of the central spikes (K_X and K_Y) for the orbital ephemeris (2.1).

A second striking feature seen in the red spectrum, which has the largest signal-to-noise ratio and the highest spectral resolution, is the central emission in the double-winged helium emission lines (see figure 2.3 in section 2.3.3 for a close-up). This "central spike" feature was first seen in GP Com (Smak, 1975) and observed with the discovery of the second low-state AM CVn star, CE 315 (Ruiz et al., 2001). However, in SDSS J1240 it is considerably weaker than in the other two systems. Its origin is reported to be most likely on or very near the accreting white dwarf, based on a small but clearly detected movement of the central spike in both GP Com and CE 315, consistent in phase and amplitude with the accretor's orbital motion (Marsh 1999, Morales-Rueda et al. 2003, Steeghs et al. in prep.).

2.3.2 The spectroscopic period

To find the spectroscopic period, we used a slightly modified version of the method described by Nather et al. (1981). The emission lines are divided into a red and blue part and the ratio of fluxes in both wings – summed over all emission lines to maximize the signal-to-noise – is calculated for each spectrum. In order to minimize the effects of CCD pixels falling just inside a wing mask for one spectrum, but just outside the wing mask for another due to small differences in the dispersion solution, we used masks with "soft edges" to calculate the red-wing and blue-wing fluxes. The edges of a mask fall off as a Gaussian which has a width matched to the spectral resolution of the set-up.

A Lomb–Scargle periodogram of the measured red-wing/blue-wing ratios as a function of heliocentric Julian date is shown in figure 2.2. A clear signal is seen at around 38 cycles/day; a weaker group of peaks appears at three times this frequency. Zooming in on the main signal, we see that the strongest peak occurs at 38.546 cycles/day ($P = 37.36$ minutes), with the two next-strongest peaks occurring at the usual ± 1 cycle/day aliases. We will assume that the strongest peak corresponds to the orbital period of the binary. We will refine our orbital period measurement using the emission line kinematics in the next section.

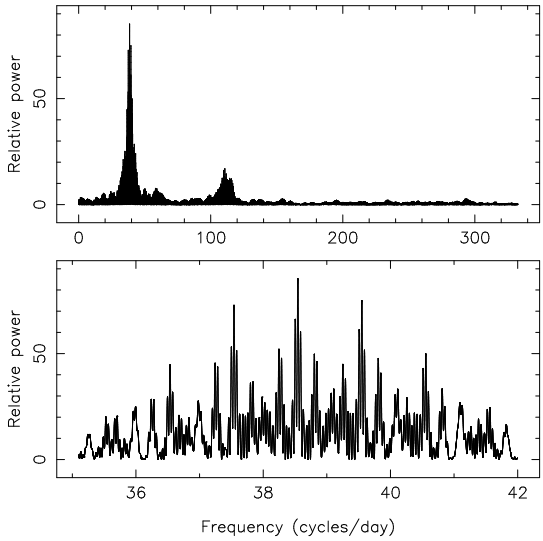

Figure 2.2: Lomb-Scargle periodogram of the red wing/blue wing flux ratios. The lower panel provides a magnified view of the strongest peaks.

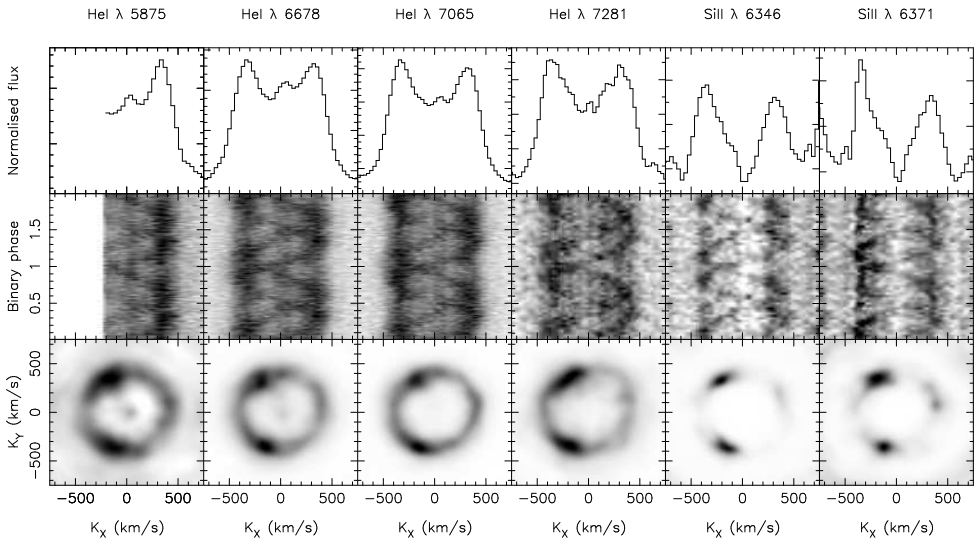

Figure 2.3: Trailed spectra and Doppler tomograms of the R-band He i and Si ii features. A pattern of two bright spots, at approximately the same radial velocity but at a 120 degree angle, appears in the trails and tomograms. The central spikes are clearly visible in the trailed spectra of He i 5875, He i 6678 and He i 7065. The possible central spike feature in the He i 7281 line is strongly affected by night sky lines.

2.3.3 Doppler tomography

Features of the accretion disc

Usually, a Doppler tomogram of a binary in which accretion via an accretion disc occurs, shows one bright emission site that can been attributed to the impact point of the accretion stream into the accretion disc. Both the helium and silicon emission line tomograms in SDSS J1240 show an unusual pattern of two bright spots at approximately the same radial velocity of 390±10 km/s, and at approximately the same intensity. This feature is also clearly identified in the trailed spectra. See figure 2.3 for trailed spectra and maximum-entropy Doppler tomograms of all emission lines in the red.

In the trailed spectra of He I 5875, He I 6678 and He I 7065 as well as in the Doppler tomograms of He I 5875 and He I 6678 we can furthermore distinguish the (rather weak) central spike, at near-zero velocities. Note that the intrinsic redshifts of the central spikes, as summarised in table 2.3 but also clearly visible in the trailed spectra, causes them to be smeared out in the Doppler tomograms since these have been made using the rest-frame wavelengths of the helium lines. Therefore the central spikes do not show up as clearly as would be expected from the trailed spectra.

The double bright spot pattern, which persists even in Doppler tomograms made from a single night's data, was used to further refine the orbital period by aligning the bright spot patterns in the tomograms from each night. After correcting for the systemic velocity of the star, we derive an orbital period $P_{\rm orb} = 37.355 \pm 0.002$ minutes. The error is determined by the time-base of our observations and the notion that a phase drift of $P_{\rm orb}/20$ over this time-base clearly shows up in the Doppler tomograms.

Redshift and movement of the central spike

Detailed studies of the central spike in GP Com and CE 315 (Marsh, 1999; Morales-Rueda et al., 2003) have shown that it is most likely produced on or very near the accreting white dwarf. The origin of the line-dependent intrinsic redshifts observed in the central spikes of GP Com and CE 315 is still unclear and will be the subject of a separate study (Steeghs et al. in prep.). The main problem with the redshifts of the central spike is that it is significantly different for each helium line, which makes it difficult to explain the redshifts as being caused by just the gravitational field of the primary white dwarf. Due to the lower spectral resolution, lower signal-to-noise, more complicated line profiles, and weaker central spikes, the same approach as taken by Morales-Rueda et al. (2003) for measuring the central spikes' redshifts in GP Com does not work for the data presented here. Instead of fitting multiple Gaussians to phase-binned spectra, we auto-correlate all spectra simultaneously via linear back-projection Doppler tomography (Marsh & Horne, 1988). We use the fact that, for a given trial wavelength, an emission feature in the spectra will appear blurred in a Doppler tomogram if its intrinsic "rest" wavelength does not coincide with the trial frequency. We thus make linear back-projection Doppler tomograms for a range of trial wavelengths around the rest-frame wavelengths of the

three neutral helium lines showing a central spike, and fit a 2-D Gaussian to the central spike in every back-projection. For each line, the height (i.e., the sharpness) of the fitted central spike peaks strongly around a certain (redshifted) wavelength which we define as the "rest" wavelength of the central spike. The results are summarised in table 2.3.

Once we have the redshifts of the central spike, we can look for the location of the central spikes in the velocity space of their Doppler tomograms, which should reflect the orbital motion of the primary white dwarf if we assume that the central spike is indeed produced on or near the primary white dwarf. Measuring the central spike's movement thus allows us to (a) determine the zero phase in the orbital ephemeris, and (b) constrain the mass ratio of the system from the ratio of velocities of the central spike and the bright spot. To further optimise the signal-to-noise we fit a 2-D Gaussian to the combined back-projections of all three helium lines showing a central spike, where the central spikes' centre wavelengths that we just determined are taken as the "rest" (zero-velocity) wavelengths.

Fitting a 2-D Gaussian to the central spike in a back-projection requires separating the low-velocity spike from the higher-velocity asymmetric accretion disc emission, which may cause gradients that shift the peak of the central spike. We assume that the background gradients in the central spike region of the back-projection are caused by high-velocity emission sites (e.g., the bright spots) that blurr into the low-velocity spike region, such that we can estimate the background gradients at radial velocities below, say, 100 km/s by considering the intensity at the $\sqrt{K_X^2 + K_Y^2} = 100$ km/s boundary. We then interpolate the background underneath the central spike by solving Laplace's equation for the intensities of the pixels in the inner region of the back-projection given the intensities ("potential") along the boundary.

The exact choice of boundary is arbitrary; reasonable values are 100–150 km/s, given the central spike's width of about 40 km/s and the strong accretion disc emission peaking around 400 km/s. When determining the central spikes' redshifts, we varied the boundary radius between 100–150 km/s to estimate the uncertainties on the redshifts as shown in table 2.3.

The uncertainty on the central spike's velocity as obtained from the 2-D Gaussian fit is determined with a simple Monte Carlo simulation. We follow the procedure above for a large number of Doppler tomograms in which we set random phases on all spectra. One then expects the central spike to be smeared out (slightly) around $K_X = K_Y = 0$ in each random tomogram. A 2-D Gaussian fit to such a randomised central spike should thus lie at $K_X = K_Y = 0$; the deviations from this expected value give us an estimate of the uncertainty in our measurement. After fitting all the randomised central spikes, we fit a 2-D Gaussian to the distribution of scatter around $K_X = K_Y = 0$. This fits well with $\chi^2/\text{n.d.f} \approx 1$. The radial width of this Gaussian is taken as the 1-σ accuracy of our central spike velocity measurement. The results for the central spike and its corresponding error turn out to be insensitive to the exact choice of the background boundary radius in the range 100–150 km/s. For radii smaller than 100 km/s and for radii larger than 150 km/s, the scatter in the fits to the random tomograms increases.

Using this method, we obtain a central spike velocity of 15.3 ± 4.6 km/s. By aligning the central spike along the negative K_Y axis, which is where the primary white dwarf should be, we obtain the zero phase in the ephemeris of SDSS J1240. With the spectroscopic period found above,

the full orbital ephemeris then becomes

$$T_0(\mathrm{HJD}) = 2453115.6599 + 0.025944E \tag{2.1}$$

As a further sanity check on the significance of the determined central spike velocity, we repeat the central spike velocity measurement for each of the helium lines separately. Although the individual velocity measurements will have larger error than the measurement above from the three lines combined, agreement between the individual lines on the central spike velocities would give strong support to the correctness and significance of the determined amplitude and phase.

Table 2.3 shows the results for the spike velocities for each line after employing the orbital ephemeris (2.1). Indeed the individual lines yield mutually compatible locations for the central spike in velocity space, along the negative K_Y axis, giving support to the statistical significance of the determined zero phase in the ephemeris (2.1). Figure 2.3 shows the maximum-entropy Doppler tomograms (Marsh & Horne, 1988) that we obtain from this orbital ephemeris. We see that one of the two bright spots lines up near the expected stream–disc impact point in velocity space, especially for ballistic stream velocities at the impact site (cf. figure 2.5), while the other bright spot ends up in the lower-left quadrant. The uncertainty in the zero phase is on the order of $\arcsin(4.6/15.3) \approx 20°$ or 0.0013 days.

System parameters

From the low projected velocity amplitude of the primary ($v_{1,\mathrm{proj}} = 15.3 \pm 4.6$ km/s) and the projected velocity amplitude of the bright spot ($v_{\mathrm{spot,proj}} = 390 \pm 10$ km/s) we can put interesting limits on the mass ratio $q = M_2/M_1$ of the system. Since we have two velocity amplitudes, the unknown orbital inclination is eliminated quite trivially. The independence of the velocity ratio on the absolute mass of the components is slightly less trivial, but is easily demonstrated (appendix 2.5). We are left with just two parameters that determine the velocity ratio of the primary and the bright spot: the mass ratio q, and the effective accretion disc radius R at the stream–disc impact point.

Figure 2.4 shows the limits on q and R obtained by solving the equation of motion for a ballistic particle in the accretion stream (2.8) for a grid of values for q and R. A hard upper limit on R is caused by the accretion disc extending beyond the Roche lobe for large R. Similarly, a hard lower limit on R is set by conservation of angular momentum of the matter falling in from the inner Lagrange point, and the resulting constraint that the accretion disc should *at least* extend to the circularisation radius R_{circ}, the radius at which the specific angular momentum for matter in a Keplerian orbit around the primary equals that of matter in the L_1 point. In the remaining parameter space, a greyscale plot indicates the regions allowed by the data at various confidence levels.

We see that, for reasonable disc radii of $0.7 - 0.8 R_{L_1}$ and assuming ballistic stream velocities

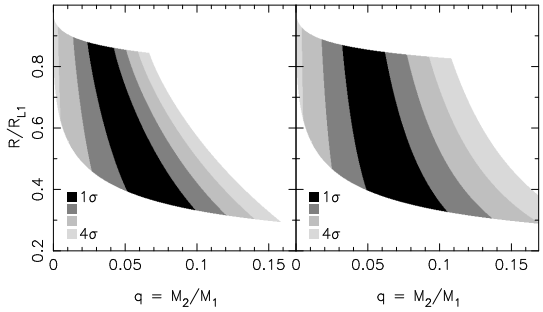

FIGURE 2.4: Allowed values of the accretion disc radius R and the mass ratio q for SDSS J1240. Left the results if one assumes ballistic stream velocities in the bright spot. In the right panel the results in case of disc velocities.

in the bright spot, we find a mass ratio of about $q = 0.039 \pm 0.010$.[1] In reality, there may be mixing with accretion disc velocities in the bright spot region. In case of pure Keplerian disc velocities the mass ratio increases slightly to 0.050 ± 0.015. We can conclude that the system is indeed of extreme mass ratio, as expected for an AM CVn star with a 37-minute orbital period. The mass ratio falls between $q \approx 0.087$ for AM CVn itself at $P_{\rm orb} = 1028$ s (Nelemans et al., 2001), and $0.017 < q < 0.020$ for GP Com at $P_{\rm orb} = 2970$ s (Steeghs et al. in prep.).

2.4 Discussion

2.4.1 System parameters

We presented high time resolution optical spectra of SDSS J1240 and determined an orbital period of 37.355±0.002 minutes, confirming beyond doubt the AM CVn nature of the system. This is further supported by the extreme derived mass ratio of 0.039±0.010.

It is interesting to compare the new system with theoretical predictions. Bildsten et al. (in prep.) have recently modelled the temperature of the accretors in AM CVn stars as a function of orbital period. Depending on the core temperature and mass of the donor star, they find an accretor temperature between 11,000–20,000 K for an AM CVn star with a 37-minute orbital period. The temperature of about 17,000 K derived for SDSS J1240 (Roelofs et al., 2004) is consistent with that prediction. With a more accurate measurement of the primary temperature, it may be possible to constrain the entropy of the donor star for SDSS J1240 based on the results of Bildsten et al., since the higher its entropy, the higher the mass transfer rate, and the hotter the

[1] R_{L_1} represents the distance from the centre of the primary to the L_1 point, not the effective radius of the primary Roche lobe.

primary for any given orbital period. High signal-to-noise flux-calibrated spectra in the UV would be needed for this, combined with realistic DB white dwarf atmosphere models.

We can estimate the distance to SDSS J1240 with the absolute magnitude $M_V \simeq 11.5$–12.0 as modelled by Bildsten et al., which is set by the effective temperature and radius of the accreting white dwarf. This gives a distance of $350-440$ pc and a height $z = 305-385$ pc in the Galactic disc.

For a given mass–radius relation of the Roche-lobe filling donor star, we can calculate the component masses using the measured orbital period and mass ratio. If we assume a fully degenerate, zero-temperature helium white dwarf (Zapolsky & Salpeter 1969, Rappaport & Joss 1984) we get a secondary mass of $0.012 M_\odot$, which means a primary mass of $0.31^{+0.10}_{-0.07} M_\odot$ and an inclination $i \sim 53°$. These are the minimum allowed masses for the system. For a semi-degenerate helium star secondary (see Nelemans et al., 2001) we obtain $M_2 = 0.031 M_\odot$, $M_1 = 0.79^{+0.28}_{-0.16} M_\odot$ and $i \sim 36°$.

2.4.2 Chemical composition and temperature of the accretion disc

The presence of Si II and Fe II clearly distinguishes SDSS J1240 from GP Com and CE 315. Si II was first observed in an AM CVn star by Groot et al. (2001) in a quiescent spectrum of CP Eri. A decade earlier, Marsh et al. (1991) noticed the strong underabundance of Si and Fe in GP Com (less than 1/1000 solar) based on the fact that they did *not* show up in the spectrum *at all*, and concluded that GP Com is probably a population II halo object. The identical spectral signature of CE 315, combined with its high proper motion, suggests a similar origin for CE 315. The spectrum of the new star SDSS J1240, like that of CP Eri, indicates a higher metallicity. A simple LTE model of a helium-dominated disc of about 11,000 K with solar abundances of heavy metals (similar to that used by Marsh et al. (1991), see Nelemans et al. (2004) for a description) predicts that Si II 6346 & 6371, Fe II 5169 and Ca II H & K should be the strongest metal lines. Apart from the calcium lines, which are not detected, this agrees with our observations. Furthermore, although the model is undoubtedly too simple, the strengths of the metal lines relative to helium indicate that the abundances of silicon and iron are compatible with solar values. We therefore expect that SDSS J1240, unlike GP Com and CE 315, is a more "ordinary" population I object. This is further supported by the low proper motion $\mu = 18 \pm 17$ mas/yr of the object, as measured by SuperCOSMOS from scans of southern sky survey plates.

Interestingly, a blue spectrum of 'SN2003aw' in its low state looks identical to that of SDSS J1240 shown in figure 2.1 but for the presence of strong Ca II H & K emission (Roelofs et al. in prep.). This is further indication that SDSS J1240, or at least the material that we are seeing now in the disc, may somehow be underabundant in calcium.

2.4.3 The second bright spot

When determining the mass ratio of the system, we assumed that one of the bright spots corresponds to the (first) stream–disc impact point. This is supported by the fact that one of the

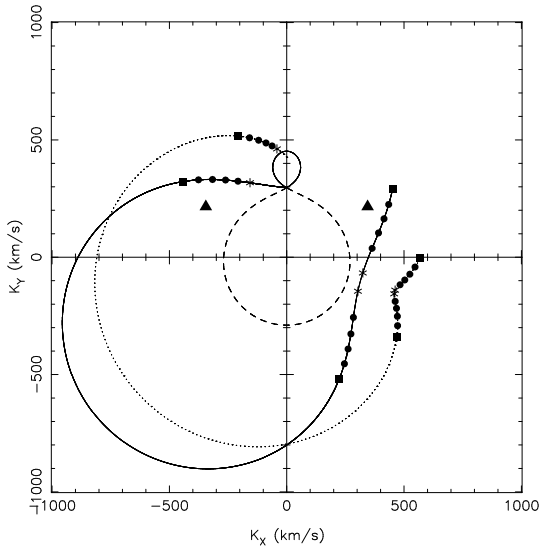

FIGURE 2.5: Possible scenarios for the second bright spot for a $q = 0.04$ binary. The solid line represents the stream velocities along the ballistic stream starting at the inner Lagrange point, while the dotted line indicates the Keplerian disc velocities at each point along the path followed by the stream. Adjacent spots represent the impact points for disc radii from $R = 0.6R_{L_1}$ (squares) to the maximum disc radius that can be contained within the primary Roche lobe (asterisks). The group of spots at $K_X > 0$ are the second and third crossing of the accretion disc edge by the ballistic stream. The triangles indicate the L_4 and L_5 points.

bright spots lines up with the expected stream–disc impact position in the tomograms if we use the zero-phase as determined by the central spike.

The origin of the second bright spot in the trailed spectra and Doppler tomograms is as yet unclear. Given the fact that the radial velocity of both bright spots is identical, one would expect a similar origin. The first thing that comes to mind is an overshoot scenario in which part of the accretion stream initially "misses" the (flared) edge of the accretion disc, and impacts the disc rim again on the other side of the disc. However, the stream would have to deviate significantly from a ballistic trajectory after the first impact point in order to produce the spot at the angle observed, in which case one would expect the radial velocity of the second bright spot to change significantly as well, contrary to what is observed. Figure 2.5 shows the ballistic trajectory and its second and third encounters with the edge of the accretion disc for a wide range of disc radii; clearly, no bright spot occurs in the lower-left quadrant of the Doppler tomogram. Another possibility is that the particle orbits in the outer disc get excited by the impact, causing a standing wave pattern in the outer disc, while a third possibility would be that the second bright spot is not caused by the mass stream, but is simply a tidal effect of the secondary and the disc, like the spiral arms observed in outbursting dwarf novae (Steeghs et al.,

2001).

If one considers the 120-degree angle between the bright spots as a starting point, then the "Trojan asteroids" at the L_4 and L_5 points come to mind as a natural 120-degree angle in any binary system. Furthermore, the extreme derived mass ratio $q = 0.039 \pm 0.010$ coincides with the stability criterion for matter in the L_4 and L_5 point ($q < 0.040$). However, as can again be seen in figure 2.5, the positions of the two spots in the Doppler tomograms as determined from the phase of the central spike do not match the expected L_4 and L_5 positions.

It should be stressed that the fact that the double bright spot pattern persists even in data from a single night rules out the possibility that they are the result of a mistake in identifying the correct orbital period alias. The double bright spot feature thus appears to be real. The correctness or statistical significance of our determined zero-phase is more open to debate, in which case the entire Doppler tomogram could be freely rotated around $K_X = K_Y = 0$, opening up more possibilities for the bright spots' origin.

Interestingly, VLT+UVES spectroscopy of both GP Com and CE 315 (Steeghs et al. in prep.) shows a very weak second bright spot at approximately the same place as in SDSS J1240. In these high-resolution data there is no room for a different zero-phase. Although the second bright spot is much weaker relative to the 'primary' bright spot than in SDSS J1240, it does suggest that the second bright spot feature, like the enigmatic central spike, may be another peculiar feature common to (and unique to) the AM CVn stars.

2.5 The system parameters

Consider a binary system in which all velocity vectors are in the orbital plane. The ratio of the projected bright spot velocity and the projected primary star velocity in a Doppler map is then given by

$$\frac{v_{\rm spot,proj}}{v_{\rm 1,proj}} = \frac{|\mathbf{v}_{\rm spot} + \omega \times \mathbf{r}_{\rm spot}|}{|\omega \times \mathbf{r}_1|} \tag{2.2}$$

To demonstrate the independence of this ratio on the absolute masses of the binary components, it will suffice to show that (i) the lengths of $\mathbf{r}_1$, $\mathbf{r}_{\rm spot}$ and $\mathbf{v}_{\rm spot}$ all scale with the same function of M_1, and that (ii) the angle between $\mathbf{r}_{\rm spot}$ and $\mathbf{v}_{\rm spot}$ remains the same. Consider the Roche potential

$$\Phi(\mathbf{r}) = -\frac{GM_1}{|\mathbf{r}-\mathbf{r}_1|} - \frac{GM_2}{|\mathbf{r}-\mathbf{r}_2|} - \frac{1}{2}(\omega \times \mathbf{r})^2 \tag{2.3}$$

where $\mathbf{r}$ points from the centre of mass, $\mathbf{r}_{1,2}$ denote the positions of the primary and secondary star, respectively, and the angular frequency ω is related to the masses and binary separation a as

$$\omega = \left[\frac{G(M_1+M_2)}{a^3}\right]^{1/2} \tag{2.4}$$

If we scale up the system by increasing the masses of the components while keeping their ratio fixed, it is clear from (2.3) and (2.4) that the potential difference between two points, say the inner Lagrange point and a point fixed on the edge of the accretion disc, scales as

$$\Delta\Phi \propto \frac{M_1}{a} \tag{2.5}$$

Therefore the speed gained by a ballistic particle (in the binary frame) goes as $v_{\rm bal} \propto \sqrt{M_1/a}$, while in a Keplerian disc, the velocities of matter orbiting the primary also scale as $v_{\rm kep} \propto \sqrt{M_1/a}$. Therefore, both in case of ballistic stream and Keplerian disc velocities in the bright spot, we have

$$|\mathbf{v}_{\rm spot}| \propto \sqrt{\frac{M_1}{a}} \tag{2.6}$$

while from (2.4) one sees that for all $\mathbf{r}$,

$$|\omega \times \mathbf{r}| \propto \sqrt{\frac{M_1}{a}} \tag{2.7}$$

Assuming an ideal Roche geometry, the full equation of motion for a ballistic particle becomes

$$\frac{\partial^2 \mathbf{r}}{\partial t^2} = -\nabla\Phi - 2(\omega \times \mathbf{v}) \tag{2.8}$$

in which it is now easy to verify that both terms on the right hand side scale as M/a^2. Hence, the shape of the ballistic stream is independent of the absolute mass scale. The angle between $\mathbf{v}_{\rm spot}$ and $\mathbf{r}_{\rm spot}$ will thus remain constant. Combined with (2.6) and (2.7) we may therefore conclude that the ratio of the projected bright spot and primary star velocities (2.2) is indeed independent of the absolute masses.

Chapter 3

Phase-resolved spectroscopy of the helium dwarf nova 'SN 2003aw' in quiescence

G. H. A. Roelofs, P. J. Groot, T. R. Marsh, D. Steeghs and G. Nelemans

MNRAS, 365, 1109 (2006)

Abstract. High time resolution spectroscopic observations of the ultra-compact helium dwarf nova 'SN 2003aw' in its quiescent state at $V \sim 20.5$ reveal its orbital period at 2027.8 ± 0.5 seconds or 33.80 minutes. Together with the photometric "superhump" period of 2041.5 ± 0.5 seconds, this implies a mass ratio $q \approx 0.036$. We compare both the average and time-resolved spectra of 'SN 2003aw' and SDSS J124058.03−015919.2 (Roelofs et al., 2005). Both show a DB white dwarf spectrum plus an optically thin, helium-dominated accretion disc. 'SN 2003aw' distinguishes itself from the SDSS source by its strong calcium H & K emission lines, suggesting higher abundances of heavy metals than the SDSS source. The silicon and iron emission lines observed in the SDSS source are about twice as strong in 'SN 2003aw'. The peculiar "double bright spot" accretion disc feature seen in the SDSS source is also present in time-resolved spectra of 'SN 2003aw', albeit much weaker.

3.1 Introduction

The AM CVn stars are ultra-compact binaries: white dwarfs accreting from a degenerate, helium-rich companion star. The have orbital periods shorter than about one hour, clearly indicating the evolved nature of their donor stars. Their accretion disc spectra show mainly helium, with no traces of hydrogen and varying contributions of heavy metals. See Nelemans et al. (2001) for a recent review.

No less than six new members of the small AM CVn family, including the first eclipsing system, have been found in the last year or so (Woudt et al., 2005; Roelofs et al., 2005; Anderson et al., 2005). Optical spectroscopy of one of the new members, SDSS J124058.02−015919.2 (hereafter SDSS J1240, Roelofs et al. 2005) allowed for a measurement of the orbital period and of the mass ratio, and showed a peculiar and as yet not understood feature of two equally strong bright spots in the accretion disc, in strong contrast with the usual one bright spot attributed to the impact of the accretion stream into the disc. In this paper we present time-resolved spectroscopy of another recent addition to the family, and a close relative of SDSS J1240: 'SN 2003aw'.

'SN 2003aw' was found as a supernova candidate in February 2003, based on an observed strong increase in brightness (maximum $V \sim 16.5$) and its supposed positional coincidence with a faint galaxy (Wood-Vasey et al., 2003), but Chornock & Filippenko (2003) identified it spectroscopically as a helium-rich dwarf nova. Following their announcement, Woudt & Warner (2003) performed fast white-light photometry on the source, from which a periodic modulation of 2041.5 ± 0.5 seconds was derived. They attributed this period to a superhump, although an analysis of the Fourier spectrum showed sidebands to the main period that could point to an orbital modulation rather than a superhump.

Over a period of about six months from its detection as a supernova candidate the source was seen to decline to its apparent quiescent state at $V \sim 20.5$ (Woudt & Warner, 2003). We caught the star in quiescence in December 2003, when we took a few low-resolution spectra. Our first set of phase-resolved spectroscopic observations was taken in March 2004, thirteen months after its discovery, with the star still in quiescence near $V = 20.5$. In May 2004 the star was reported to be in outburst again (Nogami et al., 2004) with an even higher maximum detected brightness at $V = 15$. In March 2005 we then obtained our second, larger set of phase-resolved spectra, the star having returned to a quiescent state again near $V = 20.5$.

3.2 Observations and data reduction

We obtained phase-resolved spectroscopy of 'SN 2003aw' on 18 and 19 March 2004, and on 1 and 2 March 2005 with the Very Large Telescope (VLT) of the European Southern Observatory and the FOcal Reducer/low dispersion Spectrograph (FORS2). The observations consist of 159 spectra in the blue (grism 600B), most of them with a 180-second exposure time. Typical seeing was $0.6''$ giving an effective resolution of $\sim$4 Å; for 50 of the 159 spectra we used slightly longer

Date	UT	Exposure time (s)	Exposures
Magellan			
2003/12/15	08:08–08:40	900	3
VLT			
2004/03/18	01:27–02:43	260	14
2004/03/19	00:24–01:23	260	14
2005/03/01	00:30–05:04	180	70
2005/03/02	00:37–03:33	180	39
	03:38–05:22	240	22

Table 3.1: Summary of our observations of 'SN 2003aw'.

exposure times of 240 or 260 seconds because of less perfect seeing conditions ($\sim 1''$, resolution $\sim$6 Å).

All VLT observations were done with a $1''$ slit. The detector was the MIT CCD mosaic of which only chip 1 was used; binning was standard 2×2 pixels. Low read-out speed and high gain minimized the read-out and digitisation noise, respectively. In order not to add more noise to the spectra, we subtracted a constant bias level from each CCD frame. The bias level was determined per frame from the overscan regions on the CCD. A normalised flatfield frame was constructed from 5 incandescent lamp flatfield frames each night, which ensured a cosmic-ray-free final flatfield.

All spectra were extracted using the IRAF implementation of optimal (variance-weighted) extraction. The read-out noise and photon gain, necessary for the extraction, were calculated from the bias and flatfield frames, respectively. Wavelength calibration was done with a standard HeHgCd arc exposure taken during the day. A total of around 40 arc lines could be fitted well with a Legendre polynomial of order 3 and 0.14 Å root-mean-square residual. All spectra were transformed to the heliocentric rest-frame prior to analysis.

The average spectrum was corrected for instrumental response using spectroscopic standard star EG274.

In addition to the phase-resolved spectra described above, we obtained three 900-second spectra with the IMACS spectrograph on the Magellan–Baade telescope at Las Campanas Observatory on 15 December 2003. An $0.7''$ slit together with the 300 lines/mm grating provided coverage between 3400–9500 angstrom at 4.6 Å resolution.

A summary of all observations is given in table 3.1.

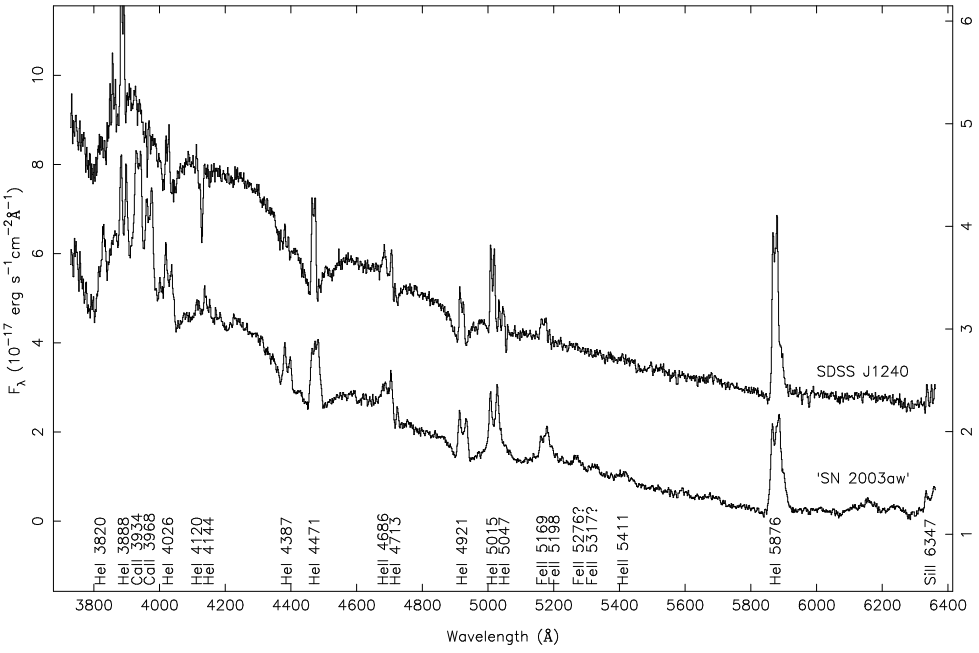

FIGURE 3.1: Average spectra of SDSS J1240 (top spectrum & left axis, Roelofs et al. 2005) and 'SN 2003aw' (bottom spectrum & right axis). The most prominent lines are labelled. Uncertain identifications carry a question mark.

3.3 Results

3.3.1 Average spectrum

The flux-calibrated average spectrum of 'SN 2003aw' is shown in figure 3.1. It is a striking match to the average blue spectrum of SDSS J1240 from Roelofs et al. (2005). The latter is reproduced in figure 3.1 for easy reference. The spectrum of 'SN 2003aw' also shows the characteristic broad helium absorption lines, presumably from the accreting white dwarf, in addition to the double-peaked emission lines, mainly helium, from the accretion disc. There are a few differences: first, the accretion disc lines are much broader, extending to ∼1000 km/s FWHM, suggesting a higher inclination than SDSS J1240. Second, the accretion disc shows strong calcium H & K emission, in addition to the iron and silicon features also seen in SDSS J1240. Table 3.2 lists the equivalent widths of a number of accretion disc emission lines for both SDSS J1240 and 'SN 2003aw'; the blue helium lines are omitted because of the strong influence of the underlying white dwarf's absorption lines. The strengths of the helium lines are identical in both objects, whereas the heavy metal lines are significantly stronger in 'SN 2003aw'. The He I 5876 line is blended with a weak unidentified emission feature around 5896 Å in both

Line	Equivalent widths (Å)	
	SDSS J1240[1]	'SN 2003aw'[2]
He I 5876	-31.3 ± 0.5	-30.3 ± 0.5
He I 6678	-19.6 ± 0.1	-18.5 ± 1.1
He I 7065	-25.0 ± 0.1	-25.5 ± 1.7
He I 7281	-10.3 ± 0.1	-11.3 ± 2.2
Fe II 5169	-2.1 ± 0.2	-5.0 ± 0.5
Si II 6347	-2.2 ± 0.1	-4.0 ± 0.4
Ca II 3934	0.0 ± 0.5	-5.6 ± 0.5
Ca II 3968	0.0 ± 0.5	-5.6 ± 0.5

Table 3.2: Equivalent widths of several accretion disc emission lines, including estimated errors. [1]Spectra published in Roelofs et al. (2005); [2]He I 6678, 7065 & 7281 lines based on our Magellan spectrum (not shown).

objects, which might be Na D. This emission feature is included in the equivalent widths of the He I 5876 line in table 3.2.

3.3.2 The spectroscopic period

To determine the spectroscopic period of the binary, we used a modified version of the method used by Nather et al. (1981), as described in Roelofs et al. (2005). Figure 3.2 shows the resulting Lomb–Scargle periodogram of red wing–blue wing emission line flux ratios. The long baseline between our 2004 and our 2005 observations causes a fine pattern of aliases on top of the usual 1 day^{-1} aliases in the periodogram. The strongest peak occurs at 42.6 cycle/day. In addition to the main peaks around this frequency there appears to be a weak group of higher harmonics much like in SDSS J1240 (Roelofs et al., 2005). The strongest harmonic is exactly three times the frequency of the overall strongest peak, compatible with a second bright spot in the accretion disc appearing 120 degrees out of phase.

3.3.3 Doppler tomography

Features of the accretion disc

Figure 3.3 shows the trailed spectra and maximum-entropy Doppler tomograms (Marsh & Horne, 1988) of the strongest lines of 'SN 2003aw'. There is one strong emission bright spot causing a clear S-wave in the trailed spectra; the He I 5015 line also shows a second S-wave at approximately 30% of the flux of the main S-wave. There are two lines in the current data that are also present in the SDSS J1240 data of Roelofs et al. (2005), namely Si II 6347 and He I 5876; these are compared directly in figure 3.4. The double bright spot pattern in the SDSS

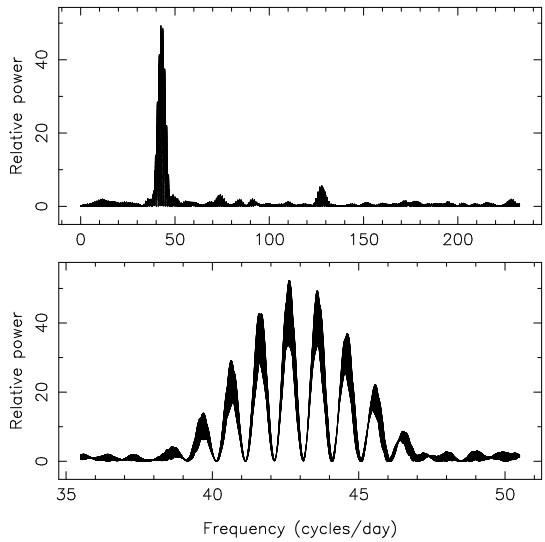

FIGURE 3.2: Lomb-Scargle periodogram of the red wing/blue wing emission line flux ratios. The lower panel provides a magnified view of the strongest peaks.

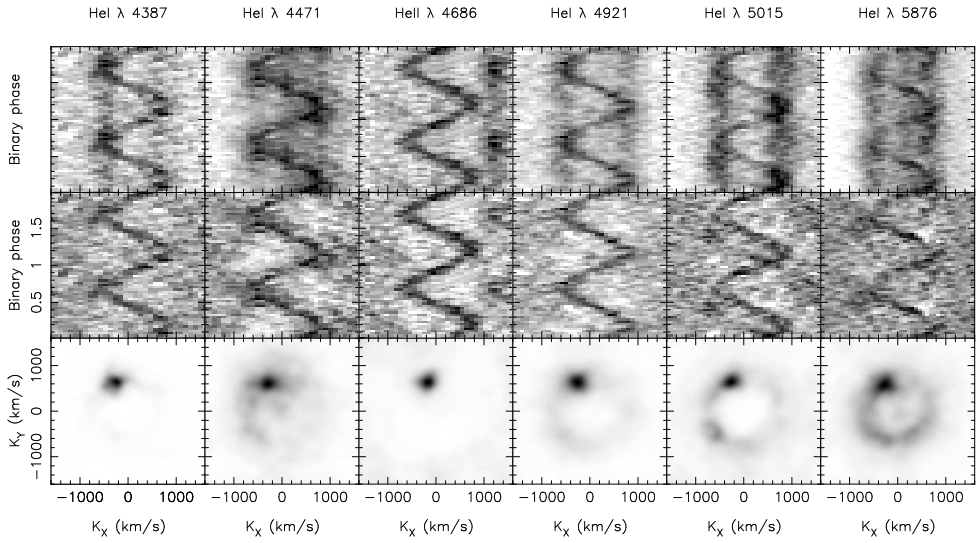

FIGURE 3.3: Trailed spectra (top row), average-subtracted trailed spectra (middle row) and maximum-entropy Doppler tomograms (bottom row) of the strongest He I and He II features.

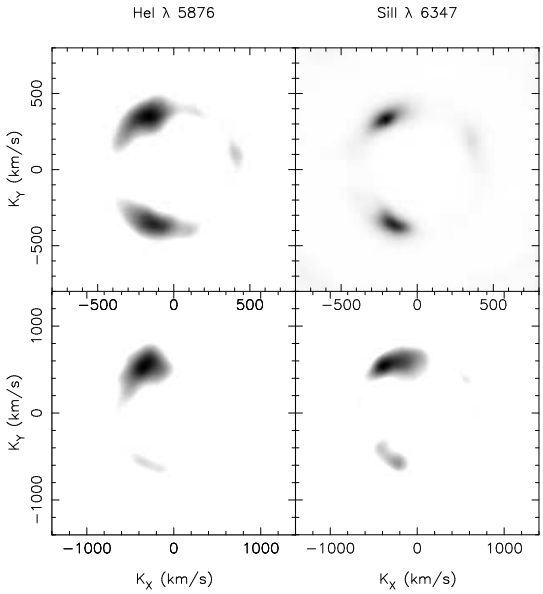

Figure 3.4: Detailed comparison of Doppler tomograms between SDSS J1240 (top row) and 'SN 2003aw' (bottom row). The tomograms of 'SN 2003aw' are aligned with those of SDSS J1240 artificially, since we do not have a zero-phase measurement for 'SN 2003aw'. A linear back-projection code that can cope with the Si II line being at the edge of our spectral window is used for 'SN 2003aw'.

source is not reproduced in 'SN 2003aw', but there do seem to be very weak secondary bright spots at approximately the same position as in the SDSS source.

The orbital period

In section 3.3.2 we determined the spectroscopic period from a periodogram of red wing–blue wing emission line flux ratios. The clear kinematic S-wave feature in the trailed spectra, when phase-folded on this spectroscopic period, indicates that we are seeing the orbital motion of the binary. The strength and sharpness of the bright spot in the Doppler tomograms, especially in the He II 4686 line, allows us to determine the orbital period quite accurately. The coverage per night during our 2005 run (about 4.5 hours) is sufficient that we can distinguish between the true orbital period and its 1 day^{-1} aliases in the periodogram, since these aliases already lead to noticeable smearing of the bright spot signal when phase-folding the spectra from a single night.

Assuming that the bright spot is fixed in the binary frame, we can further refine the orbital period by lining up the phases of the bright spot in the tomograms of March 1 and March 2, 2005. The bright spot phases are determined by fitting a 2-D Gaussian in the Doppler

tomograms. We estimate the uncertainty in the fitted bright spot phases with a simple Monte Carlo simulation, where we make a large ensemble of Doppler tomograms from our dataset using the bootstrap method. For each March 1 Doppler tomogram we thus randomly pick 70 spectra out of the set of 70 spectra that we have for this night, allowing for a spectrum to be picked more than once. We fit a 2-D Gaussian to each tomogram in the ensemble; the resulting distribution of fitted bright spot locations in K_X, K_Y space gives an estimate of the accuracy allowed by the data.

In practice there may also be an intrinsic shift in the bright spot phase due to changes in the effective accretion disc radius at the stream–disc impact point. In such a scenario, the radial velocity of the bright spot in the Doppler tomograms is expected to change more than its phase, since both the accretion stream and accretion disc velocity (at the stream–disc impact point) change faster with accretion disc radius than their directions, for reasonable accretion disc radii (see, for instance, figure 5 in Roelofs et al. 2005). The radial velocity change measured in the bright spot between March 1 and 2, 2005 thus gives us a reasonable measure for the maximum intrinsic bright spot phase shift. We add this radial velocity change to the statistical fit uncertainty from the Monte Carlo ensemble; both give an uncertainty of about 20 km/s. The total uncertainty in lining up the bright spots from March 1 and 2, 2005 thus comes out at ∼4 degrees. The orbital period and its error then become $P_{\rm orb} = 2027.8 \pm 0.5$ seconds.

The one-year baseline between our 2004 and 2005 runs does not allow us to trace the orbit all the way in between, since one revolution fewer or more between these runs would correspond to a phase drift of just about one degree between the two consecutive nights of our 2005 run, which is below the accuracy with which we can measure the bright spot's phases in the 2005 data.

3.4 Discussion

3.4.1 Chemical composition of the accretion disc

Marsh et al. (1991) first modelled the accretion disc spectrum of the 46-minute orbital period AM CVn star GP Com and found a strong underabundance of heavy metals relative to the Sun. In particular, expected emission lines of singly ionised iron, silicon and calcium were missing from the spectrum. The recently discovered AM CVn star SDSS J1240 showed clear Fe II 5169, Si II 6347 and Si II 6371 emission, compatible with solar abundances (Roelofs et al., 2005). Calcium H & K were also expected if solar abundances of heavy metals were assumed, but could not be found in the spectrum. They do show up strongly in the spectrum of 'SN 2003aw' presented here. The spectrum of 'SN 2003aw' furthermore shows possible weak iron features near 5276 and 5317 Å not seen in SDSS J1240 (cf. figure 3.1). The possible Na D emission feature in both SDSS J1240 and 'SN 2003aw', mentioned in section 3.3.1, must originate in relatively cool parts of the accretion disc — a large part of the disc where most of the emission lines originate is expected to be at ≈11,000 K (see Marsh et al. 1991 for a discussion), where the sodium should be largely ionised and the Na D lines would not show up. The feature does

not show any bright spot (nor the typical double-peaked profile) in the trailed spectra, which is then conform expectations if it is sodium D.

We now have two emission-line systems that seem to be strongly underabundant in heavy metals (GP Com, $P_{\rm orb} = 46$ min and CE 315, $P_{\rm orb} = 65$ min), which together with their high proper motions suggests a halo origin, and two systems showing more or less the expected metal lines if solar abundances of heavy metals are assumed (SDSS J1240, $P_{\rm orb} = 37$ min and 'SN 2003aw', $P_{\rm orb} = 34$ min). The stronger silicon and iron lines in 'SN 2003aw' relative to helium (by about a factor of 2, see table 3.2) can probably be accommodated by a higher column density of gas in the disc – e.g. due to a higher mass transfer rate – and saturated helium lines. The complete absence of calcium H & K in SDSS J1240 is more difficult to explain, but together with the notion that the Si II 6347 & 6371 lines in SDSS J1240 originate exclusively from the bright spots, this suggests somewhat higher abundances of heavy metals in 'SN 2003aw' (if we assume both discs to be largely at ≈11,000 K). A more detailed study of these optically thin helium-dominated accretion discs is beyond the scope of this paper, but will be interesting for estimating the mass transfer rates and for putting more accurate constraints on the chemical abundances in the discs.

3.4.2 The second bright spot

The remarkable double bright spot feature in SDSS J1240 was one of the motivations for obtaining the observations presented here. Since the average spectrum of 'SN 2003aw' looked so similar, and since the suggested orbital period from the photometric superhump was quite close to that of SDSS J1240, it was interesting to see if the accretion disc would show the same behaviour.

From the trailed spectra and Doppler tomograms (figure 3.3) it is clear that the He I 5015 line does indeed show a second S-wave much like in SDSS J1240, but it is significantly weaker at about 30% of the integrated flux of the main S-wave. A direct comparison of the He I 5876 and of the Si II 6347 line, for which there are phase-resolved spectra of both objects, shows the weakness of the second bright spot in these lines compared to SDSS J1240 (figure 3.4). So more than anything else, 'SN 2003aw' adds to the diversity of the second bright spot feature. A very recently discovered new AM CVn star, 2QZ J142701.6−012310 (Woudt et al., 2005) with a suggested orbital period near 36 minutes (again based on a photometric superhump period), even closer to the orbital period of SDSS J1240, may be a nice test case for this still enigmatic feature.

3.4.3 The orbital period

We measure an orbital period $P_{\rm orb} = 2027.8 \pm 0.5$ seconds. This proves that the photometric period of 2041.5±0.5 seconds first detected by Woudt & Warner (2003) is a superhump period. Therefore the helium dwarf nova 'SN 2003aw', like the permanent superhumper AM CVn (Nelemans et al., 2001), exhibits positive superhumps, which are usually explained as the beat

period of the orbit and the prograde precession of a tidally deformed eccentric accretion disc. If we employ the latest empirical relation between the mass ratio q and the superhump period excess ϵ, as determined from superhump and orbital periods of a large number of hydrogen-rich dwarf novae by Patterson et al. (2005):

$$\epsilon(q) = 0.18q + 0.29q^2 \tag{3.1}$$

where

$$\epsilon \equiv \frac{P_{\rm sh} - P_{\rm orb}}{P_{\rm orb}} \tag{3.2}$$

we find $q = 0.036 \pm 0.003$. This compares to $q = 0.039 \pm 0.010$ determined kinematically for SDSS J1240 (Roelofs et al., 2005). It should be stressed that the relation (3.1) may not be well-calibrated for these extreme mass ratios, and in reality ϵ might depend on more parameters than just q. The quoted error on the mass ratio may therefore be a bit optimistic.

Chapter 4

Kinematics of the ultra-compact helium accretor AM Canum Venaticorum

G. H. A. Roelofs, P. J. Groot, G. Nelemans, T. R. Marsh and D. Steeghs

MNRAS, 371, 1231 (2006)

Abstract. We report on the results from a five-night campaign of high-speed spectroscopy of the 17-minute binary AM Canum Venaticorum, obtained with the 4.2-m William Herschel Telescope on La Palma.

We detect a kinematic feature that appears to be entirely analogous to the 'central spike' known from the long-period, emission-line AM CVn stars GP Com, V396 Hya and SDSS J124058.03−015919.2, which has been attributed to the accreting white dwarf. Assuming that the feature indeed represents the projected velocity amplitude and phase of the accreting white dwarf we derive a mass ratio $q = 0.18 \pm 0.01$ for AM CVn. This is significantly higher than the value found in previous, less direct measurements. We discuss the implications for AM CVn's evolutionary history and show that a helium star progenitor scenario is strongly favoured. We further discuss the implications for the interpretation of AM CVn's superhump behaviour, and for the detectability of its gravitational-wave signal with *LISA*.

In addition we demonstrate a method for measuring the circularity or eccentricity of AM CVn's accretion disc, using stroboscopic Doppler tomography. We test the predictions of an eccentric, precessing disc that are based on AM CVn's observed superhump behaviour. We limit the effective eccentricity in the outermost part of the disc, where the resonances that drive the

eccentricity are thought to occur, to $e = 0.04 \pm 0.01$, which is smaller than previous models indicated.

4.1 Introduction

AM Canum Venaticorum was found in a survey of faint, blue objects by Humason & Zwicky (1947). It was observed to have peculiarly broad and shallow helium absorption lines, but no hydrogen (Greenstein & Matthews, 1957). The star was shown to be a possible ultra-compact white dwarf binary by Smak (1967), who discovered photometric variations on an 18-minute period; quickly thereafter, Paczynski (1967) noted that it would be a prime example of a binary whose evolution is expected to be governed by gravitational-wave radiation, and which could serve as an excellent test for the existence of gravitational radiation. The interpretation as an interacting binary analogous to the Cataclysmic Variables was first proposed by Warner & Robinson (1972) upon their discovery of rapid flickering in the light-curve. The discussion as to the true orbital period of the system was finally put to rest by Nelemans et al. (2001) who discovered a kinematic 'S-wave' feature in time-resolved spectra of AM CVn, thereby proving that the orbital period is 1028 seconds, while the main photometric signal at 1051 seconds is to be interpreted as a 'superhump'.

Here we present phase-resolved spectra of AM CVn with significantly higher spectral resolution and signal-to-noise ratio than those previously used by Nelemans et al. (2001). Moreover, our current data-set fully samples the proposed 13.37-h accretion disc precession period (Patterson et al., 1993; Skillman et al., 1999) for the first time, allowing for a characterisation of the spectroscopic appearance of the system as a function of orbital period, precession period, and superhump (beat) period.

4.2 Observations and data reduction

We obtained phase-resolved spectroscopy of AM CVn on 20, 21, 22, 23 and 24 March 2005 with the William Herschel Telescope (WHT) and the ISIS spectrograph. The observations consist of 2159 spectra taken with the 1200B grating, covering ∼4300–5100Å; the exposure time was 30–40 seconds depending on sky transparency and airmass. The sky varied from clear to opaque due to high clouds, but the median seeing was quite good, about $0.8''$, giving an effective resolution of about 0.7 Å or 45 km/s.

The chosen slit width was dependent on the seeing and transparency, and varied from $1.0'' - 1.4''$. The detector was the standard EEV12 chip in the spectrograph's blue arm, windowed and binned by a factor of two in the spatial direction to increase the read-out speed. The read-out speed was kept 'low' to minimize the read-out noise. Each night, an average bias frame was

Date	UT	Exposures (30–40 s)	Typical seeing (")
2005/04/20	20:52–05:06	523	0.8
2005/04/21	22:46–05:15	114	0.8
2005/04/22	20:41–05:04	585	1.1
2005/04/23	21:03–04:57	370	1.4
2005/04/24	20:35–05:01	567	0.8

TABLE 4.1: Summary of our observations.

created from 20 individual bias exposures, and a normalised flatfield frame was constructed from 20 incandescent lamp flatfields.

All spectra were extracted using the IRAF implementation of optimal (variance-weighted) extraction. The read-out noise and photon gain, necessary for the extraction, were calculated from the bias and flatfield frames, respectively. HeNeAr arc exposures were taken every hour during the night to correct for instrumental flexure; all dispersion solutions were interpolated between the two arc exposures nearest in time. Arcs were taken before and after every rotator adjustment needed to keep the slit at near-parallactic angle. In each arc exposure a total of about 40 arc lines could be fitted well with a Legendre polynomial of order 4 and 0.04 Å root-mean-square residuals. The root-mean-square residuals due to flexure are estimated to be smaller than this; the total arc drift was measured to be 0.5 Å peak-to-peak over an entire night. All spectra were transformed to the heliocentric rest-frame prior to analysis.

The average spectrum was corrected for instrumental response using spectrophotometric standard star Feige 34.

A summary of all observations is given in table 4.1.

4.3 Results

4.3.1 Average and phase-binned spectra

The grand-average spectrum of AM CVn is shown in figure 4.1. It shows several broad neutral helium absorption lines seen before in AM CVn's spectrum, and clear emission of He II 4686. The absorption wings extend to about 1300 km/s (half width at half minimum). See table 4.2 for a list of equivalent widths for the strongest absorption lines.

The phase-binned (trailed) spectrum reveals several additional, weaker features that are too smeared out in the average spectrum to be detected. See figures 4.2 and 4.3. Among these are the 'S-wave' emission features in several lines, already found by Nelemans et al. (2001). It includes the metal line Mg II 4481; already present but not mentioned in Nelemans et al.

Line	Equivalent width (Å)
He I 4387	1.58 ± 0.02
He I 4471 (+He I 4437)	2.84 ± 0.02
He II 4686 (+He I 4713)	0.76 ± 0.04
He I 4921	2.60 ± 0.05
He I 5015	0.73 ± 0.02

TABLE 4.2: Equivalent widths of the detected accretion disc absorption lines, including estimated errors, in the average spectrum of AM CVn (figure 4.1).

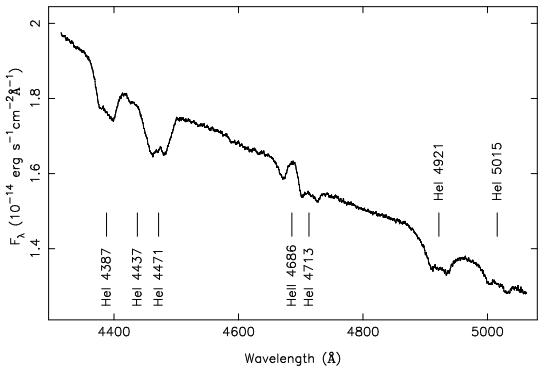

FIGURE 4.1: Average spectrum of AM CVn. The wavelength-dependent instrumental response has been corrected for, but the overall received flux is strongly affected by clouds; no attempt has been made to correct for this.

(2001). Two very weak S-wave features flank the (also very weak) He I 5048 line, which we identify with Si II 5041 & 5056.

The most remarkable is a weak and narrow emission feature slightly offset to the red of He I 4471. It is clearly offset in phase from the presumed bright spot feature, and has a much lower amplitude (see figure 4.3). As such it has everything in common with the 'central spike' feature that was first detected in GP Com (Smak, 1975) and has since become a common (though poorly understood) feature in long-period, emission-line AM CVn stars (Ruiz et al., 2001; Roelofs et al., 2005). As in the aforementioned systems, the phase of the low-velocity component (relative to the bright spot) is consistent with the expected phase of the accreting white dwarf, and its relatively low velocity amplitude is difficult to reconcile with any emission site in the accretion disc. It is also intrinsically redshifted through some as yet unknown mechanism (cf. Marsh 1999; Morales-Rueda et al. 2003). Based on these three properties, we interpret the feature as the perfect analogue of the central spike in GP Com, V396 Hya, and SDSS J124058.03−015919.2.

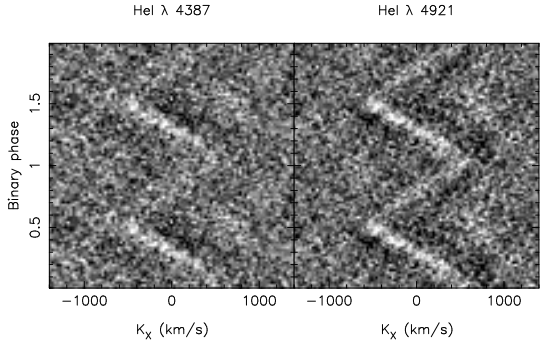

FIGURE 4.2: Phase-binned, average-subtracted spectrum of AM CVn around the He I 4387 and He I 4921 lines.

We see no evidence for a central spike in any of the other helium lines. However, from Morales-Rueda et al. (2003) we see that the central spike is strongest in the He I 4471 line in GP Com, and it is clear that we are barely detecting this line's spike in AM CVn. Our non-detection of a spike in the other helium lines is thus plausibly a matter of signal-to-noise.

4.3.2 Doppler tomography

The central spike

The weak, sinusoidal emission feature we interpret as the central spike in the He I 4471 line can be made more tangible in a linear back-projection Doppler tomogram (Marsh & Horne, 1988). We begin by phase-binning our 2159 spectra in ∼200 bins using the known orbital period $P_{\rm orb} = 1028.7322\,{\rm s}$ (Harvey et al., 1998; Skillman et al., 1999). The two bright spots close to the spike – from the He I 4471 line itself and from the nearby Mg II 4481 line, see figure 4.3 – are masked out to prevent them from dominating the (back-projected) spectra. Each phase-binned spectrum is then normalised by fitting a polynomial and dividing the spectrum by it, and finally all phase bins are divided by the column-averaged spectrum so that we are left with the components of the spectrum that vary on the orbital period, apart from the bright spots which were masked out earlier.

The next step is determining the central spike's rest wavelength or, equivalently, its intrinsic (rest) velocity γ relative to the He I 4471 rest wavelength. We proceed in the same manner as in Roelofs et al. (2005), that is, we make Doppler tomograms for a range of trial wavelengths and determine the wavelength at which the spectra auto-correlate best. As in Roelofs et al. (2005), the height of the presumed central spike nicely peaks at a certain wavelength, which we take as the rest wavelength of the central spike. See table 4.3 and the corresponding Doppler tomogram in figure 4.4.

Feature	γ (km/s)	K_Y (km/s)	K_X (km/s)
Bright spot	0 ± 5	330 ± 8	-336 ± 8
Central spike	40 ± 4	-92 ± 4	0 ± 4

TABLE 4.3: Velocities of the bright spot and central spike components of the He I 4471 line, after aligning the central spike with the negative K_Y axis.

The final step is determining the central spike's velocity amplitude and phase, and their associated errors. We employ the bootstrap method used in Roelofs et al. (2006a). In this Monte Carlo process we make a large number (10^3) of Doppler tomograms with the recipe described above, using a random selection of 2159 spectra taken from our data set, and allowing for replacement. We determine the emission centroid of the central spike in each tomogram, make a 2-D histogram of all the K_X and K_Y values obtained, and fit a 2-D Gaussian to this distribution. The width of this Gaussian is taken as a measure for the error on the central spike's coordinates in K_X, K_Y space. See table 4.3 for the results.

The bright spot

We follow the same procedure as for the central spike, but now masking out only the bright spot of the Mg II 4481 line. We again construct an ensemble of $\sim 10^3$ Doppler tomograms via the bootstrap method in order to be able to estimate the errors on the resulting data points. Table 4.3 lists the rest wavelengths, velocity amplitudes and phases as well as their errors, of both the bright spot and the central spike of the He I 4471 line. The central spike has been aligned with the negative K_Y axis, which coincides with the conventional zero-phase of the accreting white dwarf.

Figure 4.5 shows the velocities of the central spike and the bright spot, with errors, to show their relative phases and amplitudes, after aligning the central spike with the negative K_Y axis. Looking ahead at the next section, we also plot the velocities of a free-falling accretion stream, as well as the Keplerian velocities along the trajectory of the ballistic accretion stream, for a binary of mass ratio $q = M_2/M_1 = 0.18$.

4.3.3 The mass ratio of AM CVn

Using the velocity amplitudes and phases of the central spike and the bright spot, we can constrain the mass ratio and the effective accretion disc radius in AM CVn. To this end we solve the equation of motion for a free-falling stream of matter through the inner Lagrangian point, based on the results of Lubow & Shu (1975), and we see whether the resulting accretion stream and/or accretion disc velocities and phases at the stream–disc impact point match with the measured values. The results are displayed in figure 4.6.

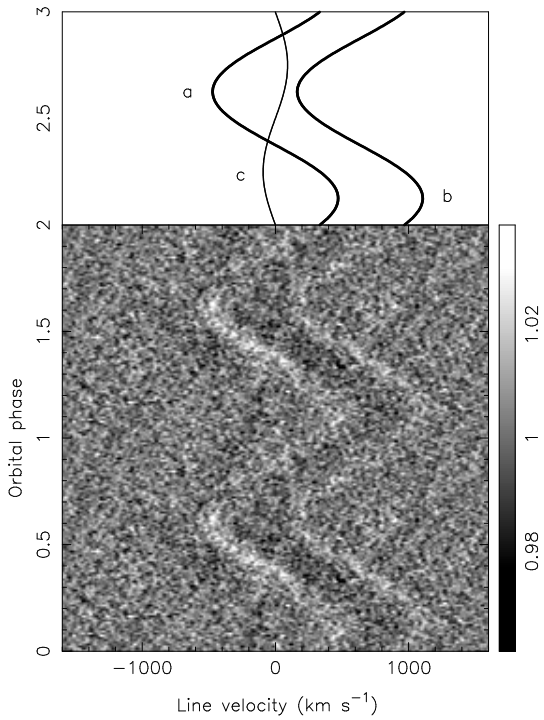

FIGURE 4.3: Phase-binned, average-subtracted spectrum of AM CVn around the He I 4471 line. The bright spot trails around zero velocity (component a), in phase with the bright spot from the nearby Mg II 4481 line (b). In addition there is a weak component moving around 40 km/s with a semi-amplitude of 92±5 km/s, and offset in phase from the bright spot (c). We propose that this is the 'central spike' of the He I 4471 line.

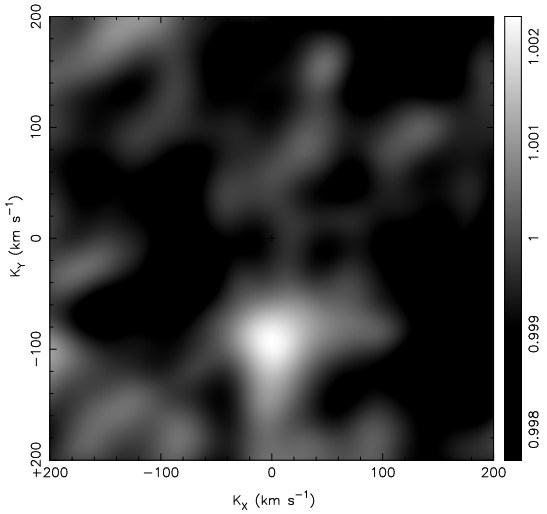

FIGURE 4.4: Linear back-projection Doppler tomogram of the redshifted, low-velocity central spike. Its velocity amplitude comes out at 92±5 km/s. Its phase has been aligned with the negative K_Y axis, the conventional zero-phase of the accreting star.

Keplerian velocities in the bright spot imply very small effective accretion disc radii ($R \sim 0.3R_{L1}$, with R_{L1} the distance from the centre of the accretor to the inner Lagrange point), and very large mass ratios ($q \sim 0.5$). In particular, the disc would not come anywhere near the 3 : 1 resonance radius. This resonance is commonly thought to drive the superhump behaviour that is observed in outbursting dwarf novae as well as nova-like systems such as AM CVn (Whitehurst & King, 1991; Hirose & Osaki, 1990).

For purely ballistic stream velocities in the bright spot, the best-fitting accretion disc radius is $5-10\%$ smaller than the maximum accretion disc radius that can be contained within the primary star's Roche lobe. In this case, the disc would clearly extend past the 3 : 1 resonance radius. If we assume purely ballistic stream velocities, we obtain a mass ratio $q = 0.18 \pm 0.01$. This constitutes a lower limit.

If we allow for mixing between the ballistic stream and the Keplerian disc velocities, the mass ratio could be slightly larger than this. See figure 4.6. The maximum mass ratio for which the bright spot would remain outside the 3 : 1 resonance radius is $q \leq 0.22 \pm 0.01$, which corresponds to a (best-fitting) mix of about 80% stream and 20% disc velocities. A mass ratio of $q \lesssim 0.25$ is commonly quoted as the requirement for a binary to be able to excite its 3 : 1 resonance and develop the corresponding superhumps (Whitehurst, 1988; Whitehurst & King, 1991; Hirose & Osaki, 1990).

Two values for the mass ratio q from the literature are overplotted in figure 4.6. Both these values are derived from the fractional superhump period excess $\epsilon \equiv (P_{\rm sh} - P_{\rm orb})/P_{\rm orb} = 0.0216$

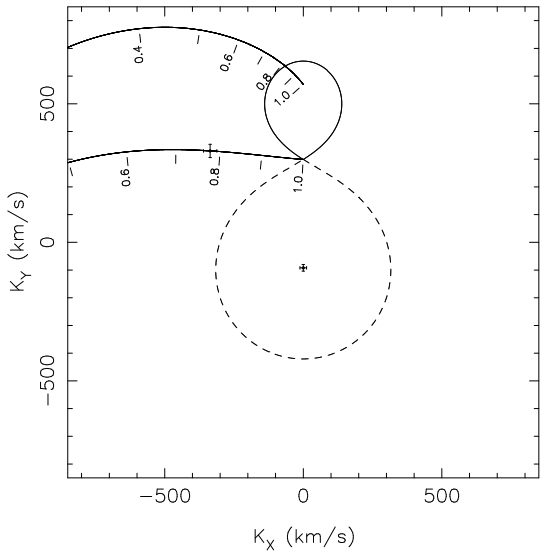

FIGURE 4.5: The measured central spike and bright spot velocities, with the associated 3-σ error bars. Overplotted is the best-fitting binary of mass ratio $q = 0.18$, with the ballistic accretion stream starting at the inner Lagrange point and passing through the bright spot. The upper solid line starting within the secondary star represents the Keplerian accretion disc velocities along the ballistic stream trajectory. The labels represent the accretion disc radius as a fraction of R_{L1}.

observed in AM CVn (e.g. Skillman et al. 1999), combined with theoretical-numerical or empirical relations between ϵ and q. The mass ratio derived from AM CVn's kinematics is significantly larger than these predictions. The present data indicate a lower limit of $q = 0.18 \pm 0.01$, compared with $q = 0.10$ as obtained from the latest empirical $\epsilon(q)$ relation for hydrogen-rich Cataclysmic Variables by Patterson et al. (2005) (P05). The value $q = 0.087$ found by Nelemans et al. (2001) (NSG01), from fits to numerical accretion disc simulations as taken from Warner (1995), deviates even more. In the remainder of this paper, we shall conservatively use $q = 0.18 \pm 0.01$, which corresponds to pure stream velocities in the bright spot.

4.3.4 Stroboscopic Doppler tomography

The permanent superhump phenomenon, exhibited by AM CVn, is usually explained in terms of a precession of a tidally deformed (i.e., non-circular) accretion disc. After exactly one orbital cycle, the orientation of the two stars with respect to the observer is restored, but during the orbit the eccentric disc has advanced slightly so that it takes slightly more than one orbital period to restore the orientation of the two stars with respect to the accretion disc. This beat period is then assumed to be responsible for the main photometric signal, which is usually observed to be a few percent longer than the orbital period.

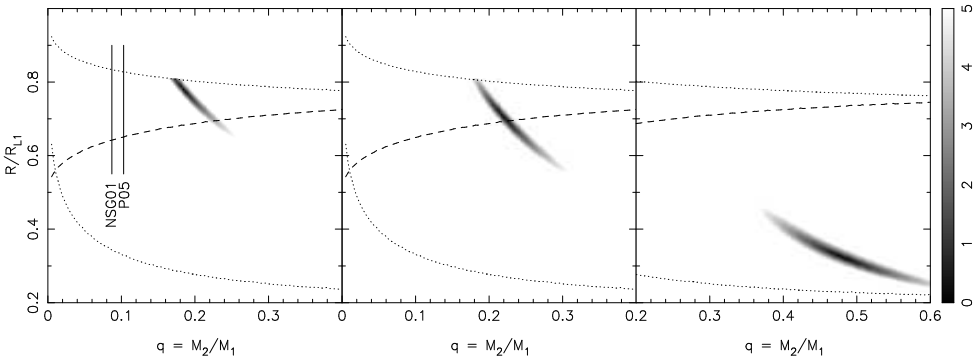

FIGURE 4.6: Mass ratio q and effective accretion disc radius R of AM CVn based on the observed velocities and phases of the central spike and the bright spot. Left: purely ballistic stream velocities; right: purely Keplerian disc velocities; centre: mixing of 80% stream and 20% disc velocities in the bright spot. The grey-scale shows the exclusion confidence levels, in standard deviations. The upper and lower dotted lines indicate the edge of the primary Roche lobe and the circularisation radius, respectively, while the dashed line shows the 3 : 1 resonance radius. The labels NSG01 and P05 indicate previous mass ratio estimates based on AM CVn's superhump behaviour (Nelemans et al., 2001; Patterson et al., 2005).

The model requires that there be a precessing accretion disc with sustained eccentricity. Furthermore, Skillman et al. (1999), among others, find the superhump cycle to be extremely stable over many thousands of orbital periods, with the superhump period always within 0.1 s of 1051.2 s and the superhump waveform remaining very stable throughout the years[1]. This implies that the shape of the disc is (semi-)stationary rather than chaotic. It further implies that the superhump phase will drift by at most 0.04 of a cycle over our ∼100-hour observing baseline, if we adopt their average superhump period of 1051.2 seconds. These two results open up the possibility of combining the large number of superhump cycles in our data-set to reconstruct the appearance of the system as a function of superhump phase.

The application of Doppler tomography as an instrument for testing the eccentric disc model is as follows. As the secondary star goes around the slowly precessing and non-circular disc, the effective radius at which the accretion stream impacts the disc will vary. Since the bright spot is caused by the free-falling stream of matter from the inner Lagrange point crashing into the edge of the accretion disc, a variation in effective accretion disc radius will lead to differences in the gas velocities of both the stream and the disc matter at the impact point. Observationally, we then expect the bright spot to show excursions in velocity space, as a function of the relative orientation of the eccentric disc and the secondary star, i.e., as a function of superhump phase.

In order to measure these excursions we must divide our spectra in a number of bins corresponding to different superhump phases, and subsequently phase-fold the spectra contained in

[1] Note that the superhump waveform is double-humped; most of the power is actually in the first harmonic at 525.6 seconds.

each bin on the orbital period. The method bears resemblance to the 'stroboscopic Doppler tomography' method employed by Marsh & Duck (1996) to disentangle the orbital and white dwarf spin periods in the magnetic accretor FO Aqr, except that we now have the orbital period of the binary and the precession period of the accretion disc.

We argue that this is in fact quite a sensitive method for measuring variations in the effective radius of the accretion disc. If we consider the simplest case of an eccentric, elliptical accretion disc, a simple estimate for the ratio of the projected apastron and periastron velocity amplitudes $v_{\rm a,p}$ as a function of the eccentricity e is

$$\frac{v_{\rm p}}{v_{\rm a}} \approx \frac{1+e}{1-e} \approx 1+2e, \quad e \ll 1. \tag{4.1}$$

A bright spot of average velocity amplitude $\overline{v} \simeq 450$ km/s, combined with a reasonable spectral resolution and signal-to-noise ratio that allow the bright spot to be measured to 10 km/s accuracy, gives an eccentricity sensitivity of $e \sim 0.01$. In practice, the excursion of the bright spot in a Doppler tomogram will be larger and the eccentricity sensitivity will correspondingly be better than this.

As an example we show in figure 4.7, by solving numerically the equation of motion for a ballistic test mass in the binary potential, how we expect the bright spot to vary as a function of superhump phase, in a binary of mass ratio $q = 0.18$, with an elliptical accretion disc of semi-major axis $R = 0.65 R_{L1}$ and eccentricity $e = 0.2$. This eccentricity value is chosen based on the simple observational model of Patterson et al. (1993) and the numerical models of Simpson & Wood (1998). The bright spot is expected to show excursions of several hundreds of km/s, indicating that eccentricities of this magnitude should be easily observable with our spectral resolution.

In our simple model we have assumed a somewhat sharp edge to the accretion disc as in e.g. Armitage & Livio (1998), such that the gradual changes in pressure along the ballistic stream do not significantly alter the depth of the stream's impact into the disc. In order to explore the possible effects of such variations, consider the pressure of the accretion stream $p_{\rm s}$,

$$p_{\rm s} = p_{\rm static} + p_{\rm dynamic} \approx p_{\rm dynamic} = \frac{1}{2}\rho v^2 \tag{4.2}$$

where ρ and v are the density and velocity of a fluid element along the stream, respectively, and $p_{\rm static}$ can be neglected since $k_B T \ll m_{\rm He} v^2$ in the free-fall regime (by definition, one could say), where v is of the order 10^2 km/s and the temperature T of the stream, set by the surface temperature of the donor star, is of the order 10^4 K. If we assume a steady ballistic flow of gas, where the scale height of matter in the flow remains fairly constant in the region just outside the disc (Lubow & Shu, 1976) since the matter does not have time to maintain hydrostatic equilibrium perpendicular to the flow, then conservation of mass gives

$$\rho \propto v^{-1} \qquad \text{(along streamline)} \tag{4.3}$$

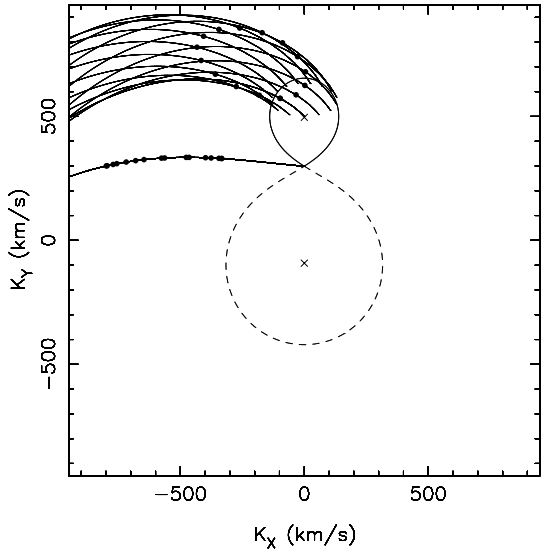

FIGURE 4.7: Simulated stroboscopic Doppler tomogram for a binary of mass ratio $q = 0.18$, accretion disc semi-major axis $R = 0.65R_{L1}$, and accretion disc eccentricity $e = 0.2$. The elliptical group of spots represent Keplerian accretion disc velocities in the bright spot, the group sticking out to the left represent ballistic accretion stream velocities, as a function of superhump phase (one full cycle shown).

so that

$$p_s \propto v \qquad \text{(along streamline)} \tag{4.4}$$

The pressure along the accretion stream thus increases linearly with velocity. In case of a 'soft' edge to the accretion disc (that is, a slowly increasing disc pressure p_d from the disc edge inwards) this could have the effect of *increasing* the ratio of observed periastron and apastron bright spot velocities for given e, as the stream impacts slightly deeper into the disc rim at periastron due to its higher pressure than it does at apastron. Thus if one employs the radius at which the bright spot occurs as the effective *in situ* accretion disc radius, and one allows the disc edge to be soft, an eccentricity measurement based on the bright spot excursion amplitude could lead to an overestimate of e, and thus to an *upper limit* for e.

4.3.5 Eccentricity of the accretion disc: the bright spot

Figures 4.8 and 4.9 show the results from our stroboscopic Doppler tomograms. In fig. 4.8 we plot eight Doppler tomograms that together cover one full superhump period. In order to improve on the signal-to-noise ratio of the individual maps we combined the data (in velocity space) of four lines that show a clear bright spot in the trailed spectra, namely He I 4387, He I 4471, Mg II 4481 and He I 4921 (figures 4.2 & 4.3). Figure 4.9 shows the measured excursions

of the bright spot as a function of superhump phase, for 16 superhump phase bins, connected by a line, where the bright spot centroids have been determined in the same way as in section 4.3.2. Here, the 16 phase bins oversample the superhump cycle by a factor of two, so that each bin contains 1/8th of the data as in figure 4.8.

Based on the observed bright spot excursion amplitude of less than 100 km/s (see figure 4.9), we constrain the effective eccentricity of the outermost part of the accretion disc to $e = 0.04 \pm 0.01$, where we define the 'effective' eccentricity as that which would cause a simple elliptical disc to give rise to the same bright spot excursion amplitude in velocity space. The error on this value can be rather small because the method of measurement is insensitive to the accretion disc's semi-major axis (or average radius), and to whether the bright spot represents stream or disc velocities (see also figure 4.7). In case the bright spot velocity is a *variable* mix of the disc and stream velocities, the derived eccentricity can be an overestimate.

Despite the rather large error bars in the left panel of figure 4.9, at least relative to the small movement of the bright spot, the disc appears to be more complex than the simple ellipse which it is often pictured to be in explaining the superhump phenomenon. Detailed numerical simulations, e.g. by Simpson & Wood (1998), show that the accretion disc in a permanent superhump system like AM CVn is in fact most likely of irregular shape. Not only that, the disc is also predicted to change shape during a superhump period, only to return to its original shape after one full superhump cycle – therefore, the disc could *in principle* be exhibiting strong changes in radius at the other side of the accreting star, where the mass stream cannot be used to probe its effective radius. The changes in effective radius of the accretion disc *might* thus be larger than is revealed by the excursions of the bright spot.

4.3.6 Eccentricity of the accretion disc: integrated disc profile

Figure 4.10 shows trailed spectra and Doppler tomograms of He II 4686 as a function of superhump phase. The He II 4686 line was chosen because it clearly shows emission in the average spectrum (fig. 4.1), which is commonly used as a tracer of locally enhanced dissipation in accretion discs, for instance in searches for spiral shocks in outbursting dwarf novae. A sinusoid with the phase and amplitude of the central spike – i.e. the presumed motion of the accretor – has been shifted out of the spectra to leave the net kinematic signal of the matter in the disc orbiting the accretor. The ionised helium emission profile is clearly variable on the superhump period: the emission is asymmetric and the degree of asymmetry is changing (see also figure 4.9). These general features agree with the predictions of Simpson & Wood (1998).

It can furthermore be deduced that the He II 4686 emission is strongest where the effective radius of the disc is smallest. The right panel in figure 4.9 shows both the bright spot velocity amplitude and the angle between the bright spot and the centroid of He II 4686 emission, as a function of superhump phase. This angle is given in spatial coordinates – for the transformation of velocity into spatial coordinates we assume roughly ballistic stream velocities for the bright spot based on the results of section 4.3.3, and roughly Keplerian disc velocities for the He II 4686 emission. Despite the rather large error bars, there appears to be a trend whereby the

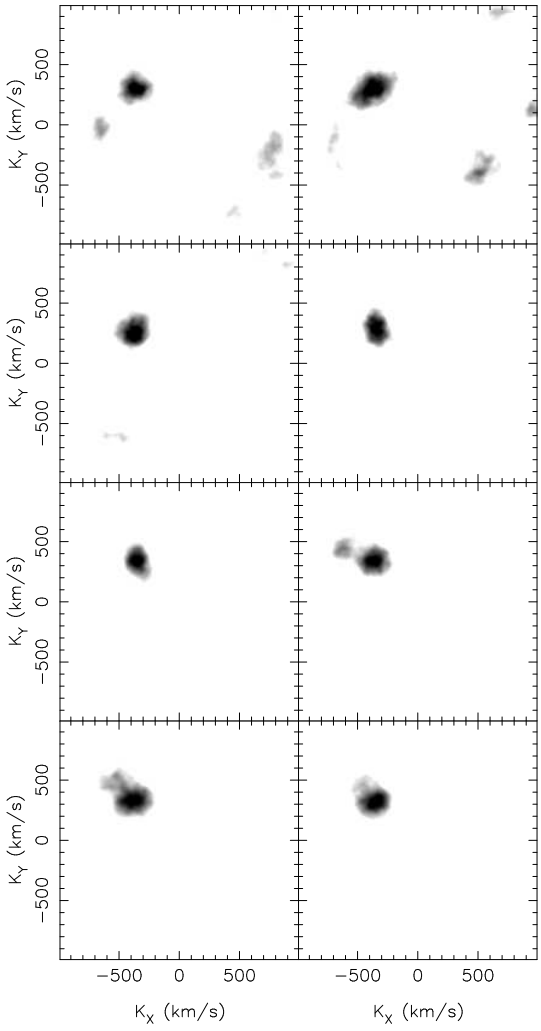

FIGURE 4.8: Doppler tomograms showing the bright spot as a function of superhump phase. One full cycle is shown from left to right, top to bottom. The bright spot is visible at all superhump phases, and shows no large excursions in velocity space.

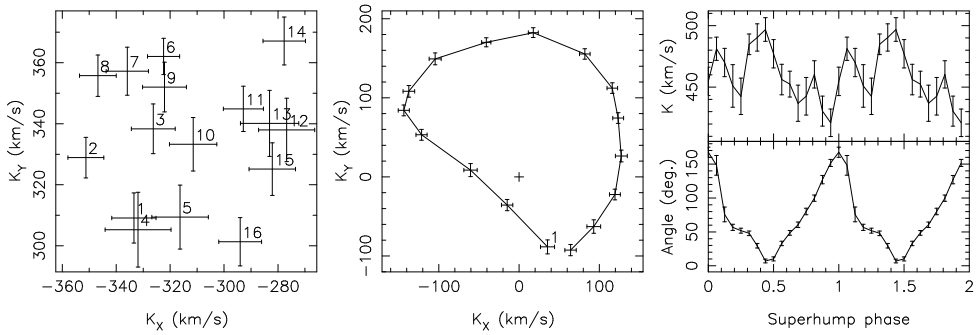

FIGURE 4.9: The accretion disc as a function of superhump phase. Left: the measured bright spot velocities in 16 superhump phase bins. Middle: the measured He II 4686 emission centroids, again in 16 phase bins. Right: the bright spot velocity amplitude, together with the angle (in spatial coordinates) between the bright spot and the He II 4686 emission centroid, as a function of superhump phase. In this last panel we assume approximately stream velocities in the bright spot and Keplerian velocities for the He II 4686 emission.

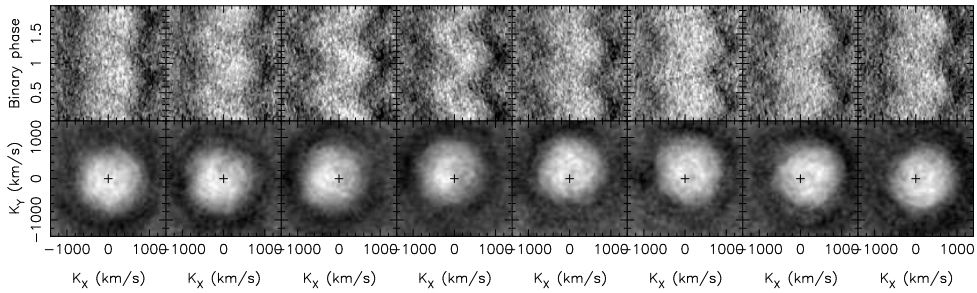

FIGURE 4.10: Trailed spectra and linear back-projection Doppler tomograms of the He II 4686 line as a function of superhump phase. One full superhump cycle is shown from left to right.

maximum bright spot velocity amplitude (which should correspond to the smallest effective disc radius) corresponds to alignment of the bright spot with the He II emission centroid, while the minimum bright spot velocity (i.e. largest effective disc radius) corresponds to anti-alignment.

These findings again agree with the numerical simulations of Simpson & Wood (1998). Their analysis of the changes in internal energy in the disc as a function of superhump cycle, too, showed that energy production was highest where the disc radius was smallest. This may not be that surprising since streamlines of matter in the disc will be squeezed more closely together towards a region of smaller disc radius, causing extra viscous dissipation. We may tentatively conclude that cooling proceeds on a timescale less than the orbital period of the matter in the disc, which is a few minutes.

4.4 Discussion

4.4.1 A central spike in AM CVn?

The mysterious central spike has so far been observed in long-period, low mass transfer rate AM CVn stars, where the accreting white dwarf dominates the optical flux. It is thought to originate on (or very close to) the surface of the accreting white dwarf, since the spike perfectly tracks the expected movement of the accreting white dwarf relative to the bright spot in the accretion disc. In addition, there is no accretion disc component that is expected to move at such low velocities, and the phase of the spike relative to the bright spot does not match the phase of the secondary. See Morales-Rueda et al. (2003) for a detailed analysis of the central spike in GP Com.

The kinematic feature observed in the He I 4471 line in AM CVn, as presented here, has all the characteristics for being the perfect analogy to the central spike in GP Com (Morales-Rueda et al., 2003), V396 Hya (Steeghs et al. in preparation) and SDSS J124058.03−015919.2 (Roelofs et al., 2005): (1) it is intrinsically redshifted; (2) it agrees in amplitude with the expected velocity amplitude of the accreting white dwarf (and not with any other binary component's velocity amplitude); and (3) it agrees in phase with the expected phase of the accreting white dwarf, relative to the bright spot. We therefore conclude that it is *very* likely that it is the central spike.

The mass ratio for AM CVn implied by the central spike is significantly higher than previously thought, although there has been a study by Pearson (2003) suggesting, in fact, a mass ratio $q \sim 0.19 - 0.25$ based on a model in which the secondary star is moderately magnetic. The motivation for that study was to try to reconcile the mass ratio with the K-velocity of the He II 4686 emission line measured (but discarded) by Nelemans et al. (2001), which suggested a mass ratio in this regime. It is clear from this work however, in particular figure 4.10, that the measured K-velocities of the He II 4686 emission indeed *cannot* be used reliably as an indicator for the motion of the accretor, since the apparent kinematic signal could easily be dominated by the eccentricity of the disc rather than the actual motion of the primary.

4.4.2 Implications for AM CVn's formation channel

One of the long-standing questions regarding the AM CVn stars is how they are formed. Theoretically, they can be formed in both double-degenerate and single-degenerate configurations: Roche-lobe overflow from a white dwarf onto another (more massive) white dwarf (e.g. Nelemans et al. 2001), or from a helium-burning star onto a white dwarf (Iben & Tutukov, 1991). A third suggested formation channel is Roche-lobe overflow from an evolved main-sequence star onto a white dwarf (Podsiadlowski et al., 2003), where mass transfer starts by the time hydrogen core burning ends. This latter scenario, however, has the problem of leaving significant amounts of hydrogen, while our high-S/N average and phase-binned spectra show exclusively helium and metals. For the other two formation channels, the main discriminator is the mass

of the secondary star: in the helium-star channel, one expects a relatively hot and massive, only partially degenerate secondary, while in the double-degenerate channel, one expects a 'cold' degenerate donor star.

The significantly higher mass ratio found for AM CVn in this paper has important implications for the nature of the donor star, and hence for AM CVn's formation channel, as it suggests a relatively massive donor. If we combine the orbital period with the mass–radius relation for a relatively 'cold' (core temperature $T_c \leq 10^6$ K), degenerate helium white dwarf as used in Nelemans et al. (2001) and refined recently in Deloye et al. (2005), we get a secondary mass $M_2 \approx 0.035 M_\odot$ and hence, through our minimum mass ratio of $q = 0.18 \pm 0.01$, a maximum primary mass of only $M_1 = 0.19 M_\odot$. This is *very* low; the maximum combined mass of $M_1 + M_2 = 0.22 M_\odot$ would, for instance, be significantly lower than the average value $M_1 + M_2 = 0.8 M_\odot$ found in detached WD–WD binaries (e.g. Nelemans et al. 2005). This casts doubt on the possible white dwarf (WD) nature of the donor star, and thereby on the double-degenerate formation channel for AM CVn, unless the white dwarf donor was still very hot upon Roche-lobe overflow – that is, unless mass transfer started shortly after the second common-envelope phase.

Concurrent with the measurement of AM CVn's mass ratio presented here, it was discovered that AM CVn's distance is larger than expected, through an *HST/FGS* parallax measurement ($\pi = 1.65 \pm 0.30$ mas, Roelofs et al. in preparation). This means a smaller absolute magnitude M_V and thus, since we expect the accretion disc to dominate the optical flux, a higher accretion luminosity.

In order to link the observed M_V to the mass of the secondary M_2, we proceed in the same way as in Deloye et al. (2005). We assume conservative mass transfer that is driven entirely by loss of angular momentum due to the emission of gravitational waves and, since accretion proceeds via an accretion disc, we assume that all angular momentum carried by the transferred matter is fed back to the orbit. We then have

$$\frac{\dot{M}_2}{M_2} = \frac{\dot{J}}{J} \frac{2}{\zeta_2 + 5/3 - 2q} \tag{4.5}$$

where J is the orbital angular momentum, $\dot{J}$ is the orbital angular momentum loss rate

$$\frac{\dot{J}}{J} = -\frac{32}{5} \frac{G^3}{c^5} \frac{M_1 M_2 (M_1 + M_2)}{a^4} \tag{4.6}$$

due to the emission of gravitational waves (Landau & Lifschitz, 1971), and

$$\zeta_2 \equiv \frac{\mathrm{d} \log R_2}{\mathrm{d} \log M_2}. \tag{4.7}$$

We take $\zeta_2 = -0.06$ for $M_2 < 0.2 M_\odot$ as in Nelemans et al. (2001), based on evolutionary calculations for a mass-losing helium-burning star by Tutukov & Fedorova (1989). Clearly

Parameter	Value
$P_{\rm orb}$ (s)	1028.7322 ± 0.0003 (Skillman et al., 1999)
q	0.18 ± 0.01
$M_1(M_\odot)$	0.68 ± 0.06
$M_2(M_\odot)$	0.125 ± 0.012
$\dot{M}_2(M_\odot/\mathrm{yr})$	$6.7^{+1.9}_{-1.3} \cdot 10^{-9}$
i (degrees)	43 ± 2
d (pc)	606^{+135}_{-93} (Roelofs et al. in prep.)

TABLE 4.4: The collection of system parameters for AM CVn.

$\zeta_2 = 0$ around the point where helium burning stops, while it may be somewhat closer to $\zeta_2 = -0.19$ along the semi-degenerate part of the track for a secondary that is more helium depleted, as found by Savonije et al. (1986). This represents a $\lesssim$10% uncertainty in eq. (4.5).

The last step is to calculate the bolometric luminosity L, for which we use

$$L = \frac{1}{2}\dot{M}_2\big(\Phi(L_1) - \Phi(R_1)\big) \tag{4.8}$$

where Φ is the common Roche potential, at the inner Lagrange point L_1 and the surface of the accretor R_1. This states that the matter in the disc stays virialised during the accretion process, which should hold for approximately Keplerian particle orbits.

Figure 4.11 shows M_V as a function of M_2 for $q = 0.18$, $\zeta_2 = -0.06$ and a bolometric correction BC $= -3.0$ (see below). The lower limit to M_2 is given by the requirement that the system does not eclipse. The data point $M_V = 5.0 \pm 0.4$ as determined from our aforementioned *HST* parallax is overplotted, which yields a secondary mass $M_2 = 0.125 \pm 0.012\,M_\odot$ and, via $q = 0.18 \pm 0.01$, a primary mass $M_1 = 0.68 \pm 0.06\,M_\odot$. The corresponding mass transfer rate is $\dot{M}_2 = 6.7^{+1.9}_{-1.3} \cdot 10^{-9} M_\odot$/yr, and the inclination of the binary comes out at $i = 43 \pm 2°$. Table 4.4 lists the system parameters for AM CVn in convenient tabular form.

Our results have been corrected for the geometric effect that the 'apparent absolute magnitude' (Warner, 1995) of an accretion disc depends on the inclination. A factor

$$\Delta M_V(i) = -2.5 \log\left(\frac{\cos i}{1/2}\right) \tag{4.9}$$

has been taken into account as the correction from apparent absolute magnitude to absolute magnitude, where the factor $1/2$ represents the direction-averaged fraction of the disc area seen by the observer, $\langle \cos i \rangle$. We neglect the (unknown) effect of limb darkening.

In converting the bolometric luminosity $M_{\rm bol}$ obtained from equation (4.8) to an absolute visual magnitude M_V, the bolometric correction is of some importance. AM CVn's spectral energy

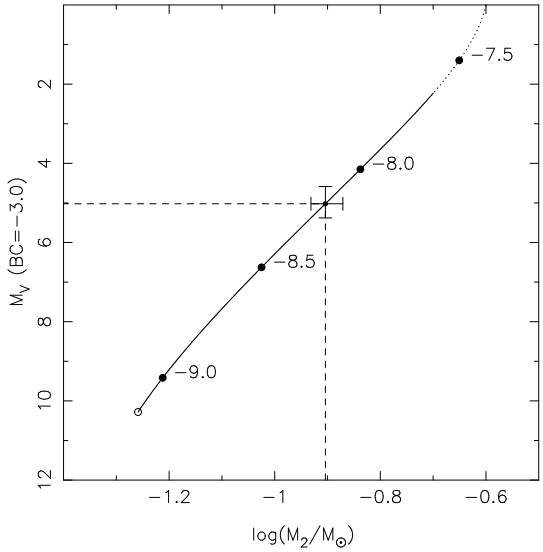

FIGURE 4.11: Relation between M_2 and M_V for AM CVn. Our measurement of the absolute magnitude M_V and its implications for the secondary mass M_2 are indicated by the dashed line. The open circle represents the minimum secondary mass for which the system does not eclipse (assuming a disc that extends to the 3 : 1 resonance radius); the dotted line, towards larger M_2 and smaller M_V, shows the helium-burning regime where we expect our assumptions regarding the mass-radius relation to break down (>10% error). The labelled dots indicate $\log \dot{M}_2$ in $M_\odot$/yr.

distribution from the far-UV to the optical (Roelofs et al. in preparation; see also Nasser et al. 2001) indicates that it is dominated by a blackbody of $\simeq 30,000$ K. This corresponds to a BC of -3.0, with an estimated error of 0.3. If we calculate the minimum temperature the accretion disc must have in order to be able to radiate away the required luminosity (for any given $M_{1,2}$ we know the maximum radiating surface of the disc), we find $T_{\rm disc} \gtrsim 30,000$ K for accretion rates $\dot{M}_2 \geq 4 \cdot 10^{-9} M_\odot$/yr. The BC we use is thus self-consistent with the accretion rate we derive; in particular, it seems unlikely that we are overestimating the mass transfer rate due to an overestimate of the BC.

Summarising, we have two independent pieces of evidence suggesting a relatively massive donor star – the large mass ratio and the large luminosity. If we compare our results to evolutionary models for helium star and white dwarf secondaries as given by Nelemans et al. (2001), we see that our derived secondary mass is compatible with the secondary being the semi-degenerate core of a formerly helium burning star, while a 'cold' degenerate donor star is ruled out. See figure 4.12. The secondary mass $M_2 = 0.125 M_\odot$ is close to the turn-off mass for helium burning, which lies at $M_2 \sim 0.16 M_\odot$ (Savonije et al., 1986; Tutukov & Fedorova, 1989). We conclude that it is very likely that AM CVn formed through an evolutionary channel in which the donor star was, upon the start of Roche-lobe overflow, still burning helium. These observations thus

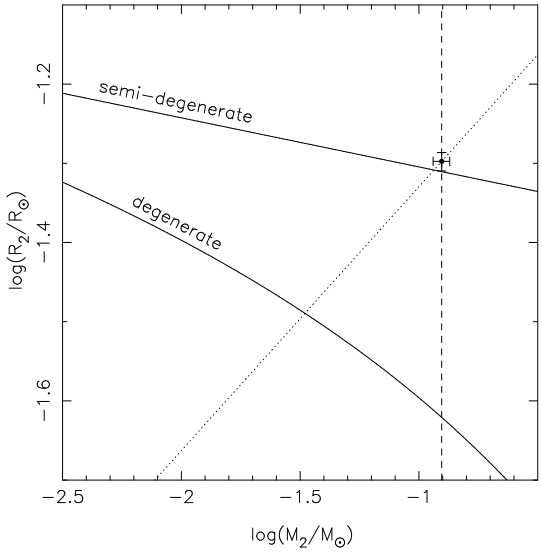

FIGURE 4.12: Relation between M_2 and R_2 for AM CVn. The upper and lower solid line represent the evolutionary tracks for semi-degenerate helium star and for cold white dwarf secondaries, respectively (Nelemans et al., 2001; Tutukov & Fedorova, 1989). The dotted line is the requirement that the secondary star fills its Roche lobe. The dashed line represents our measurement of M_2. The data favour a semi-degenerate helium star secondary, rather than a white dwarf.

provide the first observational evidence that the helium star evolutionary channel contributes to the AM CVn population.

4.4.3 Implications for AM CVn's gravitational-wave signal

We expect the orbit of AM CVn to be circular, so that the gravitational wave polarisation amplitudes A_+ and $A_\times$ at twice the orbital frequency, f, become (e.g. Timpano et al. 2006)

$$A_+ = 2\frac{(G\mathscr{M})^{5/3}}{c^4 d}(\pi f)^{2/3}\left(1+\cos^2 i\right) \tag{4.10}$$

$$A_\times = -4\frac{(G\mathscr{M})^{5/3}}{c^4 d}(\pi f)^{2/3}\cos i \tag{4.11}$$

where $\mathscr{M} = (M_1 M_2)^{3/5}/(M_1+M_2)^{1/5}$ is the so-called chirp mass, i is the inclination of the binary, and d its distance. Defining the strain amplitude

$$h = \left(\frac{1}{2}\left(A_+^2 + A_\times^2\right)\right)^{1/2} \tag{4.12}$$

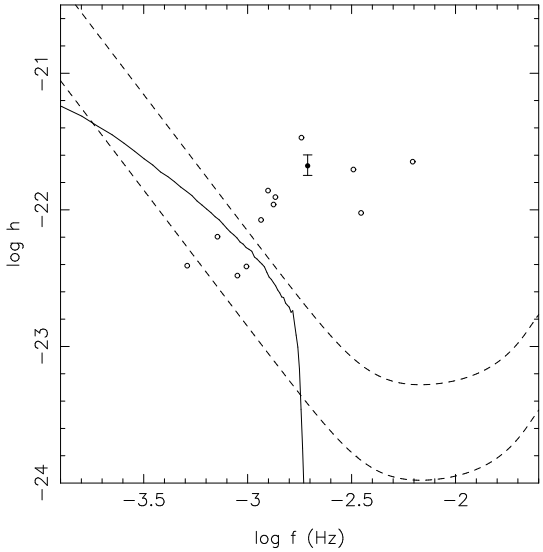

FIGURE 4.13: Gravitational-wave strain amplitude of AM CVn (solid circle). The upper and lower dashed lines show the design sensitivities of *LISA* for a S/N of 5 and 1, respectively, in one year of data-collecting (Larson et al., 2000). The solid line is a population synthesis prediction for the confusion-limited Galactic background (Nelemans et al., 2004). The open circles represent 'known' AM CVn stars that are as yet not well-constrained in terms of either distance or component masses, or both.

and converting to more convenient solar units, one finds

$$h = 2.84 \cdot 10^{-22} \sqrt{\cos^4 i + 6\cos^2 i + 1} \times \left(\frac{\mathscr{M}}{M_\odot}\right)^{5/3} \left(\frac{P_{\rm orb}}{1\,{\rm hr}}\right)^{-2/3} \left(\frac{d}{1\,{\rm kpc}}\right)^{-1} \tag{4.13}$$

Filling in the numbers derived above gives $h = 2.1^{+0.4}_{-0.3} \cdot 10^{-22}$. Figure 4.13 shows the estimated strain amplitudes and frequencies of the 'known' AM CVn stars. AM CVn itself is the first potential *LISA* source which is sufficiently well-constrained that we can plot error bars with some confidence, and we see that it stands out significantly above both the instrumental design sensitivity and the estimated confusion-limited Galactic background due to, mainly, detached WD–WD binaries.

4.4.4 The superhump excess–mass ratio relation

It is understood from numerical simulations, and it is observed in outbursting dwarf novae and nova-likes, that there exists a relation between the superhump period excess ϵ and the mass ratio

q of the binary. See Patterson et al. (2005), and references therein, for an overview including the very latest empirical work on the $\epsilon(q)$ relation. In short, they conclude that for hydrogen-rich systems,

$$\epsilon(q) = 0.18q + 0.29q^2 \tag{4.14}$$

For AM CVn, this results in $q = 0.10$ based on the photometry of Skillman et al. (1999). Although it is unknown what the intrinsic spread in $q(\epsilon)$ is, it appears from figure 9 in Patterson et al. (2005) to be quite low, no more than about 0.01. This means that the $q(\epsilon)$ for AM CVn deviates significantly from our minimum kinematic mass ratio $q = 0.18 \pm 0.01$.

Of course, the superhump excess ϵ may depend on more parameters than just the mass ratio q; it is quite conceivable that the helium nature of AM CVn may be of influence. A recent study by Goodchild & Ogilvie (2006) indicates, for instance, quite a significant dependency of ϵ on the thickness of the accretion disc, where thicker discs lead to smaller superhump period excesses for a given mass ratio. If this effect should be at play, our results would suggest a physically thicker disc in AM CVn compared to discs in hydrogen-rich systems of the same mass ratio.

Although AM CVn represents only a single data point, it seems advisable to apply the empirical superhump excess–mass ratio relation with caution for such ultra-compact binaries. An obvious test would be to obtain the mass ratio in HP Librae, the other known helium nova-like, and check whether it, too, shows a discrepancy with relation (4.14).

4.4.5 Size and eccentricity of the accretion disc

In our derivation of the minimum mass ratio $q = 0.18 \pm 0.01$, we have assumed a maximum accretion disc radius equal to the minimum radius of the primary Roche lobe. It is customary to assume a slightly more stringent limit on the maximum accretion disc radius, caused by tidal truncation of the disc. See e.g. Warner (1995) and references therein. For reference, we show in figure 4.14 the often-used tidal truncation radius

$$\frac{R_T}{a} = \frac{0.6}{1+q} \qquad (0.03 < q < 1.0) \tag{4.15}$$

for an inviscid flow, which is indeed smaller than the full minimum Roche lobe radius we assume. However, since this tidal truncation radius depends, in particular, on the unknown viscosity of the matter in the disc (and increasing with viscosity), we have not used it as a hard upper limit to the disc's radius. Interestingly, one sees that the best-fitting accretion disc radius we derive for ballistic stream velicities in the bright spot (reproduced in figure 4.14) lies very close to, but slightly above, the tidal truncation radius (4.15).

The effective eccentricity value $e = 0.04 \pm 0.01$ we derive for the outermost part of the disc, from the stream–disc impact spot, is smaller than typical values $e \sim 0.1-0.2$ found in numerical simulations. Although the eccentricity is not one of the observables that is usually quoted in numerical studies (the resulting superhump period excess is often the only given quantity), it

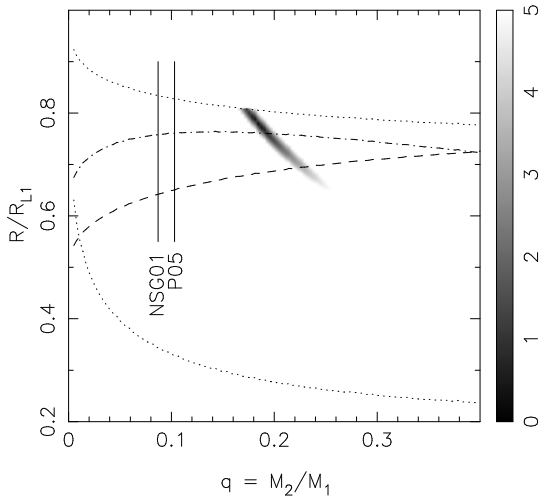

FIGURE 4.14: Same as the left panel in figure 4.6, but now including the tidal truncation radius (eq. (4.15)) for an inviscid disc, indicated by the dot-dashed line.

can be inferred that the effective eccentricity we find is significantly smaller than that found by Simpson & Wood (1998) in their simulations of discs in AM CVn stars.

A possible explanation would be that tidal truncation, discussed in the previous paragraph, acts to circularise the disc at the outer edge to some extent by effectively removing particles from the most eccentric orbits there. This tidal truncation process is essentially a competition between viscosity transporting angular momentum outwards and tidal forces 'dissipating' this angular momentum increasingly strongly with radius, and predictions about this tidal truncation process would thus be affected by our lack of understanding of the viscosity in accretion discs.

4.4.6 Spin of the accretor and tidal synchronisation

If the central spike originates from the surface of the accreting white dwarf, in particular if it rotates with the accretor, its width puts an interesting constraint upon the accretor's spin. The central spike is unresolved in our data, and we therefore place an upper limit of ∼45 km/s, equal to our formal spectral resolution, on the FWHM of the feature. For the system parameters derived for AM CVn, corotation with the orbit would imply a projected equatorial velocity of ∼36 km/s. The central spike we observe is thus consistent with a corotating primary, while significantly faster rotation is ruled out.

We can estimate the tidal synchronisation timescale of the accretor from this constraint. For simplicity, we assume that AM CVn has been steadily accreting matter at a rate $\dot{M}_2 \sim 7 \cdot 10^{-9} M_\odot$/yr for a long time. As long as the accretor is near corotation with the orbit, the spin-

up timescale τ of the primary due to the accretion of disc matter can be written as

$$\tau = \frac{\omega}{\dot{\omega}} \approx \frac{2\pi}{P_{\rm orb}} k \sqrt{\frac{M_1}{G}} \frac{R_1^{3/2}}{\dot{M}_2} \tag{4.16}$$

where $k \approx 0.18$ (see Marsh et al. 2004) is the moment of inertia factor ($k = 2/5$ for a solid sphere), and ω is the angular velocity of the accretor. Requiring that tidal synchronisation proceeds on timescales similar to or shorter than the accretion-induced spin-up of the primary, gives a maximum tidal synchronisation timescale $\tau_s \lesssim 2 \cdot 10^5$ yr.

A key question in binary evolution theory is whether two white dwarfs, upon Roche-lobe overflow at orbital periods of a few minutes, can manage to stabilise the accretion process and avoid a merger by feeding back angular momentum from the spun-up accretor to the orbit. This has profound implications for the number of systems that may survive the initial phase of mass transfer, when accretion proceeds at a high rate of $\dot{M}_2 \sim 10^{-6} M_\odot$/yr (Marsh et al., 2004).

Although its absolute magnitude is highly uncertain from a theoretical point of view, tidal synchronisation is understood to scale with the orbital separation and the radius of the accretor as

$$\tau_s \propto \left(\frac{M_1}{M_2}\right)^2 \left(\frac{a}{R_1}\right)^6 \tag{4.17}$$

(see, e.g., Marsh et al. 2004). This means that, for a three-minute white dwarf binary in which Roche-lobe overflow is about to commence, the tidal synchronisation timescale will be at least a factor 10^3 shorter than for AM CVn, or $\tau_s \lesssim 200$ yr. This is an interesting result since it is exactly the regime that is needed for an appreciable fraction of binary white dwarf systems to survive the initial phase of mass transfer. See Marsh et al. (2004), in particular their figure 11.

If the central spike is thus associated with the accreting white dwarf as we think, it implies a tidal synchronisation timescale that is short enough to make the double-degenerate formation channel for AM CVn stars viable (Nelemans et al., 2001). It would thereby also increase the viability of the direct-impact accretor scenario for the ultra-compact binaries RX J0806.3+1527 and V407 Vul (Marsh & Steeghs, 2002).

Chapter 5

HST/FGS parallaxes of AM CVn stars and astrophysical consequences

G. H. A. Roelofs, P. J. Groot, G. F. Benedict, B. E. McArthur, D. Steeghs, L. Morales-Rueda, T. R. Marsh and G. Nelemans

Submitted to The Astrophysical Journal

Abstract. We present absolute parallaxes and relative proper motions for five AM CVn stars, which we obtained using the Fine Guidance Sensors on board the *Hubble Space Telescope*. Our parallax measurements translate into distances $d_{\mathrm{AMCVn}} = 606^{+135}_{-93}(+49)$ pc; $d_{\mathrm{HPLib}} = 197^{+14}_{-12}(+3)$ pc; $d_{\mathrm{CRBoo}} = 337^{+44}_{-35}(+14)$ pc; $d_{\mathrm{V803Cen}} = 347^{+32}_{-27}(+9)$ pc; and $d_{\mathrm{GPCom}} = 75^{+2}_{-2}(+0)$ pc, where the numbers in parentheses are the estimated Lutz–Kelker bias corrections. From these distances we estimate the space density of AM CVn stars and suggest that previous estimates have been too high by about an order of magnitude. We also infer the mass accretion rates which allows us to constrain the masses of the donor stars, and we show that relatively massive, semi-degenerate donor stars are favored in all systems except GP Com. Finally, we give updated estimates for their gravitational-wave signals, relevant for future space missions such as the proposed *Laser Interferometer Space Antenna (LISA)*, based on their distances and the inferred masses of the binary components. We show that all systems but GP Com are excellent candidates for detection with *LISA*.

5.1 Introduction

The AM CVn stars are white dwarfs (WDs) accreting matter from a white-dwarf-like companion, constituted of helium with traces of metals. Because of their helium-dominated nature they exist in ultra-compact configurations, with orbital periods ranging from about one hour down to ten, possibly even five, minutes. See Warner (1995) and Nelemans (2005) for recent reviews.

Several evolutionary channels that could contribute significantly to the AM CVn population have been proposed. The first is stable Roche-lobe overflow in a (formerly detached) double white dwarf binary, when the two white dwarfs are brought together by angular momentum loss due to the emission of gravitational waves (the WD channel; see Nelemans et al. 2001). The second is Roche-lobe overflow from a helium star onto a white dwarf, followed by a period minimum around ten minutes, caused by the quenching of helium fusion and the donor star becoming semi-degenerate – equivalent to the orbital period minimum in the hydrogen-rich Cataclysmic Variables (CVs) (the helium star channel; Iben & Tutukov 1991). In a third scenario, a hydrogen main sequence star starts mass transfer onto a white dwarf right at the time when its core becomes depleted of hydrogen, shifting the normal CV orbital period minimum down to, again, about ten minutes depending on the level of hydrogen depletion (the evolved-CV channel; Podsiadlowski et al. 2003).

Determining which of these evolutionary channels actually produce AM CVn stars, and in what numbers, has been a long-standing problem. An important observable is the distance to known AM CVn stars: this helps in determining their space density, and their absolute magnitudes contain important information about the rate at which they accrete matter, which in turn constrains the masses of the donor stars.

In this paper we present *Hubble Space Telescope (HST)* parallaxes of five AM CVn stars, ranging from 17 to 46 minutes in orbital period. They were selected on their average brightness ($V < 16$) because of the source brightness limitations of the Fine Guidance Sensors (FGS). All five systems accrete through an accretion disk. The shortest orbital period systems AM CVn and HP Lib, at 17 and 18 minutes respectively, contain a stable disk that appears optically thick with shallow helium absorption lines, while the longest-period system GP Com, at 46 minutes, has a stable disk that appears optically thin with strong helium emission lines. The two intermediate systems under consideration, CR Boo and V803 Cen at orbital periods of 24 and 27 minutes, display transitions between high and low accretion disk states, with the disk changing from absorption-line to emission-line states and the luminosity dropping by as much as five magnitudes. This is presumably caused by a thermal instability in their disks (Tsugawa & Osaki, 1997). Photometrically, these AM CVn stars thus behave much like the well-studied CVs (e.g. Patterson et al. 1997, 2000).

The outline of this paper is as follows. We describe the observations and data reduction in Section 5.2, and present the parallaxes and absolute magnitudes in convenient tabular form in Section 5.3. We then discuss the implications of these results for the space density of AM CVn stars, for their mass accretion rates and the masses of the components, and for their gravitational-wave signals in Section 5.4.

5.2 Observations and data reduction

Ten sets of astrometric data were acquired with the Fine Guidance Sensors on board *HST* for each of our five science targets. At each epoch we measured several reference stars and the target multiple times to correct for intra-orbit drift. We obtained these sets in pairs typically separated by a week. Each complete data aggregate spans ∼1.5 years, except for GP Com, where a servicing mission forced a one-year slip of an observation at one maximum parallax factor. Table 5.3 contains the epochs of observation and measured photometry for each AM CVn star. The data were reduced and calibrated as detailed in Benedict et al. (2002a, 2002b, 2005), McArthur et al. (2001), and Soderblom et al. (2005).

Because the parallaxes determined for the AM CVn stars will be measured with respect to reference frame stars which have their own parallaxes, we must either apply a statistically derived correction from relative to absolute parallax (van Altena et al., 1995) or estimate the absolute parallaxes of the reference frame stars listed in Table 5.4. We choose the second method, as it yields a more direct (less Galaxy-model dependent) way of determining the reference star absolute parallaxes.

In principle, the colors, spectral type, and luminosity class of a star can be used to estimate the absolute magnitude, M_V, and V-band absorption, A_V. The absolute parallax is then simply,

$$\pi_{\rm abs} = 10^{-(V-M_V+5-A_V)/5} \tag{5.1}$$

To obtain the spectral type and luminosity class of all reference stars, which is essential for estimating their absolute parallaxes, we combine existing photometric data from the Two-Micron All Sky Survey (2MASS), proper motions from the USNO CCD Astrograph Catalog (UCAC2), and ground-based spectroscopic follow-up from the 2.5-m Isaac Newton Telescope (with IDS), the 4.2-m William Herschel Telescope (with ISIS), the 6.5-m Magellan–Baade telescope (with IMACS), and the FLWO 1.5-m (with FAST), where the acronyms in parentheses are the names of the spectrographs used. The spectra typically have a ∼5 Å resolution and a wide spectral range, suitable for classification purposes from early- to late-type stars. Table 5.5 lists the spectral types and luminosity classes we obtain for our reference stars based on independent photometric and spectroscopic classification. Estimated classification uncertainties are used to estimate the errors on the $m - M$ values in that table.

Assuming an $R = 3.1$ Galactic reddening law (Savage & Mathis 1979), we derive A_V values by comparing the measured colors (Table 5.6) with intrinsic $(V-K)_0$ colors from Bessell & Brett (1988) and Cox (2000). The resulting A_V values are collected in Table 5.7, from which we calculate a field-wide average A_V to be used in equation 1. The resulting reference star parallax estimations are listed in Table 5.5.

5.3 Results

5.3.1 Parallaxes and absolute magnitudes

Table 5.1 lists the absolute parallaxes, proper motions, and absolute magnitudes for the five AM CVn stars. To determine the average absolute magnitudes, we first derived average values for the apparent magnitudes of our objects. AM CVn, HP Lib and GP Com have never been observed to show brightness variations larger than about a tenth of a magnitude around their mean, and it is commonly assumed that their accretion disks are in stable states of high (AM CVn, HP Lib) or low (GP Com) mass transfer, such that the thermal instabilities that may trigger transitions between different brightness states do not occur. We can therefore use our accurate FGS photometry (Table 5.3), which consists of 10 visits per object well separated in time, to directly derive average apparent magnitudes for these three systems. The two other objects, V803 Cen and CR Boo, are known to show complex brightness variations, as also evidenced by our FGS photometry (Table 5.3). For these we use the results of extensive photometric monitoring campaigns conducted by Patterson et al. (1997, 2000) to estimate time-averaged apparent magnitudes. The results are collected in Table 5.1.

When using a trigonometric parallax to measure a distance or distance modulus, a correction should be made for the Lutz–Kelker (LK) bias (Lutz & Kelker, 1973). This LK bias occurs when the number of stars in a population significantly increases (or decreases) with distance around the measured distance for a certain object in the population, both due to an increase in the sampled volume with distance and a decrease in the population space density with distance. This can be corrected for if one knows the scale height of the population under consideration, which for the AM CVn stars is a problem.

GP Com, together with its twin V396 Hya, most likely belongs to a (potentially large) halo population of old and very metal-poor AM CVn stars (Marsh, 1999; Morales-Rueda et al., 2003). For the shorter-period systems, we have no indication that they belong to a halo population. Significant amounts of metals have been detected in AM CVn, HP Lib and V803 Cen (Roelofs et al. 2006b,c), suggesting a thin or possibly thick disk origin. Similar data is as yet unavailable for CR Boo, but several more recently discovered AM CVn stars – SDSS J124058.03-015919.2 (Roelofs et al., 2005), and 'SN 2003aw' (Roelofs et al., 2006a) – show abundances of metals in optical spectra (typically Fe, Mg and Si) that are compatible with solar values. There is thus no evidence that the AM CVn stars in the solar neighborhood in general belong to a halo population. In addition, none of our objects show particularly large proper motions, except for GP Com (see Table 5.1). We thus assume that AM CVn, HP Lib, CR Boo and V803 Cen all belong to a disk population.

We model this population with a thin disk component of moderate age, with a scale height $h_{z,\mathrm{thin}} = 300\,\mathrm{pc}$, plus an older thick disk component of scale height $h_{z,\mathrm{thick}} = 1250\,\mathrm{pc}$ that contributes 2% at $z = 0$, where z is the distance from the Galactic plane. The resulting LK bias corrections on the distances and distance moduli are given in Table 5.1. The errors on these corrections have been estimated by varying the modeled thin disk scale height from

200–500 pc. The interesting object is AM CVn: adopting a halo distribution for AM CVn in particular would yield a significantly larger LK bias correction of ≈ -0.4 on its distance modulus, thanks to its small parallax and high Galactic latitude. For the other four systems, a halo rather than disk population would increase the LK bias by at most -0.03, rendering the induced error negligible for these systems. All results, including the final absolute magnitudes we obtain for the five stars, are listed in Table 5.1.

5.4 Discussion

5.4.1 Previous distance measurements

Ground-based parallax measurements

Two of our targets (AM CVn and GP Com), as well as one other member of the AM CVn class (V396 Hya) have a measured ground-based parallax. Thorstensen (2003) derived a parallax for GP Com of 14.8±1.3 mas, translating into a distance of 68^{+7}_{-6} pc, in good agreement with our determination. For V396 Hya, J. R. Thorstensen (private communication) derives a parallax of 12.9±1.4 mas, translating into a distance of 76^{+11}_{-8} pc, very close to the distance found for GP Com.

A ground-based absolute parallax of 4.25 ± 0.43 mas is derived for AM CVn itself (C. Dahn 2004, as quoted by Nelemans et al. 2004), translating into a distance of 235 pc. This is in disagreement with our measurement at the 5-σ level. The origin of this rather significant discrepancy is not clear.

None of the other AM CVn stars have a ground-based parallax determination sofar. A lower limit to the distance to CR Boo is set by C. Dahn (2004, as quoted by Espaillat et al. 2005) of $d_{\mathrm{CR\,Boo}} > 250$ pc, fully consistent with our measurement.

Parameter	AM CVn	HP Lib	CR Boo	V803 Cen	GP Com
Study Duration (yr)	1.59	1.53	1.62	1.51	2.4
Observation Sets (#)	10	10	9	10	10
Reference stars (#)	3	5	5	5	5
Reference stars $\langle V \rangle$	13.98	13.18	12.09	14.58	14.50
Reference stars $\langle B-V \rangle$	0.84	0.75	0.81	0.67	0.80
HST $\pi_{\rm abs}$ (mas)	1.65±0.30	5.07±0.33	2.97±0.34	2.88±0.24	13.34±0.33
HST relative μ (mas yr^{-1})	34.25±0.88	33.59±1.54	38.80±1.78	9.94±2.98	352.36±12.79
in Position Angle (°)	67.0±1.7	314±14	-79.9 ± 3.7	248±11	-84.7 ± 3.1
d (pc)	606^{+135}_{-93}	197^{+14}_{-12}	337^{+44}_{-35}	347^{+32}_{-27}	75^{+2}_{-2}
LK bias Δd (pc)	$+49 \pm 15$	$+3 \pm 0$	$+14 \pm 2$	$+9 \pm 1$	$+0 \pm 0$
$\langle V \rangle$	14.02±0.05	13.59±0.05	14.5±0.2	14.0±0.2	15.94±0.05
A_V	0.05±0.02	0.34±0.06	0.03±0.04	0.31±0.09	0.02±0.11
$m-M$	$8.91^{+0.36}_{-0.44}$	$6.47^{+0.14}_{-0.15}$	$7.64^{+0.24}_{-0.26}$	$7.70^{+0.17}_{-0.19}$	$4.37^{+0.05}_{-0.05}$
LK bias ΔM	-0.16 ± 0.05	-0.03 ± 0.00	-0.09 ± 0.01	-0.06 ± 0.00	-0.01 ± 0.00
M_V	$4.90^{+0.37}_{-0.45}$	$6.75^{+0.16}_{-0.17}$	$6.74^{+0.32}_{-0.33}$	$5.93^{+0.28}_{-0.29}$	$11.54^{+0.13}_{-0.13}$

Table 5.1: AM CVn Parallaxes, Proper Motions, and Absolute Magnitudes

Model-based distances

A number of accretion disk modelling studies have been done, where the observed optical spectra, in particular the shapes of the spectral lines and the overall slope of the spectrum, are fitted to accretion disk models to derive a number of parameters, including the distance. Estimates include: $d_{\mathrm{ESCet}} = 350$ pc (Espaillat et al., 2005); $d_{\mathrm{CRBoo}} = 469 \pm 50$ pc, $d_{\mathrm{HPLib}} = 188 \pm 50$ pc, $d_{\mathrm{V803Cen}} = 405 \pm 50$ pc, $d_{\mathrm{AMCVn}} = 288 \pm 50$ pc (all from Nasser et al. 2001); and $d_{\mathrm{AMCVn}} = 420 \pm 80$ pc, $d_{\mathrm{CRBoo}} = 206 \pm 15$ pc (El-Khoury & Wickramasinghe, 2000).

Comparing these values with our parallaxes, the large discrepancy with the distance to AM CVn is again striking, whereas the values for CR Boo scatter around our parallax value, and the determination for HP Lib is dead-on target.

Based on our *HST/FGS* parallaxes, it would thus appear that ground-based parallaxes up to at least 75 pc can give quite reliable results, whereas ground-based parallaxes at several hundred pc as well as distances obtained from disk modelling remain uncertain.

5.4.2 Space density of AM CVn stars

Based on an estimated $M_V = 9.5$ for the AM CVn stars in their high states, and the resulting distances $d < 100$ pc for five of the six AM CVn stars known at the time, Warner (1995) derives a local space density $\rho(0) \sim 3 \times 10^{-6}\,\mathrm{pc}^{-3}$ for the systems that are (mostly) in a high state.

Our *HST* parallaxes show that the absolute magnitude in the high states is close to $M_V = 6$, significantly brighter than the value used by Warner (1995). Despite the increase in the number of known AM CVn stars in recent years, mainly due to the Sloan Digital Sky Survey (Anderson et al., 2005; Roelofs et al., 2005), the number of known systems that have high states of $m_V \lesssim 14.5$ is still four. It would thus seem that we can lower the estimates by Warner (1995) that were based on this sample. Employing the "$1/V_{\mathrm{max}}$" method (Schmidt, 1975) with allowance for a completeness of only 10−20% down to $m_V = 14.5$, based on an estimated concentration of systems towards the relatively poorly surveyed Galactic plane, and assuming a population scale height of 300 pc, we arrive at a space density of $\rho(0) \sim 2 \times 10^{-7}\,\mathrm{pc}^{-3}$ for the systems that have high states. This is an order of magnitude lower than Warner's estimate.

If we combine this with the notion that AM CVn stars with orbital periods $P_{\mathrm{orb}} \lesssim 2000$ s are observed to be in a high state at least some of the time, and we compare with evolutionary predictions that only about 2% of the local AM CVn population should currently be at these or shorter orbital periods (Nelemans et al., 2001), we arrive at a local space density

$$\rho(0) \sim 1 \times 10^{-5}\,\mathrm{pc}^{-3} \tag{5.2}$$

for the entire AM CVn population, including the old and dim ones at long orbital periods.

This is an order of magnitude lower than predictions from population synthesis models by Nelemans et al. (2001), which indicate $\rho(0) \sim 1 \times 10^{-4}\,\mathrm{pc}^{-3}$ (there is a small dependency of our 'observed' space density on the population models, because the 2% fraction of systems at

$P_{\rm orb} < 2000$ s was derived from them). It thus appears that space density estimates – both of the bright, short-period ones and of the entire population – have so far been too large by an order of magnitude. The completeness estimates are nevertheless still relatively uncertain, and a more homogeneous sample of AM CVn stars will be needed to bring down those uncertainties (Roelofs et al., in preparation).

5.4.3 Mass accretion rates

From the absolute magnitudes we can estimate the mass accretion rates $\dot{M}$ in our AM CVn stars, assuming that the observed flux is dominated by the accretion luminosity. For this we need to estimate what fraction of the total accretion luminosity of the stars is emitted in the V band; that is, we need the bolometric correction.

To determine this correction, we compose the spectral energy distribution (SED) for all systems except GP Com, based on the optical fluxes, archival *IUE* spectra covering the far- and near-UV, and their 2MASS detections. See Figure 5.1. The most reliable SEDs are those of the non-outbursting systems AM CVn and HP Lib; that of AM CVn has the additional advantage that the extinction towards AM CVn is low, reducing the impact of uncertainties in the extinction correction. We see that the slopes of the UV spectra suggest at least ∼30 kK 'blackbody' components, although both in the infrared and at the far-UV end of the spectra there is a flux excess relative to a 30 kK blackbody, indicating that the systems are not described perfectly by a single-temperature blackbody. At the far-UV end, we could be seeing a contribution from the accreting white dwarf, which is expected to have an effective temperature of ∼40 kK (Bildsten et al., 2006). However, this contribution to the UV flux has to be small since the quiescent magnitudes of V803 Cen and CR Boo indicate that the accretor contributes no more than a few per cent of the light in the optical, while the accretor is not expected to be much hotter than the disk. The donor star is expected to have an effective temperature of only a few thousand Kelvin (C. Deloye, private communication), while it should not be larger than the disk; therefore it should not contribute significantly to the SED either. Thus we are most likely seeing a disk with a range of temperatures.

We first derive a *minimum* bolometric correction (BC) for AM CVn by summing all the *observed* fluxes, without extrapolating beyond the observed wavelengths. This yields a lower limit of $\mathrm{BC} \leq -2.3$. We then have to estimate how much flux is beyond the observed wavelengths. By far the largest part of this flux will be at wavelengths shorter than the observed range. From the slopes of the far-UV spectra, which do not appear to be flattening off that much towards shorter wavelengths, we estimate that they continue as 30–40 kK blackbodies. With this estimated extra flux the total bolometric correction becomes $\mathrm{BC} = -2.8 \pm 0.3$. Given the similarity of the SEDs, we assume this bolometric correction for all systems (although CR Boo's *IUE* spectrum has a rather low flux compared to its average optical flux, we assume that this is due to its outburst behavior).

The exception is GP Com, which is thought to be in a stable state of low mass transfer. Its SED has been shown to match rather well with a $T_{\rm eff} = 11$ kK blackbody, which is expected

to be the accreting white dwarf, plus helium emission lines from an optically thin accretion disk (Bildsten et al., 2006). We have therefore used a bolometric correction appropriate for an 11 ± 1 kK blackbody: $\mathrm{BC}_{\mathrm{GP\,Com}} = -0.5 \pm 0.2$. Since the temperature of the accreting white dwarf we see today is probably set by accretion heating that occurred a long time ago, when GP Com was a much shorter-period binary with much higher $\dot{M}$ (Bildsten et al., 2006), we can only put an upper limit to GP Com's present-day accretion rate.

For a given system with a given BC, we can derive the bolometric luminosity, L, and compare with the value

$$L = \frac{1}{2}\dot{M}_2(\Phi(L_1) - \Phi(R_1)) \tag{5.3}$$

expected for conservative mass transfer through a Keplerian (i.e. virialised) disk, where Φ is the Roche potential, at the inner Lagrange point L_1 and the surface of the accreting star R_1. Since the accreting white dwarf will still be rather hot due to accretion-induced heating (Bildsten et al., 2006), at least for the four bright systems, we apply a first-order correction of 10% to the zero-temperature white dwarf radius, based on the mass–radius relations given by Panei et al. (2000). We can then link the mass transfer rate to the component masses by assuming that gravitational-wave losses drive the evolution of the system, as is commonly assumed (e.g. Deloye et al., 2005; Marsh et al., 2004), and requiring that the secondary fill its Roche lobe. This gives

$$\frac{\dot{M}_2}{M_2} = \frac{\dot{J}}{J}\frac{2}{\zeta_2 + 5/3 - 2q} \tag{5.4}$$

where the angular momentum loss due to the emission of gravitational waves is given by

$$\frac{\dot{J}}{J} = -\frac{32}{5}\frac{G^3}{c^5}\frac{M_1 M_2 (M_1 + M_2)}{a^4} \tag{5.5}$$

(Landau & Lifschitz, 1971), $q \equiv M_2/M_1$ is the mass ratio of the binary, and

$$\zeta_2 \equiv \frac{\mathrm{d}\log R_2}{\mathrm{d}\log M_2}. \tag{5.6}$$

expresses the mass–radius relation of the mass-losing star. This parameter may range from $\zeta_2 \approx -0.06$ for a semi-degenerate helium object based on evolutionary calculations by Tutukov & Fedorova (1989) as parameterized by Nelemans et al. (2001), to $\zeta_2 \approx -1/3$ for an (idealized) zero-temperature white dwarf.

For a given mass ratio q and a choice of mass-radius relation of the secondary ζ_2, the mass of the secondary is now fixed by the observed bolometric luminosity. At present only GP Com (Steeghs et al. in preparation) and AM CVn (Roelofs et al., 2006b) have a directly measured mass ratio. For the other three we can either estimate the primary's mass, or the mass ratio. In Roelofs et al. (2006b) we derive a primary mass $M_1 = 0.68 M_\odot$ for AM CVn, and combined with the mass distribution of single white dwarfs (e.g. Bergeron et al. 1992), it would seem

reasonable to adopt a similar canonical white dwarf mass for the accretors in HP Lib, CR Boo, and V803 Cen.

We do, however, have one additional piece of information on these three systems: they all show 'superhump' periods ($P_{\rm sh}$) in time-series photometry (Patterson et al., 1997, 2000, 2002), which are thought to be due to a tidal resonance between the accretion disk and the secondary star. Observationally and theoretically, it has been found that there exists a (roughly linear) relation between the superhump period excess ϵ, defined as

$$\epsilon \equiv \frac{P_{\rm sh} - P_{\rm orb}}{P_{\rm orb}} \tag{5.7}$$

and the mass ratio q, at least for the hydrogen-rich Cataclysmic Variables (Patterson et al., 2005; Whitehurst, 1988; Whitehurst & King, 1991; Hirose & Osaki, 1990). To date, there is only one AM CVn star for which we have both a kinematically derived mass ratio and a superhump period excess, namely AM CVn itself (Skillman et al., 1999; Roelofs et al., 2006b). We may estimate mass ratios for HP Lib, CR Boo, and V803 Cen by assuming a linear $\epsilon(q)$ relation,

$$\epsilon(q) = 0.12q \tag{5.8}$$

for them, based on $q = 0.18$, $\epsilon = 0.0218$ measured for AM CVn. The resulting mass ratios for HP Lib, CR Boo and V803 Cen are shown in Table 5.2. The first two of these are about twice as large as those used by Deloye et al. (2005), who employ an $\epsilon(q)$ relation that is based on fits to numerical simulations of accretion disks in hydrogen-rich CVs, as given by Warner (1995). Adopting instead the empirical $\epsilon(q)$ for hydrogen-rich CVs from Patterson et al. (2005) already yields larger mass ratios than the ones used in Deloye et al. (2005), but still smaller than ours. Our mass ratio estimate for V803 Cen is also much larger *relative* to the other systems than the one used by Deloye et al. (2005); this is due to a new robust measurement of V803 Cen's orbital period, as discussed in section 5.4.5. Although our $\epsilon(q)$ relation is uncertain since it is based solely on AM CVn, it is probably the best we can do until independent mass ratio measurements become available for more AM CVn stars. We choose to employ this $\epsilon(q)$ relation combined with the known superhump excesses for HP Lib, CR Boo, and V803 Cen to estimate their individual mass ratios, rather than assume a canonical primary mass for all three.

Lastly, a correction has to be made for the inclination i of the binary, since the 'apparent absolute magnitude' (Warner, 1995) depends on the inclination. For HP Lib and V803 Cen the inclination is constrained by spectroscopic measurements of the velocity amplitude of the 'bright spot' (that is, the accretion stream–accretion disk impact region) in these systems (Roelofs et al. 2006d; see also section 5.4.5). We make the assumption that the radial velocity semi-amplitude of the donor star is equal to that of the bright spot, which is usually a good estimate. Similar data does not exist for CR Boo and we thus adopt the value of $i = 30°$ derived from spectral line modelling by Nasser et al. (2001), with the sidenote that their model-derived inclinations for AM CVn, HP Lib, and V803 Cen are in excellent agreement with the kinematically derived values. Table 5.2 lists the inclinations we employ for all systems.

With the above assumptions we have all the ingredients needed to solve for the masses and mass transfer rates of our AM CVn stars: for a given mass ratio q, there is only one set of M_1 and M_2 for which the resulting accretion luminosity due to gravitational-wave losses matches with the observed luminosity. For AM CVn, which has a kinematically measured mass ratio, the dominant contributions to the error on the mass transfer rate are the error on its absolute magnitude M_V and the uncertainty in the bolometric correction. For HP Lib, CR Boo, and V803 Cen, we consider the uncertainty on their true mass ratios to be the most important factor. The errors on the mass transfer rates for these systems are estimated by varying q by $\pm 50\%$ from the 'best estimates' given in Table 5.2. The resulting lower limits then correspond to the low mass ratios employed by Deloye et al. (2005), while the resulting upper limits correspond to qs that are such that $q_{\rm HP\,Lib}$ coincides with our kinematically measured $q_{\rm AM\,CVn}$, which one might expect if they share a similar evolutionary history, given their similar orbital period. Note that these ranges in q give ranges of M_2 and M_1 (see Table 5.2) that are anti-correlated.

We can compare our values to those obtained by Nasser et al. (2001) using spectral modelling of the accretion disks of these systems. With our larger distance for AM CVn, the accretion rate based on their models should be a bit larger than our value, at $\dot{M}_{\rm AM\,CVn} \sim 1 \times 10^{-8}\,M_\odot$/yr (J.-E. Solheim, private communication). For the other systems they find $\dot{M} \sim 4 \times 10^{-9}\,M_\odot$/yr, which is again larger than our values of $\dot{M} \sim 1 \times 10^{-9}\,M_\odot$/yr. El-Khoury & Wickramasinghe (2000) on the other hand find $\dot{M}_{\rm AM\,CVn} \sim 2 \times 10^{-9}\,M_\odot$/yr, also from spectral modelling of the accretion disk, which is lower than our value. Their value of $\dot{M}_{\rm CR\,Boo} \sim 1 \times 10^{-9}\,M_\odot$/yr is close to ours.

Parameter	AM CVn	HP Lib	CR Boo	V803 Cen	GP Com
$P_{\rm orb}$ (s)	1029	1103	1471	1596	2794
q	0.18[a]	0.12[b]	0.09[b]	0.11[b]	0.02[a]
i (degrees)	43 ± 3	$27 - 35$	30[c]	$14 - 19$	n/a
BC	-2.8 ± 0.3	-2.8 ± 0.3	-2.8 ± 0.3	-2.8 ± 0.3	-0.5 ± 0.2
L (W)	$4.3^{+2.8}_{-1.5} \times 10^{27}$	$7.8^{+2.9}_{-2.1} \times 10^{26}$	$7.8^{+4.0}_{-2.6} \times 10^{26}$	$1.7^{+0.8}_{-0.5} \times 10^{27}$	$1.1^{+0.3}_{-0.2} \times 10^{24}$
$\dot{M}$ ($M_\odot$ yr^{-1})	$6.7^{+1.9}_{-1.3} \times 10^{-9}$	$[0.63-1.8] \times 10^{-9}$	$[3.5-9.3] \times 10^{-10}$	$[0.50-1.4] \times 10^{-9}$	$<4.3 \pm 0.5 \times 10^{-12}$
M_2 ($M_\odot$)	0.125 ± 0.012	$0.044 - 0.082$	$0.044 - 0.081$	$0.057 - 0.106$	$< 0.013 \pm 0.001$
M_1 ($M_\odot$)	0.68 ± 0.06	$0.72 - 0.45$	$0.98 - 0.60$	$1.04 - 0.64$	$< 0.62 \pm 0.05$

Table 5.2: Bolometric Luminosities and Mass Accretion Rates. [a]Measured kinematically. [b]Inferred from superhump period; note the difference with Table 1 of Deloye et al. (2005). [c]From Nasser et al. (2001).

5.4.4 The nature of the donor stars

The most surprising result of our *HST* parallaxes is the large distance to AM CVn, which exceeds every previous estimate. The resulting large luminosity of AM CVn already suggests a relatively high mass accretion rate. In addition to the large distance found here, AM CVn's recently measured mass ratio, too, was found to be significantly larger than previously thought (Roelofs et al., 2006b). With these two pieces of information we could solve self-consistently for the masses of the components (within the assumptions outlined in Section 5.4.3), and provide strong evidence that the donor star in AM CVn is a relatively massive, only partially degenerate helium object.

For HP Lib, CR Boo, and V803 Cen, there is a larger uncertainty in the masses of the components due to the larger uncertainties on their mass ratios, as discussed in the previous section. Nevertheless, if we compare the data with evolutionary predictions for fully-degenerate and semi-degenerate donors (see Figure 5.2), the data are seen to favor rather massive, semi-degenerate donor stars in all systems but GP Com (although in HP Lib the donor is not quite as massive as in the other three bright systems). This agrees qualitatively with the accretion disk models of Nasser et al. (2001), but disagrees with El-Khoury & Wickramasinghe (2000) who find a fully-degenerate donor in AM CVn.

It should be noted that there is a selection effect against fully-degenerate donor stars, since AM CVn stars with semi-degenerate donors are expected to be brighter at short orbital periods due to the higher mass accretion rates. At long orbital periods this is partially offset by the fact that semi-degenerate systems evolve to lower accretion rates more quickly. If we evolve a fully degenerate and a semi-degenerate system, based on the parameterization of Nelemans et al. (2001), we see that semi-degenerate donors are in a bright state about twice as long, where we take 'bright state' to be $\dot{M}_2 \sim 10^{-8} - 10^{-10}\,M_\odot$/yr, i.e. a state corresponding to the four bright AM CVns under consideration here. See Figure 5.3.

We thus observe four relatively massive, semi-degenerate systems out of five, with a potential factor of two selection effect towards the semi-degenerates. We can conclude that at least a significant fraction, and possibly all, of the short-period systems (at $P_{\rm orb} \lesssim 2000$ s) have hot, semi-degenerate donors rather than cold, degenerate ones. AM CVn stars with such hot, semi-degenerate donors are expected naturally from the helium star channel (Nelemans et al., 2001), but a fraction of AM CVn progenitors in the WD channel are also expected to still have hot donors upon coming into contact (Deloye et al., 2005). Conceivably, it could be this hot fraction of systems that survive as AM CVn stars in the WD channel, since the mass transfer rate upon Roche-lobe overflow can be up to two orders of magnitude lower than for cold, degenerate donors (Nelemans et al., 2001; Deloye et al., 2005). Another possibility would be that cold white dwarf donors in the WD channel are reheated by tidal heating close to orbital period minimum (e.g. Iben et al. 1998). Interpretation of our results in terms of the evolutionary history of the systems requires a more detailed study of these effects. Of particular interest would be a comparison between HP Lib and AM CVn, whose donor stars appear to have a different level of degeneracy despite their otherwise identical appearance (Roelofs et al.,

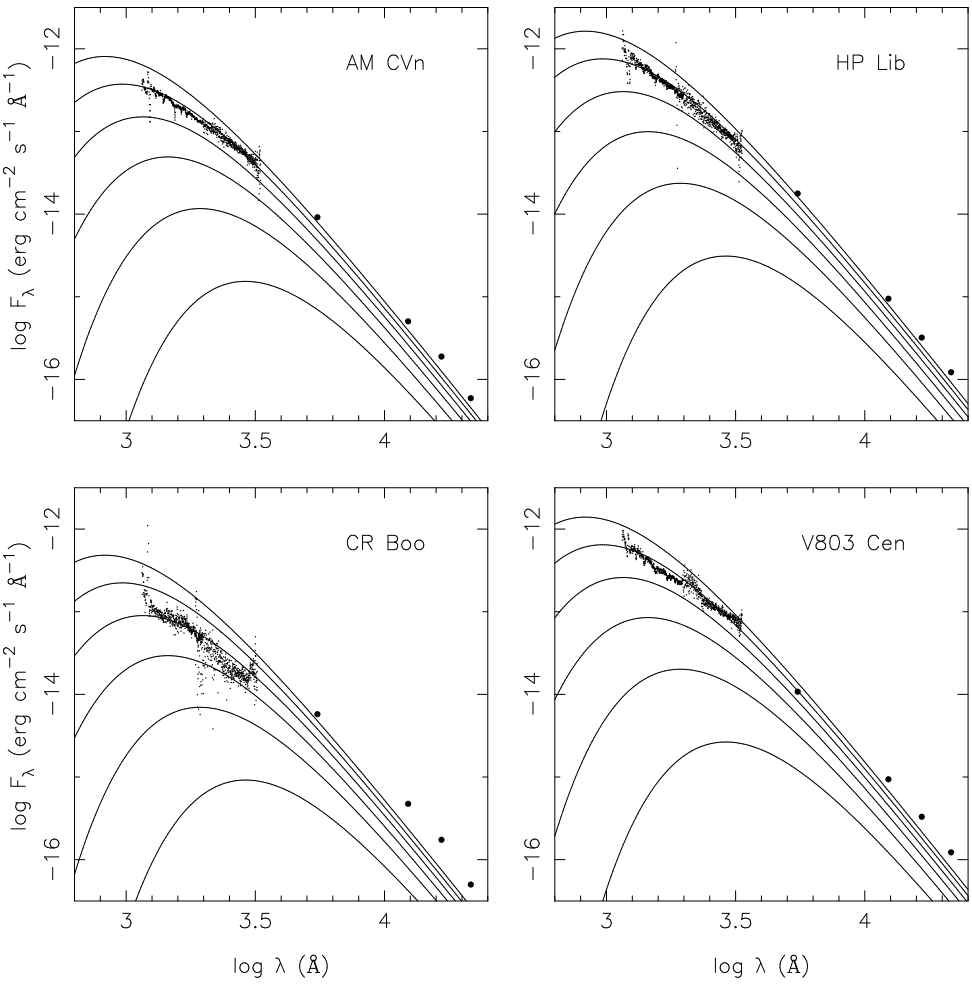

FIGURE 5.1: Observed spectral energy distributions of AM CVn, HP Lib, CR Boo, and V803 Cen, compiled from archival *IUE* spectra, 2MASS data, and the observed optical fluxes. The solid lines are blackbody spectra of $T_{\rm eff} = 10-35$ kK in steps of 5 kK (bottom to top) to get an idea of the temperatures. For CR Boo and V803 Cen, we selected the apparent high-state spectra from the *IUE* archives; however, we cannot exclude that they represent slightly lower intermediate states. For CR Boo this was definately the case for its short-wavelength (1150–2000 Å) spectrum; we scaled it up to match the overlapping long-wavelength (1850–3350 Å) *IUE* spectrum. Its UV flux still seems low with respect to the average optical flux and the 2MASS snapshots. The data have been corrected for extinction according to Cardelli et al. (1989) and assuming an $R_V = 3.1$ extinction law.

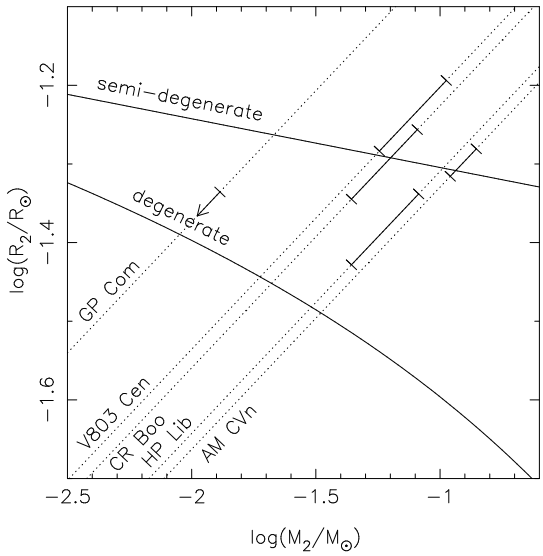

FIGURE 5.2: Constraints on the masses and radii of the donor stars, compared to degenerate and semi-degenerate evolutionary tracks from Nelemans et al. (2001). The dotted diagonals represent the Roche-lobe filling solutions for the different systems. The solid-line region for AM CVn respresents the 1-σ confidence level; for GP Com it represents the 1-σ upper limit on its donor mass. For the remaining three systems the solid line is the range obtained by varying the (indirectly measured) mass ratio by 50%. We see that, apart from GP Com, the donors appear to be rather semi-degenerate.

2006b,d). A kinematic measurement of HP Lib's mass ratio would be needed to determine whether its donor star has a truely different nature.

5.4.5 The mass ratio of V803 Cen

The small mass ratio of V803 Cen, $q_{\rm V803\,Cen} = 0.016$, implied by the small superhump period excess as obtained from Patterson (2001) by Deloye et al. (2005) and others, leads to a necessarily large accretor mass close to the Chandrasekhar limit, and a small donor mass close to the minimum mass for a Roche-lobe filling secondary (corresponding to a cold, fully degenerate object). This was already noted by Deloye et al. (2005). Given these important implications, it should be mentioned that V803 Cen is the one system for which the photometric superhump period excess appeared to be uncertain. The superhump period around 1618 seconds is confirmed beyond doubt in an extensive observational effort by Patterson et al. (2000), but the identification of 1611-second variations (see references in Patterson et al. 2000) with the orbital period is rather uncertain. An orbital period of 1611 seconds has nevertheless entered the literature (Patterson 2001, Patterson et al. 2002, Woudt & Warner 2003, Deloye et al. 2005).

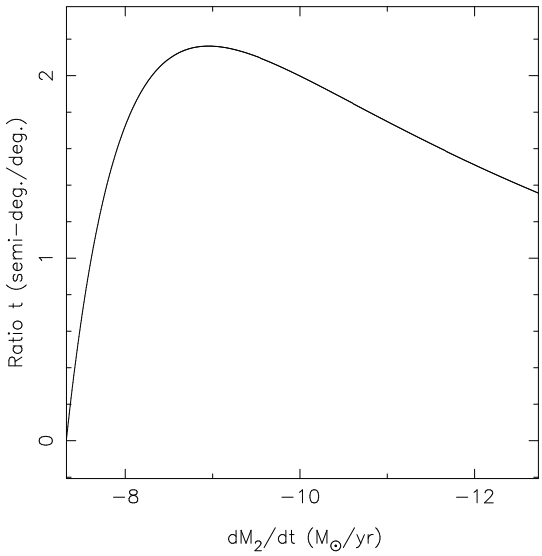

FIGURE 5.3: Ratio of the integrated times spent at a given mass transfer rate *or higher*, for a $0.6\,M_{\odot}$ white dwarf accreting from a fully degenerate ($0.25\,M_{\odot}$) and a semi-degenerate ($0.2\,M_{\odot}$) donor star as modeled by Nelemans et al. (2001). Semi-degenerate systems are seen to spend about twice as long at phases of relatively high mass transfer, $10^{-10} \lesssim \dot{M}_2 \lesssim 10^{-8}\,M_{\odot}$/yr, corresponding to the mass transfer rates found for AM CVn, HP Lib, CR Boo and V803 Cen.

Because of this uncertainty in the superhump period excess of V803 Cen, and the resulting stringent constraints on the masses of its components, we obtained time-series spectroscopy with the VLT and found a significantly shorter orbital period: $P_{\rm V803\,Cen} = 1596.4 \pm 1.6$ seconds (Roelofs et al., 2006d). The mass ratio we use in this paper is the one we obtain from the corresponding (larger) superhump period excess, again with a $\pm 50\%$ range.

Instead of a degenerate star donating matter to a massive accretor very close to the Chandrasekhar limit, the new $q_{\rm V803\,Cen} = 0.05 - 0.17$ yields a much more mundane accretor mass and a hot, semi-degenerate donor star, quite like AM CVn, CR Boo, and (to a lesser extent) HP Lib (cf. Deloye et al. 2005).

5.4.6 AM CVn stars as sources of gravitational waves

The ultra-compact nature of the AM CVn stars, combined with the relative proximity of the known systems, makes them the strongest known sources of gravitational waves in the frequency regime covered by space-borne gravitational-wave detectors such as *LISA*.

The masses of the secondary stars, inferred from the luminosities, can be used to estimate

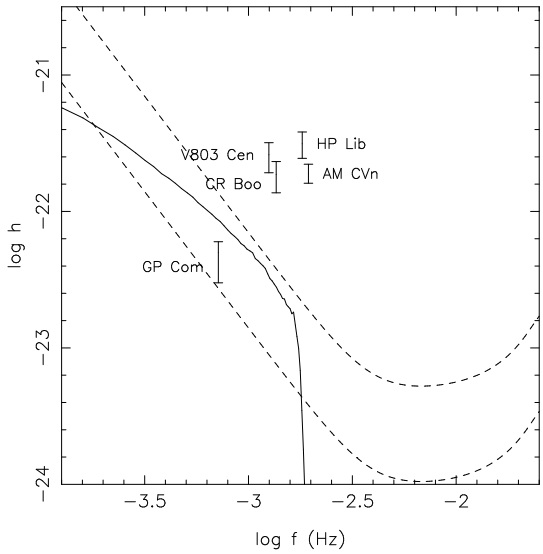

FIGURE 5.4: Predicted gravitational-wave strain amplitudes h and frequencies f of the five AM CVn stars for which we obtained an *HST* parallax. The upper and lower dashed lines show the design sensitivities of *LISA* for a signal-to-noise ratio of 5 and 1, respectively, in one year of data-collecting (Larson et al., 2000). The solid line is a population synthesis prediction for the confusion-limited Galactic background (Nelemans et al., 2004).

the gravitational-wave strain amplitudes of our five AM CVns. The gravitational-wave strain amplitude h is given by (see Roelofs et al. 2006b, after Timpano et al. 2006)

$$h = 2.84 \cdot 10^{-22} \sqrt{\cos^4 i + 6\cos^2 i + 1} \times \left(\frac{\mathscr{M}}{M_\odot}\right)^{5/3} \left(\frac{P_{\rm orb}}{1\,{\rm hr}}\right)^{-2/3} \left(\frac{d}{1\,{\rm kpc}}\right)^{-1} \quad (5.9)$$

where $\mathscr{M} = (M_1 M_2)^{3/5}/(M_1 + M_2)^{1/5}$ is the so-called chirp mass, and d the distance to the star. Figure 5.4 shows the resulting strain amplitudes of our five systems. These values are quite insensitive to the uncertain mass ratios q of some of our systems; their errors are dominated by the errors on the bolometric luminosities of the systems. We see that the four short-period systems are all excellent test sources for *LISA*, standing out significantly above both the instrument's design sensitivity and the expected average Galactic background signal (although a more rigorous analysis may be needed to predict their exact signal-to-noise ratios; see Stroeer & Vecchio 2006). The estimates for the four bright systems have gone up from initial estimates by Nelemans (2005) due to their rather massive donors, and their relatively low inclinations. The expectations for GP Com remain rather low: it does not stand out from the instrumental and

Galactic noise and will be much more difficult to identify. We note that the chances of confusion with Galactic noise sources decrease greatly with more accurately known orbital periods for these systems, as long as the error on the orbital frequency is larger than the frequency resolving power of *LISA* ($\Delta f \sim t_{\rm obs}^{-1} \sim 10^{-8}$ Hz, for a mission duration $t_{\rm obs} = 1$ yr). The orbital period of AM CVn is known to better than one part-per-million accuracy from large time-base photometric monitoring ($P_{\rm AMCVn} = 1028.7322 \pm 0.0003$ s, Skillman et al. 1999), and the orbital period of HP Lib also seems quite secure ($P_{\rm HP\,Lib} = 1102.70 \pm 0.05$ s, Patterson et al. 2002), but the orbital periods of especially V803 Cen and CR Boo seem to be less well-known. It would be worthwhile to measure the orbital periods of these systems with greater accuracy.

5.5 AM CVn and reference star data tables

Set	MJD	Roll (°)[1]	V^2
AM CVn-1	52222.81198	217	14.02±0.01
AM CVn-2	52225.88485	58	14.01±0.01
AM CVn-3	52387.43705	217	14.04±0.02
AM CVn-4	52390.64253	33	14.03±0.01
AM CVn-5	52431.24828	33	14.03±0.01
AM CVn-6	52435.52559	58	13.99±0.01
AM CVn-7	52715.78999	58	14.01±0.01
AM CVn-8	52719.72357	359	14.04±0.02
AM CVn-9	52796.35781	359	14.04±0.02
AM CVn-10	52803.28106	58	14.03±0.02
CR Boo-1	52095.17132	82	14.51±0.03
CR Boo-2	52103.46567	82	14.16±0.01
CR Boo-3	52136.09742	83	14.36±0.01
CR Boo-4	...	...	...
CR Boo-5	52309.56485	273	13.93±0.03
CR Boo-6	52322.84773	273	15.99±0.04
CR Boo-7	52501.29821	83	15.88±0.04
CR Boo-8	52512.98296	87	15.96±0.02
CR Boo-9	52676.15807	273	15.61±0.04
CR Boo-10	52686.69897	273	15.07±0.01
V803 Cen-1	52112.02035	68	14.19±0.03
V803 Cen-2	52115.43291	68	13.50±0.05
V803 Cen-3	52161.84252	37	13.64±0.01
V803 Cen-4	52164.04853	37	15.68±0.08
V803 Cen-5	52294.81707	247	13.46±0.01
V803 Cen-6	52300.82760	247	13.51±0.01
V803 Cen-7	52526.14146	37	14.64±0.03
V803 Cen-8	52530.14615	37	13.85±0.04
V803 Cen-9	52659.74478	246	14.34±0.02
V803 Cen-10	52664.41432	246	13.69±0.04
HP Lib-1	52135.63781	74	13.61±0.03
HP Lib-2	52138.24565	74	13.62±0.01
HP Lib-3	52168.26915	80	13.59±0.02
HP Lib-4	52172.41573	80	13.59±0.02
HP Lib-5	52318.71790	256	13.60±0.02
HP Lib-6	52326.79246	256	13.60±0.02
HP Lib-7	52532.15146	80	13.57±0.02
HP Lib-8	52539.16093	80	13.58±0.02
HP Lib-9	52680.90353	256	13.56±0.02
HP Lib-10	52693.71125	256	13.54±0.02
GP Com-1	52088.34598	65	15.96±0.01
GP Com-2	52097.16817	65	15.99±0.01
GP Com-3	52234.70052	229	15.89±0.02
GP Com-4	52242.04902	229	15.92±0.01
GP Com-5	52270.97565	245	15.93±0.01
GP Com-6	52273.91306	245	15.94±0.02
GP Com-7	52598.75738	229	15.93±0.02
GP Com-8	52633.85590	244	16.01±0.02
GP Com-9	52637.92521	244	16.00±0.02
GP Com-10	52963.80643	229	15.89±0.01

TABLE 5.3: Log of Observations and FGS Photometry

ID	ξ[3]	η
AM CVn[4]		
ref-2	−77.5390 0.0003	−137.4972 0.0002
ref-3	159.3017 0.0003	−173.8572 0.0002
ref-5	60.260 0.0003	−88.9279 0.0002
CR Boo[5]		
ref-2	−192.2319 0.0003	−49.5013 0.0002
ref-3	−242.6593 0.0002	−3.4712 0.0001
ref-4	304.3653 0.0003	-16.0044 0.0002
ref-5	250.2984 0.0006	19.8065 0.0004
ref-6	437.8449 0.0009	9.7262 0.0006
V803 Cen[6]		
ref-2	78.2233 0.0003	42.8896 0.0002
ref-3	−119.9175 0.0003	−26.1711 0.0002
ref-4	−55.0075 0.0002	110.9745 0.0002
ref-5	−122.0958 0.0002	67.3278 0.0002
ref-6	137.4346 0.0002	39.0072 0.0002
HP Lib[7]		
ref-2	89.3402 0.0003	−66.1514 0.0002
ref-3	249.1257 0.0003	−18.3677 0.0002
ref-4	9.8453 0.0004	77.8612 0.0003
ref-5	−4.4333 0.0003	55.4678 0.0002
ref-6	−311.6452 0.0003	−13.1930 0.0002
GP Com[8]		
ref-2	81.0209 0.0002	33.9032 0.0001
ref-3	88.3580 0.0002	95.1984 0.0001
ref-4	80.9519 0.0002	−73.6567 0.0001
ref-5	105.5746 0.0003	30.4648 0.0002
ref-6	−103.6979 0.0002	101.5386 0.0002

TABLE 5.4: Reference Star Positions

ID	Spectral Type	V	M_V	A_V	$m-M$	$\pi_{\rm abs}$(mas)
AM CVn						
ref-2	G4V	14.37	5.0	0.05	9.4±0.7	1.3±0.4
ref-3	K6V	15.15	7.6	0.05	7.5 0.7	3.2 1.0
ref-5	G4V	12.42	5.0	0.05	7.5 0.7	3.3 1.0
CR Boo						
ref-2	G9V	15.57	5.74	0.02	9.8 0.7	1.1 0.4
ref-3	M2III	11.40	−0.6	0.02	12.0 0.7	0.4 0.1
ref-4[9]	F2V	6.81	3.0	0.02	3.8 0.7	16.9 0.9
ref-5	G0V	14.82	4.4	0.02	10.4 0.7	0.8 0.3
ref-6	G7V	11.93	5.4	0.02	6.5 0.7	5.1 1.6
V803 Cen						
ref-2	K1V	15.86	6.2	0.31	9.7 0.7	1.3 0.4
ref-3	G4V	15.34	5.0	0.31	10.4 0.7	0.9 0.3
ref-4	F6.5V	13.38	3.8	0.31	9.6 0.7	1.4 0.4
ref-5	G6V	14.17	5.3	0.31	8.9 0.7	1.9 0.6
ref-6	F8V	14.15	4.0	0.31	10.2 0.7	1.1 0.4
HP Lib						
ref-2	F5V	12.86	3.5	0.34	9.4 0.7	1.6 0.5
ref-3	G9V	14.06	5.7	0.34	8.4 0.7	2.6 0.8
ref-4	K7V	12.57	7.9	0.34	4.7 0.7	14.0 4.5
ref-5	K4V	11.80	7.1	0.34	4.7 0.7	13.6 4.4
ref-6	A2.5V	14.60	1.3	0.34	13.3 1.0	0.3 0.1
GP Com						
ref-2	G0V	15.17	4.4	0.02	10.8 0.7	0.7 0.2
ref-3	G8V	14.39	5.58	0.02	8.8 0.7	1.7 0.6
ref-4	K0V	14.25	5.58	0.02	8.7 0.7	1.8 0.6
ref-5	K5V	13.56	7.4	0.02	6.2 0.7	5.7 1.9
ref-6	G8V	15.12	5.58	0.02	9.5 0.7	1.2 0.4

TABLE 5.5: Reference Star Spectrophotometric Parallaxes

ID	V	K	$J-H$	$J-K$	$V-K$
AM CVn					
ref-2	14.37 0.1	12.79 0.03	0.44 0.04	0.43 0.03	1.58 0.10
ref-3	15.15 0.1	12.09 0.02	0.74 0.04	0.82 0.03	3.06 0.10
ref-5	12.42 0.1	10.88 0.02	0.41 0.04	0.42 0.03	1.54 0.10
CR Boo					
ref-2	15.57 0.1	13.64 0.05	0.47 0.05	0.48 0.05	1.93 0.11
ref-3	11.4 0.1	7.13 0.05	0.91 0.02	1.13 0.05	4.28 0.11
ref-4	14.8 0.1	5.93 0.01	0.21 0.04	0.22 0.02	0.87 0.05
ref-5	6.8 0.1	13.54 0.05	0.34 0.05	0.27 0.06	1.46 0.11
ref-6	11.89 0.1	...	...	...	...
V803 Cen					
ref-2	15.86 0.1	13.42 0.04	0.53 0.04	0.62 0.04	2.44 0.11
ref-3	15.34 0.1	13.58 0.04	0.45 0.04	0.43 0.05	1.76 0.11
ref-4	13.38 0.1	11.96 0.02	0.29 0.03	0.33 0.03	1.42 0.10
ref-5	14.17 0.1	12.29 0.02	0.42 0.03	0.51 0.03	1.88 0.10
ref-6	14.15 0.1	12.45 0.03	0.35 0.03	0.36 0.04	1.70 0.10
HP Lib					
ref-2	12.88 0.1	11.40 0.02	0.30 0.03	0.34 0.03	1.48 0.10
ref-3	14.11 0.1	11.93 0.02	0.51 0.03	0.51 0.03	2.18 0.10
ref-4	12.6 0.1	9.17 0.02	0.69 0.03	0.84 0.03	3.43 0.10
ref-5	11.84 0.1	8.87 0.02	0.66 0.03	0.77 0.03	2.97 0.10
ref-6	14.6 0.1	...	...	...	...
GP Com					
ref-2	15.17 0.1	13.73 0.05	0.34 0.04	0.36 0.06	1.44 0.11
ref-3	14.39 0.1	12.62 0.03	0.43 0.03	0.46 0.03	1.77 0.10
ref-4	14.25 0.1	12.24 0.03	0.46 0.03	0.54 0.03	2.01 0.10
ref-5	13.56 0.1	10.71 0.02	0.67 0.02	0.74 0.03	2.85 0.10
ref-6	15.12 0.1	13.44 0.04	0.40 0.04	0.53 0.05	1.68 0.11

TABLE 5.6: FGS and Near-IR Reference Star Photometry

ID	Spectral Type	$(V-K)_0$	$V-K$	$E(V-K)$	A_V[10]	$\langle A_V \rangle$
AM CVn						0.05±0.02
ref-2	G4V	1.52	1.58	0.06	0.07	
ref-3	K6V	3.01	3.06	0.05	0.06	
ref-5	G4V	1.52	1.54	0.02	0.02	
CR Boo						0.03±0.04
ref-2	G9V	1.88	1.93	0.05	0.05	
ref-3	M2III	4.30	4.28	−0.02	−0.02	
ref-4	F2V	0.86	0.87	0.01	0.01	
ref-5	G0V	1.41	1.46	0.05	0.06	
V803 Cen						0.31±0.09
ref-2	K1V	2.14	2.44	0.30	0.33	
ref-3	G4V	1.52	1.76	0.24	0.26	
ref-4	F6.5V	1.19	1.42	0.23	0.26	
ref-5	G6V	1.67	1.88	0.21	0.23	
ref-6	F8V	1.28	1.70	0.42	0.46	
HP Lib						0.34±0.06
ref-2	F5V	1.10	1.48	0.38	0.42	
ref-3	G9V	1.88	2.18	0.3	0.33	
ref-4	K7V	3.17	3.43	0.26	0.29	
ref-5	K4V	2.68	2.97	0.29	0.32	
GP Com						0.02±0.11
ref-2	G0V	1.41	1.44	0.03	0.03	
ref-3	G8V	1.80	1.77	−0.03	−0.03	
ref-4	K0V	1.96	2.01	0.05	0.05	
ref-5	K5V	2.70	2.85	0.15	0.16	
ref-6	G8V	1.80	1.68	−0.12	−0.14	

TABLE 5.7: Field A_V from Reference Star Spectrophotometry

Chapter 6

On the orbital periods of the AM CVn stars HP Librae and V803 Centauri

G. H. A. Roelofs, P. J. Groot, G. Nelemans, T. R. Marsh and D. Steeghs

Submitted to MNRAS

Abstract. We analyse high-time-resolution spectroscopy of the AM CVn stars HP Librae and V803 Centauri, taken with the New Technology Telescope (NTT) and the Very Large Telescope (VLT) of the European Southern Observatory, Chile.

We present evidence that the literature value for V803 Cen's orbital period is incorrect, based on an observed 'S-wave' in the binary's spectrogram. We measure a spectroscopic period $P_{\mathrm{V803\,Cen}} = 1596.4 \pm 1.2\,\mathrm{s}$ of the S-wave feature, which is significantly shorter than the 1611-second periods found in previous photometric studies. We conclude that the latter period likely represents a 'superhump'. If one assumes that our S-wave period is the orbital period, V803 Cen's mass ratio can be expected to be much less extreme than previously thought, at $q \sim 0.07$ rather than $q \sim 0.016$. This relaxes the constraints on the masses of the components considerably: the donor star does then not need to be fully degenerate, and the mass of the accreting white dwarf no longer has to be very close to the Chandrasekhar limit.

For HP Lib, we similarly measure a spectroscopic period $P_{\mathrm{HP\,Lib}} = 1102.8 \pm 0.2\,\mathrm{s}$. This supports the identification of HP Lib's photometric periods found in the literature, and the constraints upon the masses derived from them.

6.1 Introduction

V803 Centauri and HP Librae are both members of the class of AM CVn stars: ultra-compact binaries with orbital periods below about one hour, in which a white dwarf accretes helium-rich matter from a degenerate or semi-degenerate companion. They are of interest for binary evolution theory, being a distinct class of evolutionary end-products that have probably undergone a common-envelope phase twice. Their ultra-short orbital periods make them important sources for gravitational-wave astronomy; they are the strongest (and so far only) known sources for future detectors such as the *Laser Interferometer Space Antenna (LISA)* (e.g. Nelemans et al. 2004; Roelofs et al. 2006b).

However, determining their orbital periods is made difficult by the superhump phenomenon, by which the observed photometric periods do not match with their orbital periods, which is thought to be due to tidal interactions between the accretion disc and the donor star (Whitehurst, 1988). Because of this complication, several of the short-period AM CVn stars do not have a secure orbital period measurement. AM CVn itself, which has a number of photometric periods dominated by one at 1051 seconds, has been shown from spectroscopy to have an underlying 1029-second orbital period (Nelemans et al., 2001). This is based on an observed 'S-wave' feature that is commonly thought to be associated with the region of impact of the accretion stream into the accretion disc in interacting binaries. Similar behaviour may be expected for HP Lib, a system virtually identical to AM CVn in appearance, and for V803 Cen, which appears similar to AM CVn and HP Lib most of the time but shows occasional drops in brightness of up to five magnitudes, presumably caused by a thermal instability in its accretion disc (Tsugawa & Osaki, 1997).

V803 Cen was discovered as a strongly variable and very blue source by Elvius (1975), in a photometric survey of the region around the galaxy NGC 5128. O'Donoghue et al. (1987) obtained high-speed photometry which showed the source to be a rapid variable, exhibiting variations on a ∼1611-second period. They noted the similarities with another recently discovered rapid variable, CR Boo, and classified it as an interacting binary white dwarf; the 1611-second period was recovered several times in follow-up photometry (O'Donoghue & Kilkenny, 1989; O'Donoghue et al., 1990). An extensive monitoring campaign by Patterson et al. (2000) uncovered a 1618-second signal whenever V803 Cen was in a state of high brightness, while recovering the 1611-second variations in low and intermediate brightness states. Although Patterson et al. (2000) initially interpreted these results in terms of a slowly dying superhump that persists into the low state, the suggestion that 1611 s is in fact the orbital period appeared shortly thereafter (Patterson, 2001). This allowed for an estimate of the mass ratio $q = M_2/M_1$ of the binary based on the observed relation between the superhump period excess, $\epsilon \equiv (P_{\rm sh} - P_{\rm orb})/P_{\rm orb}$, and the mass ratio in Cataclysmic Variables (e.g. Patterson et al. 2005).

V803 Cen's tiny superhump period excess then implies an extremely small mass ratio $q \approx 0.016$. As noted by Deloye et al. (2005), the minimum mass for the donor star, which corresponds to the mass of a cold, fully degenerate white dwarf that fills its Roche lobe in V803 Cen's orbit, implies that the accretor must be massive: $M_{1,\rm V803\,Cen} \gtrsim 1.3\,M_\odot$. Conversely, the Chandrasekhar

limit to the mass of the accretor then indicates that the donor in V803 Cen has to be nearly fully degenerate, which would suggest that V803 Cen was formed from a double-degenerate rather than from a single-degenerate binary (see Nelemans et al. 2001).

In order to explain the large observed luminosity of V803 Cen (Roelofs et al., 2006c), while requiring that the donor star be fully degenerate, one would require an accretor mass even closer to the Chandrasekhar limit in order to extract a sufficient amount of energy per unit mass of accreted material: $M_{1,\mathrm{V803\,Cen}} \approx 1.43 M_{\odot}$, if one assumes the mass transfer rate to be set by the system's gravitational-wave losses. Given these spectacular implications, a more secure identification of the orbital period of the binary is desirable. In this paper we search for a spectroscopic signal of V803 Cen's orbital period in observations made with the Very Large Telescope (VLT), Chile.

The second object discussed in this paper, HP Lib, was discovered more recently in the Edinburgh-Cape survey for blue objects and recognised immediately as a twin of the prototype star AM CVn. It exhibits 1119-second brightness variations, but no large outbursts like the ones observed in V803 Cen and CR Boo (O'Donoghue et al., 1994).

Patterson et al. (2002) again conducted an extensive campaign of time-series photometry and discovered, in addition to the main 1119-second variations, an extremely low-amplitude modulation on 1102.70 ± 0.05 seconds. This was readily interpreted as the likely orbital period of the binary, while the resulting constraints on the masses of the components, inferred from the (larger) superhump period excess (Deloye et al., 2005), are not nearly as stringent as those derived for V803 Cen. We here analyse fast spectroscopy taken with the New Technology Telescope (NTT) in order to, again, search for a spectroscopic signal of the orbital period of the binary.

6.2 Observations and data reduction

We obtained phase-resolved spectroscopy of V803 Cen on 1 and 2 March 2005 with the Very Large Telescope (VLT) and the FOcal Reducer/low dispersion Spectrograph (FORS2). The observations consist of 50 spectra taken with the 1400V grism, covering 4625–5930 Å, followed by 250 spectra with the 1200R grism, covering 5870–7360 Å, all with a 30-second exposure time. Weather conditions were good, with a median seeing around $0.6''$, giving an effective resolution of about 1.8 Å or 80 km/s at 6678 Å.

All spectra were taken with a $1''$ slit. The detector was the standard MIT mosaic consisting of two CCDs of 2k×4k, 15μm pixels, binned by a factor of two. The dispersion solution was obtained from a set of 42 night sky lines for the 1200R grism, and from standard HeNeAr arc exposures for the 1400V grism, resulting in $\sim$0.1 Å root-mean-square residuals. In order to take full advantage of the good seeing, we corrected the 1200R spectra for the possible drifting of the star within the slit and the consequent drift in the dispersion solution (to zeroth order) using the sharp atmospheric absorption edge at 6868 Å. All spectra were transformed to the

Night	UT	Set-up	Exposures	Exp. time (s)	Typical seeing (")
V803 Cen					
2005/03/01	05:20–06:15	VLT+FORS2/1400V	50	30	0.6
	07:35–08:30	VLT+FORS2/1200R	50	30	0.6
2005/03/02	05:43–09:43	VLT+FORS2/1200R	200	30	0.6
2004/03/09	02:00–04:20	NTT+EMMI/#6	10	750	0.7
2004/03/10	02:14–02:44	NTT+EMMI/#6	2	900	0.7
HP Lib					
2004/03/06	05:09–10:04	NTT+EMMI/#6	194	55	1.0
2004/03/07	04:46–10:03	NTT+EMMI/#6	191	55	0.9
2004/03/08	04:50–10:02	NTT+EMMI/#6	223	45–55	0.7
2004/03/09	04:55–10:00	NTT+EMMI/#6	225	45	0.7
2004/03/10	04:49–10:05	NTT+EMMI/#6	237	45–50	0.7

TABLE 6.1: Summary of our observations of V803 Cen and HP Lib. The set-up indicates the telescope, the instrument and the grism or grating.

heliocentric rest-frame prior to analysis. The average spectrum was corrected for instrumental response using spectrophotometric standard star EG274.

In addition to the phase-resolved spectra, we obtained spectra of long exposures with the New Technology Telescope (NTT) and the ESO Multi-Mode Instrument (EMMI) on 9 and 10 March 2004. We used grating #6 and a $1''$ slit to obtain an effective resolution of 0.7 Å FWHM over the range 4330–5050 Å. The detector was the MIT mosaic, consisting of two CCDs of 2k×4k, 0.15μm pixels, binned by a factor of two.

The same NTT set-up was used to obtain phase-resolved spectra of our second target, HP Lib, on five consecutive nights starting March 6, 2004. The exposure times were 45–55 seconds and the weather conditions were again good, with a typical seeing of $1.0''$ on the first night, dropping to $0.7''$ on the subsequent nights. The wavelength calibration was done with HeAr arc exposures, in which a total of about 28 arc lines were fitted with a fourth-order Legendre polynomial, leaving 0.02 Å residuals. All spectra were again transformed to the heliocentric rest-frame. The average spectra were flux-calibrated with the standard star HD49798.

A summary of our observations is given in table 6.1.

6.3 Results

6.3.1 Average and phase-binned spectra

We caught V803 Cen in a high state on the VLT, where we measured an average magnitude of about $V = 13.0$ from our spectroscopy (see Patterson et al. (2000) for a description of V803 Cen's different brightness states). Its average spectrum shows mainly neutral helium lines in absorption (see figure 6.1), but in a trailed spectrum we find weak additional lines of Si II 6346

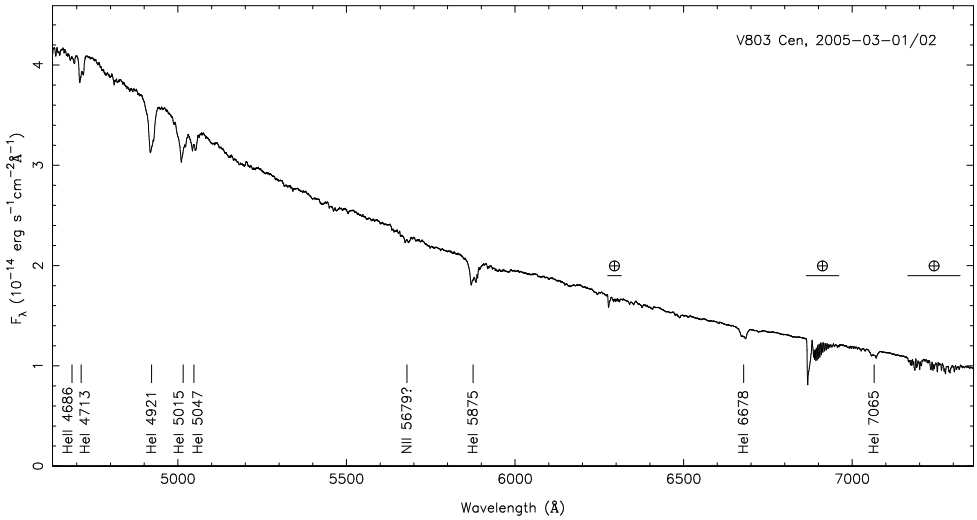

Figure 6.1: Average visual and red spectrum of V803 Cen observed with the VLT, with labels attached to the strongest features. The spectrum of the second night has been scaled up by ∼5% to match the intensity of the first night's spectrum.

and Si II 6372, also seen in other AM CVn stars (Groot et al., 2001; Roelofs et al., 2005), and two features which coincide with N II 5679 and N II 6482. There is no evidence for any hydrogen in the spectrum of V803 Cen.

On the NTT, V803 Cen was observed to be in a low state, close to $V = 17.2$, on March 9, 2004. The average spectrum shows double-peaked emission lines, characteristic of an accretion disc. The strongest lines are due to neutral helium, but He II 4686 is also clearly present and there appears to be a group of lines at 4521 Å, 4549 Å, 4583 Å and 4629 Å that may represent iron (see figure 6.2). The next night, on March 10, the star had increased in brightness by about three magnitudes, to $V = 14$, and changed from an emission-line to an absorption-line spectrum, as also shown in figure 6.2.

HP Lib has an absorption-line spectrum similar to that of V803 Cen in the high state, showing mainly neutral helium lines as well as weak emission of He II 4686 (on top of apparent broad absorption of the same line). See figure 6.3. All in all, the average spectra of HP Lib and of V803 Cen in the high state are very similar to that of AM CVn (Roelofs et al., 2006b).

6.3.2 Doppler tomography

Doppler tomography (Marsh & Horne, 1988) is a powerful technique for measuring the orbital period of interacting binaries: especially the ones that show no periodicity in broad-band photometry, and the ones that show a broad-band signal dominated by superhumps (e.g. Nelemans

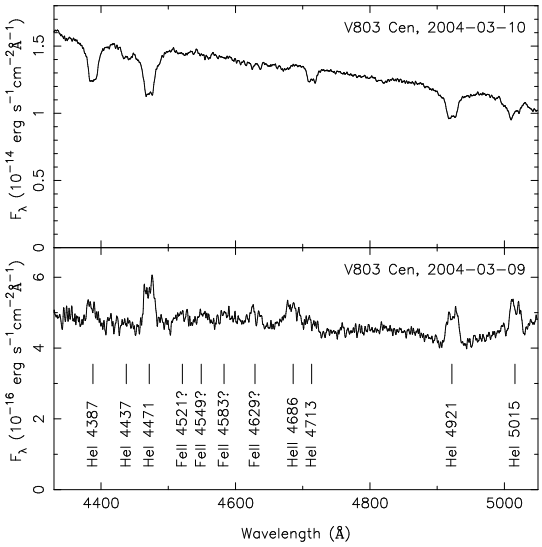

FIGURE 6.2: Average blue spectra of V803 Cen observed with the NTT.

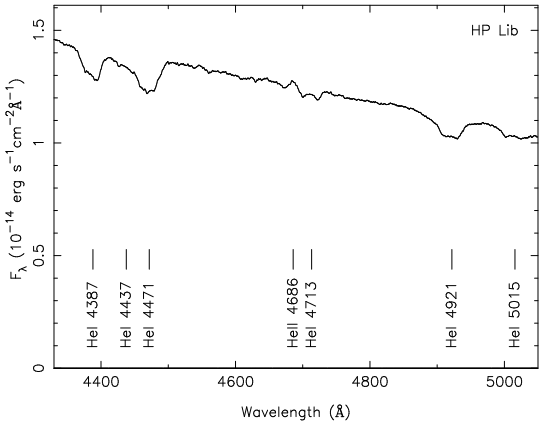

FIGURE 6.3: Average blue spectrum of HP Lib observed with the NTT.

et al. 2001). Assuming only that there is an emission region that stands out and is stationary in the binary frame, usually in the form of a 'bright spot' caused by the accretion stream–accretion disc impact point, one can track the orbital phase of the binary by tracking the phase of the emission region.

Here we apply this technique to V803 Cen and HP Lib. When we phase-fold the spectra of V803 Cen on the 1611-second period suggested from photometry, there is a persistent spot-like emission region in the Doppler tomogram throughout our VLT observing run. See figure 6.6. However, unlike in figure 6.6, its phase is seen to drift by about 180 degrees between the two nights of our observations, indicating that 1611 seconds is not exactly the orbital period *if* the feature is fixed in the binary frame.

We now assume for a moment that the emission spot seen on each of the nights is the same feature and is stationary in the binary frame over this period of time; we shall refer to it as the 'bright spot'. We can easily keep track of the bright spot's phase over the four-hour observing baseline that we have on the second night of our observations, starting from the approximate orbital period suggested from photometry, and then extrapolating to the first night without losing count of the orbital cycles. We then adjust the folding period so as to align the bright spot in the Doppler maps of both nights. This yields a spectroscopic period of 1596.4 seconds, which is also the orbital period if we assume that the bright spot is fixed in the binary frame.

We next perform a simple Monte Carlo simulation, using the bootstrap method as described in Roelofs et al. (2006a) and Roelofs et al. (2006b), in order to establish the bright spot phase resolution given by our data (at the same time, it allows us to verify that the bright spot we see is in fact a real feature rather than a coincidence of noise). We make a large ensemble of randomised Doppler tomograms from the data that we have on each night, and determine the scatter in the measured bright spot phase. We conclude that we can measure the relative bright spot phase on night 1 and night 2 to an accuracy of 5 degrees, not taking into account any intrinsic drift in the bright spot phase. If we assume that the bright spot corresponds to the conventional accretion stream–accretion disc impact point, and we allow the effective accretion disc radius to change by $0.1R_{L_1}$ between the two nights (where R_{L_1} is the distance from the centre of the accreting star to the inner Lagrange point), this adds a possible intrinsic drift of the bright spot phase in the binary frame of $\sim$10 degrees. The total error in the phasing of the bright spots is thus no more than 15 degrees. This leads to a spectroscopic period $P_{\mathrm{V803\,Cen}} = 1596.4 \pm 1.2$ s. Figure 6.6 shows the linear back-projection Doppler tomograms that we get when we phase-fold the data of each night on that period. From our Monte Carlo sample, the bright spot velocity semi-amplitude in V803 Cen is measured to be $K_{\mathrm{V803\,Cen}} = 170 \pm 15$ km/s.

Figure 6.5 shows V803 Cen's spectrogram that we obtain when we fold the data on the period obtained above. For this spectrogram we used the two hours of spectroscopy that we have on the first night, and combined it with the first and fourth hour of data from the second night in order to obtain a data-subset that is more or less evenly distributed in time. Apart from an 'S-wave' that coincides in phase and amplitude with the bright spot seen in the Doppler tomograms of figure 6.6, there is significant variability in the spectral lines on a period roughly three times

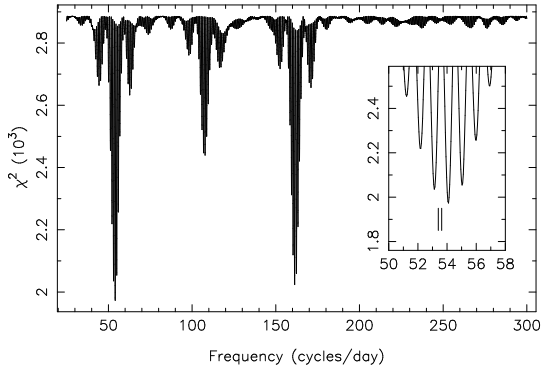

FIGURE 6.4: Chi-square values of sinusoid fits to normalised red wing/blue wing flux ratios of the helium lines in V803 Cen. The two vertical lines in the close-up indicate the 1618-second (left) and 1611-second periods known from photometry.

shorter than the S-wave period. In addition, the pattern of this variability appears to shift with time relative to the S-wave. We therefore speculate that it may be related to the superhump phenomenon. By using a data-subset that is somewhat evenly distributed in time, as described above, we find that we can minimise the amplitude of this rapid variability and maximise the visibility of the S-wave. Based on the observed changes in the pattern we speculate that it may disappear almost completely if one were to observe V803 Cen for a long time and phase-fold all the spectra (for instance if one were to fully sample the beat period between the orbital and superhump periods); this can however not be verified with our current data-set.

As a further check on V803 Cen's spectroscopic period, we compute a periodogram of the flux ratios of the red and blue wings of the spectral lines, as described in Roelofs et al. (2005) following Nather et al. (1981). We let the wings of the lines extend to $\pm$500 km/s based on the trailed spectrum of figure 6.5; for each spectrum we add up the fluxes in the red wings and in the blue wings of all the helium lines. We normalise the red/blue flux ratios such that the average ratios for the spectra taken with the different grisms and on different nights are the same; this removes the potential variability on timescales of a few hours and longer, but also weeds out the systematic differences between spectra taken with different set-ups and on different nights. Note that this also removes the influence of intrinsic, long-period skewness variations in the spectral lines, which have been seen in V803 Cen (O'Donoghue & Kilkenny, 1989) as well as in other AM CVn stars to occur on the beat period between the orbital and superhump periods (see Patterson et al. 1993). We model the flux ratios as a function of time with a constant plus a sinusoid, and compute chi-square values for the best-fitting model at each trial frequency. The resulting periodogram is shown in figure 6.4. Although, unsurprisingly, the data are poorly fitted with a constant plus a single sinusoid, shown by the large minimum reduced chi-square value of 6.7, the best-fitting sinusoidal period is $P = 1597.6$ s, in perfect agreement with the period derived from the Doppler tomograms. The nearest aliases occur at

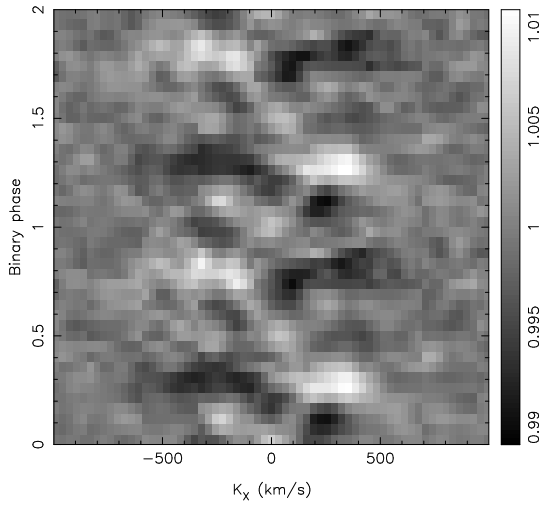

Figure 6.5: Trailed spectrum of the He I 4921, He I 5875, He I 6678 and He I 7065 lines in V803 Cen, with the average spectrum subtracted and folded on $P_{\mathrm{V803\,Cen}} = 1596.4$ s. The grey-scale indicates the flux levels relative to the mean spectrum; brighter pixels contain more flux.

$P = 1626.3$ s ($\Delta\chi^2 = 63$) and $P = 1569.8$ s ($\Delta\chi^2 = 81$).

The large $\Delta\chi^2$ values indicate that the best-fitting period fits significantly better than the next-best periods. In principle, however, these values can be inflated by underestimated errors on the data points. If we assume for a moment that our simple model should describe the data perfectly, and we renormalise the errors on the data points so as to yield a best-fitting reduced chi-square of 1, the nearest alias would have $\Delta\chi^2 = 9.5$. The best-fitting period of $P = 1597.6$ s would then still be preferred over the next-best period at the 95% confidence level (for a chi-square distribution with four degrees of freedom; see Avni 1976). This is the worst-case scenario; $\Delta\chi^2$ for the next-best period is most likely much closer to the measured value of 63 since the estimates of our errors (which are shot-noise dominated and should be fairly well-behaved) are probably not that far off.

We thus conclude that the periodogram supports the period derived from the bright spot phasing in the Doppler tomograms, although we take note of the fact that the baseline of our observations is relatively short (only 28 hours; see table 6.1), so that it will be difficult to claim the same frequency resolution in our periodogram as we have from the bright spot phasing method.

The spectrogram of HP Lib, when folded on the suggested orbital period of $P_{\mathrm{HP\,Lib}} = 1102.7$ s (Patterson et al., 2002), looks remarkably similar to that of AM CVn (Roelofs et al., 2006b); it shows relatively simple 'S-waves' in the He I 4387, He I 4471 and He I 4921 lines, as well as in the Mg II 4481 line. Like in AM CVn and other interacting binaries, the strength of the S-wave is seen to vary strongly with phase, which can be explained by a varying visibility of

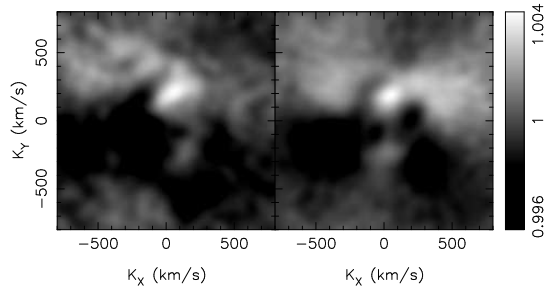

FIGURE 6.6: Linear back-projection Doppler tomogram corresponding to the trailed spectrum shown in figure 6.5, only now split into night 1 (left) and night 2 (right) to show the alignment of the bright spot. The grey-scale indicates the relative flux levels.

the accretion stream–accretion disc impact region as is expected to occur quite naturally in an inclined system. No S-waves or other structure are seen when we fold the data on the suggested 1119-second superhump period; also in this respect HP Lib is identical to AM CVn (Nelemans et al., 2001). We thus conclude that our spectroscopy supports a 1102.7-second orbital period for HP Lib.

We again perform a Monte Carlo test to determine our bright spot phase resolution and the associated error on the orbital period that we determine. To this end we make bootstrapped Doppler tomograms from the spectra of night 1 and 2, and from the spectra of night 4 and 5. The baseline between these two data-subsets is 3 nights, and the relative bright spot phase resolution is measured to be about 10 degrees. Allowing again for a 10-degree intrinsic shift in the bright spot due to changes in the effective accretion disc radius, this gives a combined bright spot phase resolution of about 15 degrees, or a resolution in orbital period of 0.2 seconds. Best alignment of the bright spots in the data-subsets is achieved for a folding period of 1102.8 seconds. Our best measurement for the period is thus $P_{\mathrm{HP\,Lib}} = 1102.8 \pm 0.2\,\mathrm{s}$.

Since the S-wave features are rather weak, we show a combined spectrogram and Doppler tomogram of the four aforementioned spectral lines in figure 6.7. The velocity semi-amplitude of the bright spot and its uncertainty, again determined from our bootstrap tests, come out at $K_{\mathrm{HP\,Lib}} = 360 \pm 20$ km/s.

6.4 Discussion & conclusions

6.4.1 The orbital periods of HP Lib and V803 Cen

If we make the (crucial) assumption that the emission features we have identified in phase-resolved spectroscopy of HP Lib and V803 Cen are (almost) stationary in the binary frame, as is the case if they correspond to the 'S-waves' or 'bright spots' commonly associated with the impact of the accretion stream into the disc, we can identify our determined spectroscopic

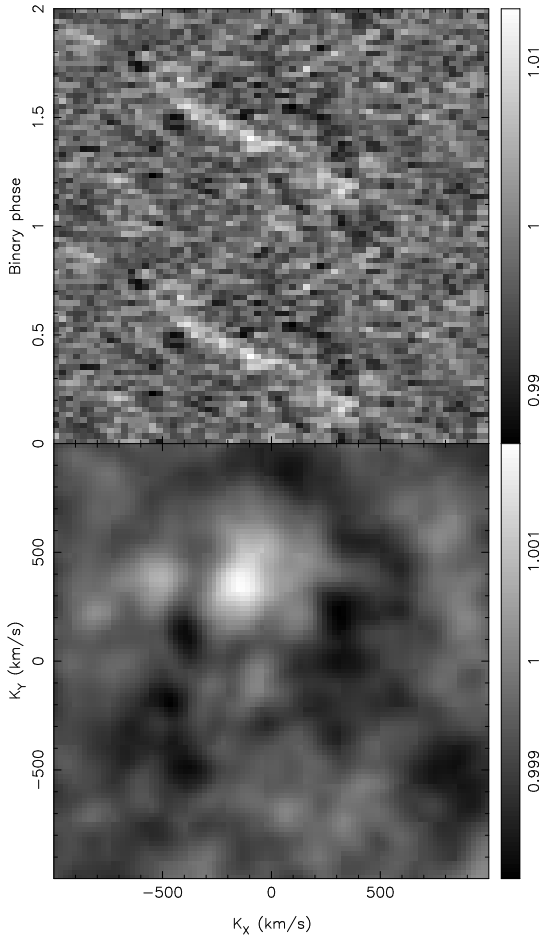

Figure 6.7: Average-subtracted trailed spectrum (top) and corresponding linear back-projection Doppler tomogram of the combined lines He I 4387, He I 4471, Mg II 4481 and He I 4921 in HP Lib, folded on $P_{\mathrm{HP\,Lib}} = 1102.8$ s. The grey-scale indicates the relative flux levels.

periods with the true orbital periods of these binaries. The orbital periods of HP Lib and V803 Cen then are $P_{\rm HP\,Lib} = 1102.8 \pm 0.2$ s and $P_{\rm V803\,Cen} = 1596.4 \pm 1.2$ s.

Our orbital period of HP Lib agrees perfectly with the value 1102.70 ± 0.05 s found in the literature, which is derived from broad-band photometry (Patterson et al., 2002). Our orbital period of V803 Cen on the other hand is significantly shorter than the literature value of 1611 ± 1 s, which is again derived from photometry (Patterson 2001; Patterson et al. 2002; but see Patterson et al. 2000 for its initial interpretation as a possible superhump). It is quite conceivable that the low inclination of V803 Cen (O'Donoghue & Kilkenny, 1989; Nasser et al., 2001) causes the photometric modulation on the orbital period to be so small, that even in extensive data-sets only superhumps are observed. We note that the velocity semi-amplitude of the bright spot in our Doppler tomograms, $K_{\rm V803\,Cen} = 170 \pm 15$ km/s, agrees with a binary of low inclination if we assume that it corresponds to the classical bright spot caused by the accretion stream–accretion disc impact ($i \sim 15°$, see also Roelofs et al. 2006c).

An interesting question would be whether our spectroscopic period of 1596.4 seconds for V803 Cen may correspond to a negative superhump, so that 1611 seconds can still be its orbital period and 1618 seconds the 'normal' (positive) superhump. Although technically possible, we consider this unlikely. The spectroscopic S-wave behaviour observed in V803 Cen is seen in many interacting binaries and has, as far as we know, always been associated with the accretion stream–accretion disc impact, rather than with a negative superhump or another feature not rotating on the orbital period. In addition, negative superhumps have not been detected in photometric studies of V803 Cen, which further weakens their case even though it does not rule out their existence.

We thus believe that the 1611-second period, observed in the intermediate and low brightness states of V803 Cen, is probably a superhump, as concluded in the original paper by Patterson et al. (2000). The same goes for the 1618-second period observed during V803 Cen's high brightness state (Patterson et al., 2000). Our spectroscopic S-wave period of $P_{\rm V803\,Cen} = 1596.4 \pm 1.2$ s is most likely the underlying orbital period of the binary. It is unclear how exactly the 1611-second period has entered the literature as the orbital period of V803 Cen. As far as we know, it first appeared in data tables in Patterson (2001) and Patterson et al. (2002), but we were unable to find a publication in which the actual detection of an orbital signal (at 1611 seconds or any other period) is claimed.

6.4.2 The superhump period excess and mass ratio

It is well known empirically, as well as from numerical modelling, that there is a correlation between the superhump period excess ϵ and the mass ratio q in Cataclysmic Variables (Patterson et al., 2005; Hirose & Osaki, 1990; Whitehurst, 1988; Whitehurst & King, 1991). Using our spectroscopic period of V803 Cen, $P_{\rm V803\,Cen} = 1596.4 \pm 1.2$ s, as the orbital period, and combining with the superhump period of 1611–1618 s measured by Patterson et al. (2000), we arrive at a superhump period excess $\epsilon_{\rm V803\,Cen} = 0.009$–$0.014$, comparable to the value $\epsilon_{\rm HP\,Lib} = 0.015$ (Patterson et al., 2002). Combined with the most recent empirical relation between

the superhump period excess and the mass ratio for the hydrogen-rich Cataclysmic Variables (Patterson et al., 2005), this would imply a mass ratio $q_{\rm V803\,Cen} = 0.05$–0.07. This is already much larger than the value $q_{\rm V803\,Cen} = 0.016$ found in the literature (e.g. Deloye et al. 2005).

If we further allow for a different scaling between the superhump period excess and the mass ratio, as measured for AM CVn itself (Roelofs et al., 2006b), we obtain an even larger mass ratio $q_{\rm V803\,Cen} = 0.08$–0.11. One could, of course, question the use of such $\epsilon(q)$ relations to derive mass ratios all too easily. The point remains, however, that there is little reason to assume that the mass ratio of V803 Cen is as extreme as previously thought, based on the orbital period that we propose here for V803 Cen.

6.4.3 Constraints on the component masses

Deloye et al. (2005) derive very stringent limits on the masses of the stars in V803 Cen based on the small mass ratio $q_{\rm V803\,Cen} = 0.016$. Basically, the minimum donor star mass is set by the mass of a cold, fully degenerate, Roche-lobe filling star, which works out to be $M_{2,\rm min} = 0.021\,M_\odot$ for a helium donor in an orbit of about 1600 seconds. This then implies a massive accretor of minimum mass $M_{1,\rm min} = 1.3\,M_\odot$. Conversely, the Chandrasekhar limit on the accretor mass implies a maximum donor star mass $M_{2,\rm max} = 0.023\,M_\odot$; in other words, there is only a very narrow range of allowed masses for the donor star. From this it is inferred by Deloye et al. (2005) that the donor star must be a cold, nearly perfectly degenerate white dwarf.

The mass ratio derived from our proposed orbital period and the associated superhump period excess relaxes these constraints almost completely, to $M_{1,\rm min} = 0.3\,M_\odot$, $M_{2,\rm max} = 0.10\,M_\odot$ for a mass ratio $q = 0.07$. It would thus seem reasonable to assume that the donor star can be much heavier than a zero-temperature white dwarf. The large observed bolometric luminosity of V803 Cen can then relatively easily be explained by a hot, semi-degenerate donor star donating matter to a much less extreme accreting white dwarf of mass $M_1 \lesssim 1.0\,M_\odot$ (see Roelofs et al. 2006c).

Chapter 7

Photometric and spectroscopic variability in the AM CVn stars SDSS J120841.97+355025.2, SDSS J141118.31+481257.6 and SDSS J124058.03–015919.2

P. J. Groot, G. H. A. Roelofs, P. A. Woudt, J. Liebert, G. Nelemans, D. Steeghs, T. R. Marsh and B. Warner

Submitted to MNRAS

Abstract. We report on the discovery of the new AM Canum Venaticorum star SDSS J120841.97+355025.2 in the Sloan Digitial Sky Survey Data Release 5. The spectrum displays strong He I emission lines on top of a blue ∼13 000 K continuum. The emission lines are triple peaked, clearly showing the 'central spike' as seen in other AM CVn systems such as GP Com, V396 Hya, SDSSJ1240–01 and AM CVn itself. We further report the determination of the likely orbital period of 46±2 minutes of another Sloan AM CVn system, SDSS J141118.31+481257.6 from time-resolved spectroscopy obtained on the MMT. The spectra of SDSS J141118.31+481257.6 also show a strong 'central spike' feature in the emission lines. Thirdly we report the detection of SDSS J1240058.03–015919.2 in March 2005 at a brightness level significantly higher than its quiescent value, the first such excursion seen in this AM CVn

star. The system appears to have been in an intermediate cycling state showing superhumps on a period slightly longer than, but not significantly different from, the orbital period.

7.1 Introduction

AM CVn stars are a small, but growing class of ultracompact binaries that consist of a white dwarf accretor and a (semi-)degenerate helium-transferring secondary. They are characterized by short orbital periods (<1 hour) and the complete lack of hydrogen in their spectra. There are currently seventeen of these systems known, excluding the two ultrashort period candidate systems HM Cnc (RX J0806+15) and V407 Vul (RX J1914+24). A recent overview of their properties is given in Nelemans (2005). They are of astrophysical significance for understanding the evolution of close compact binaries, having experienced at least one phase of common-envelope evolution (see e.g. Nelemans et al., 2001). They are also the currently only known sources above the proposed sensitivity limits of the space-borne gravitational wave mission *LISA* (e.g. Nelemans et al., 2004, Roelofs et al., 2006a,b).

Our understanding of AM CVn stars has been rapidly increasing over the last few years. On the one hand this is due to better studies of known systems (e.g. Roelofs et al. 2006c,d), and on the other hand there has been a rapid increase in the known population of objects (e.g. Warner & Woudt 2002; Woudt & Warner 2003, Roelofs et al., 2005, Woudt, Warner & Rykoff 2005; Anderson et al., 2005). With six new systems (including the one reported here) the Sloan Digital Sky Survey (SDSS; York et al., 2000) has proven to be an important resource for the discovery of new AM CVn stars.

Here we report on spectroscopic and photometric variability in three AM CVn stars that are so far little studied: the new AM CVn star SDSS J120841.97+355025.2 (hereafter referred to as SDSS J1208+35, Sect. 7.2), SDSS J1411118.31+481257.6 (Anderson et al., 2005, hereafter SDSS J1411+48, Sect. 7.3) and SDSS J1240058.03–015919.2 (Roelofs et al., 2005; herafter SDSS J1240–01, Sect. 7.4). In Sect. 7.5 we discuss our results in the context of the AM CVn population.

7.2 SDSS J1208+35

7.2.1 Spectroscopy

SDSS J1208+35 was discovered in Data Release 5 of the SDSS in a search for He I emission line objects, similar to the one performed to find SDSS J1240–01 (Roelofs et al., 2005). Fig 7.1 shows the SDSS spectrum. Clearly visible are the He I emission lines on top of a blue continuum. Table 7.1 lists the identified lines and their equivalent widths. The spectrum of

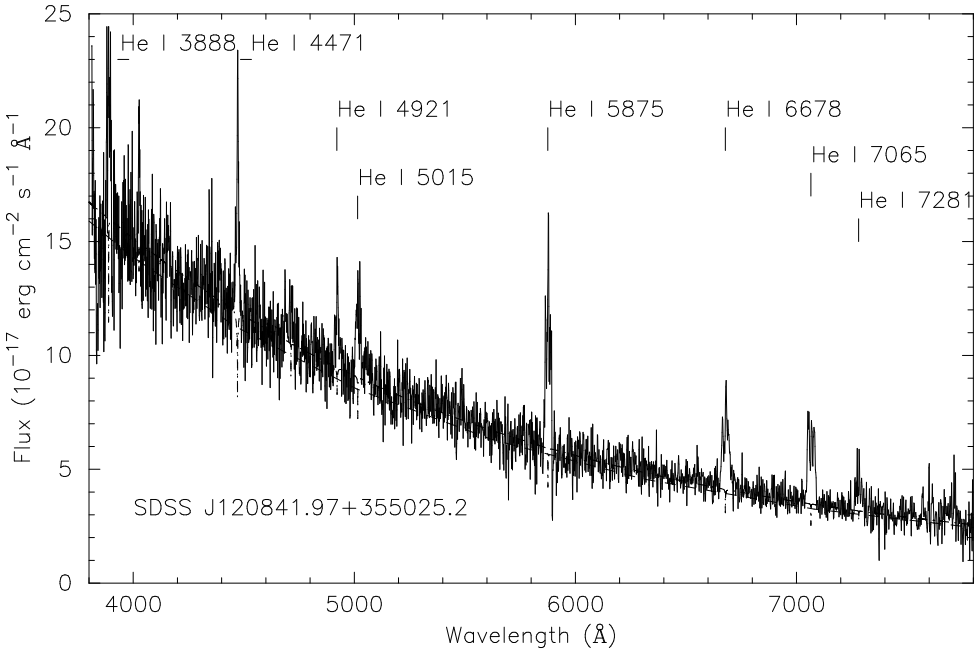

FIGURE 7.1: SDSS spectrum of SDSS J1208+35, with the strongest lines indicated. The dashed line indicates a 13 000 K blackbody scaled to the continuum of SDSS J1208+35. The dashed-dotted line shows a 12 000 K, log g=8.0 DB model scaled to the continuum.

SDSS J1208+35 is very similar to that of other members of its class, e.g. the aforementioned SDSS J1240–01 or the other AM CVn stars discovered by the Sloan survey (Anderson et al., 2005). The equivalent widths are similar or slightly stronger than e.g. SDSS J1240–01 and V406 Hya (SN2003aw; Roelofs et al., 2006c).

The blue continuum of SDSS J1208+35 is consistent with both a single blackbody temperature of $T_{BB} \sim 13\,000$ K, or with a DB white dwarf model atmosphere of the same temperature, kindly provided by D. Koester. The spectrum does not show any DB atmosphere absorption line wings as seen in e.g. V406 Hya and SDSS J1240–01, but these are also not expected at these temperatures.

The continuum temperature derived here is intermediate between SDSS J1240–01 and V406 Hya with continuum temperatures of ∼20 000 K (Roelofs et al., 2006c) and GP Com with T_{BB} ∼11 000 K (Bildsten et al. 2006).

A conspicuous feature of AM CVn stars is the presence of a very sharp emission feature overlying the more classical double peaked accretion disc profile of the emission lines. This so-called 'central spike' has been detected in GP Com (Marsh, 1999; Morales-Rueda et al., 2003), V396 Hya (Steeghs et al., in prep.), SDSS J1240–01 (Roelofs et al., 2005) and most recently in AM

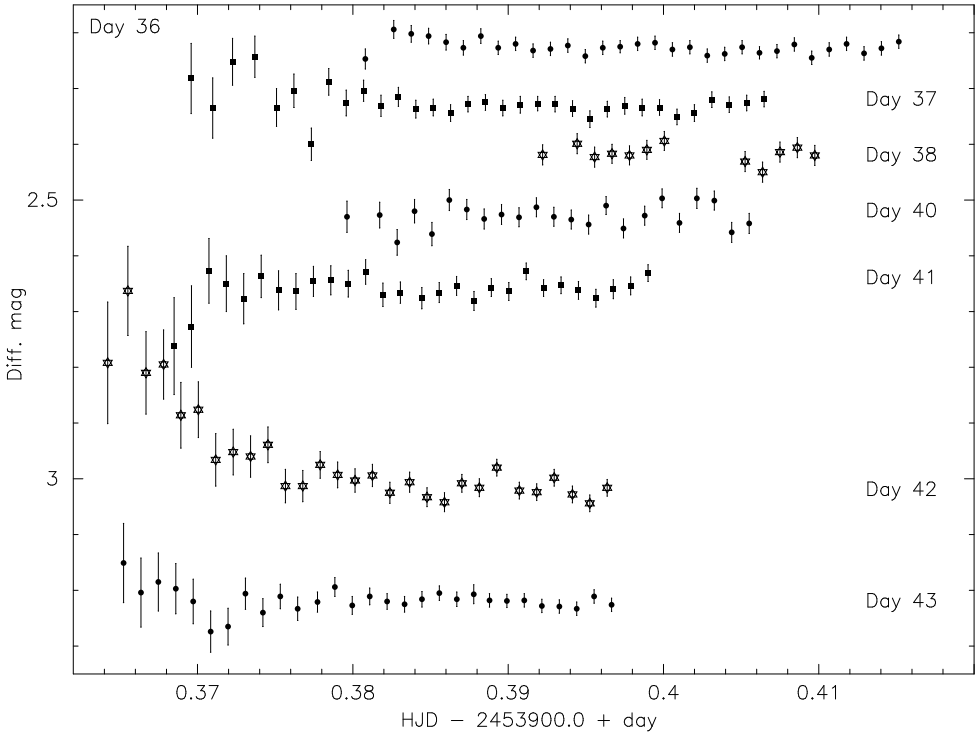

FIGURE 7.2: July 2006 INT light curve of SDSS J1208+35. Days run from top to bottom with offsets of 0.1 magnitude downwards for the days 37, 38 and 40, 0.15 mag, 0.35 and 0.2 magnitudes respectively for days 41, 42 and 43.

Spectral Line	EW (Å)
He I 3888	−10.2(5)
He I 4471	−11.4(3)
He I 4921	−7.1(5)
He I 5015	−7.9(5)
He I 5875	−34(2)
He I 6678	−29(2)
He I 7065	−37(1)
He I 7281	−19(2)

TABLE 7.1: Equivalent width of the strongest lines in SDSS J1208+35. Estimated errors are in parentheses.

CVn itself (Roelofs et al., 2006a). The persistence of this feature throughout the AM CVn orbital period range makes it one of the 'hallmarks' of the population. Its origin is poorly understood. Spectroscopic observations in GP Com, V396 Hya and AM CVn show it to have a radial velocity amplitude and phasing that is consistent with an origin on or very close to the accreting white dwarf (Morales-Rueda et al., 2003; Steeghs et al., in prep.; Roelofs et al., 2006b). The strength of the central spike in SDSS J1208+35 equals or exceeds that of the 'accretion peaks' of the classical double-peaked accretion disc profile, similar to GP Com (Morales-Rueda et al., 2003).

7.2.2 Photometry

Time-series photometry of SDSS J1208+35 was obtained on the nights of July 19-July 26, 2006 with the Wide Field Camera on the 2.5 meter Isaac Newton Telescope on the island of La Palma. The *g* filter was used with an integration time of 60 seconds. Table 7.2 shows an overview of the observations. Due to limited visibility of the object it could only be followed for ∼1 hour at the beginning of each night. Weather conditions were good, although some dust extinction due to the calima was present (especially on day 38). No observations were possible on day 39 due to high clouds. Standard overscan bias subtraction and flatfielding was performed using IRAF[1]. Object detection and aperture photometry was done using SEXTRACTOR. Differential photometry of SDSS J1208+35 was obtained using six reference stars, which were selected to be within a $11' \times 11'$ box centred on SDSS J1208+35 and being at least 2 magnitudes brighter than SDSS J1208+35. Fig. 7.2 shows the light curves of SDSS J1208+35 on the seven nights.

Fig. 7.2 shows a low-amplitude photometric variability of SDSS J1208+35. The decreasing error-bars on each night are due to the darkening of the twilight sky. A periodicity analysis of the lightcurve, excluding the first part of night 42, was performed using the PERIOD analysis package. The nightly average was first subtracted from the light curve to remove any long-term

[1] IRAF is distributed by the National Optical Astronomical Observatory under license from AURA inc.

Object	HJD (+2450000)	Length (h)	No. Exp.	Exp. Time (s)	Telescope	Phot./Spec.
SDSS J1208+35	3936.380	0.84	31	60	INT	P
SDSS J1208+35	3937.369	0.89	33	60	INT	P
SDSS J1208+35	3938.392	0.41	12	60	INT	P
SDSS J1208+35	3940.379	0.62	23	60	INT	P
SDSS J1208+35	3941.368	0.74	28	60	INT	P
SDSS J1208+35	3942.364	0.77	29	60	INT	P
SDSS J1208+35	3943.365	0.74	29	60	INT	P
SDSS J1411+48	3788.831	1.47	22	180-240	MMT	S
SDSS J1240–01	3498.213	1.72	102	60	SAAO 74-inch	P
SDSS J1240–01	3499.208	1.50	91	60	SAAO 74-inch	P
SDSS J1240–01	3499.369	1.53	93	60	SAAO 74-inch	P
SDSS J1240–01	3500.206	2.48	99	90	SAAO 74-inch	P
SDSS J1240–01	3501.389	0.77	47	60	SAAO 74-inch	P
SDSS J1240–01	3506.205	4.43	266	60	SAAO 74-inch	P

TABLE 7.2: Overview of observations of the three AM CVn stars discussed on the Isaac Newton Telescope, MMT and SAAO 74-inch telescopes

variation. A frequency range between the Nyquist frequency and one hour was searched for periodicities. A CLEAN algorithm, a Lomb-Scargle statistics and a discrete Fourier transform all returned 1108.9(1) seconds as the strongest peak, albeit at a significance too low for a definite claim of periodicity.

7.3 SDSS J1411+48

SDSS J1411+48 was one of four new AM CVn systems reported by Anderson et al. (2005) in the SDSS DR4. Its Sloan discovery spectrum shows strong He I emission lines on top of a blue continuum. To determine the orbital period of this system we obtained a set of 22 spectra on the night of Feb 22, 2006 using the Blue Channel Spectrograph on the 6.5 meter MMT at Mt. Hopkins, Arizona. Due to clouds and bad weather only ∼1.5 hours of data could be obtained. A wavelength region of 3870-5900 Å was covered using the 500 l/mm grating. A flux calibration (mainly for CCD instrumental response and not so much for an absolute flux calibration) was obtained using the flux standard Feige 34. Standard reduction procedures were performed.

Fig. 7.3 shows the average spectrum of SDSS J1411+48. Although it is qualitatively very similar to the Sloan DR4 spectrum (see Anderson et al., 2005) a few marked differences are present. The continuum of the SDSS spectrum fits best with a ∼13 000 K blackbody or a similar temperature DB white dwarf model atmosphere (see the spectrum of SDSS J1208+35 for an illustration). No absorption wings of an underlying DB atmosphere spectrum are seen (nor expected for this temperature). Our MMT spectrum appears to show a hotter (∼16 000 K) continuum

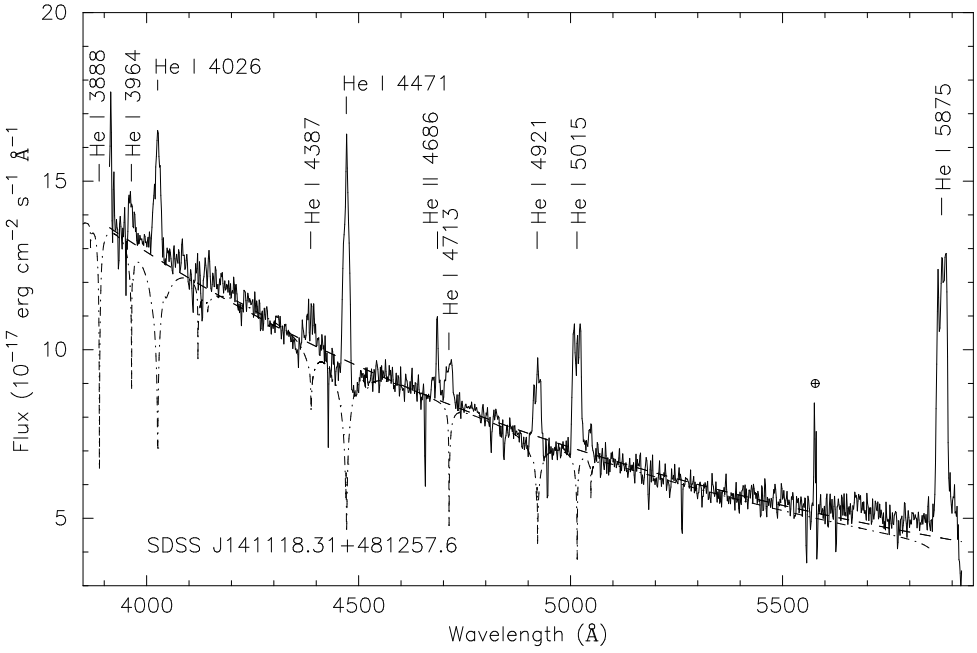

FIGURE 7.3: Average spectrum of our MMT observations of SDSS J1411+48. Major emission lines are indicated. Overplotted is a 16 000 K blackbody (dashed line) as well as a 16 000, log g = 8.0 DB Koester model (dashed-dotted line). The sharp downward spikes are caused by fluxtraps in the CCD.

temperature, as well as DB absorption line wings, best seen in He I 4921 and He I 4471. In Fig. 7.3 we overplot both a 16 000 K continuum as well as a 16 000 K, log g=8.0 DB model. Although the continuum temperature of our average MMT spectrum has a large uncertainty due to non-photometric conditions during the observations, the presence of the absorption wings points to a temperature of the accretor in SDSS J1411+48 of >15 000 K.

The central spike, which is becoming ubiquitous in many of the well-studied AM CVn systems, is also clearly visible in SDSS J1411+48, as can be seen in the He I 5015 and He I 5875 lines in Fig. 7.3.

The twenty-two individual spectra of SDSS J1411+48 were searched for periodic variations in the emission lines that may indicate the orbital period. In previous studies of AM CVn systems (see e.g. Nelemans, Steeghs and Groot, 2001; Roelofs et al. 2005, Roelofs et al., 2006a,c) the anisotropic hot-spot emission originating from where the accretion stream hits the accretion disc has served as a spectroscopic tracer of the orbital period. When correctly phased this hot-spot emission is visible as an S-wave running through a dynamic spectrum, or as a clearly defined peak in a Doppler tomogram. Both a red wing - blue wing ratio analysis as well as a 'Doppler-

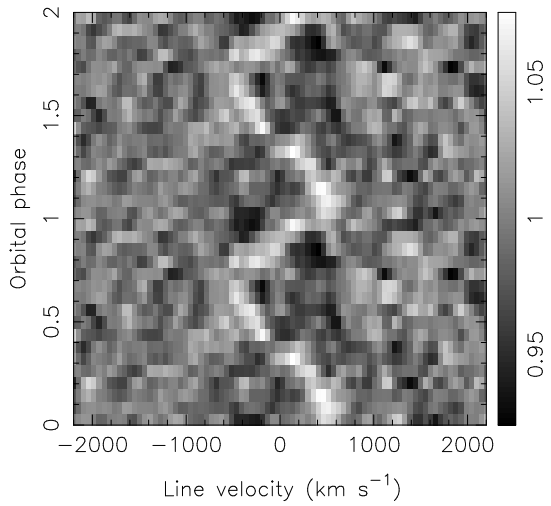

FIGURE 7.4: Trailed spectrum of the combined He I 5875, 4471, 4921 and 5015 lines, folded on the proposed orbital period of 46 minutes. A clear sinusoidal S-wave, presumably caused by the accretion stream impact is seen. The average line profile has been subtracted to enhance the visibility of the S-wave.

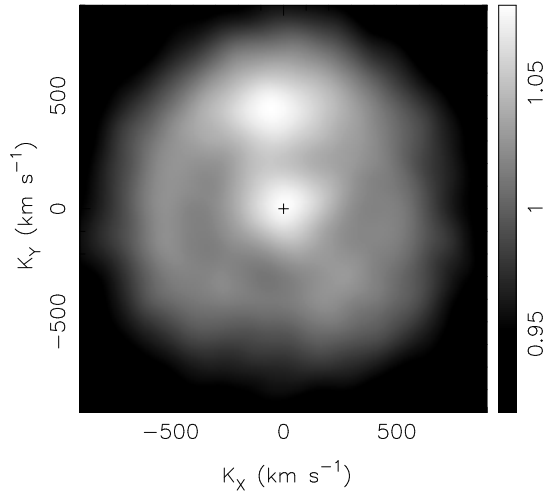

FIGURE 7.5: Backprojected Doppler map of the combined helium lines shown in Fig. 7.4, showing the three principal components of emission in this system: the accretion disc (the broad ring with radial velocities between ∼400-600 km s^{-1}), the hot-spot at a radial velocity of ∼450 km s^{-1} and the central spike near zero-velocity.

peak' analysis (see Roelofs et al., 2005) shows a strong signal at a period of 46±2 minutes, which we therefore identify with the orbital period of the system (see Fig. 7.4). The relatively large uncertainty is caused by the short time stretch of our observations (only ∼1.5 hours), and will require future refinement. Fig. 7.5 shows a combined Doppler map of the He I 5875, 5015, 4471 and 4026 lines, folded on the 46 minute period. It shows the hot-spot emission at a radial velocity of 450 km s^{-1}, and the clear presence of a central spike component, near zero velocity. Our current spectral resolution and signal-to-noise ratio are too limited to resolve the motion of the central spike, which we expect to originate close to or on the white dwarf primary, in analogy with e.g. GP Com (Morales-Rueda et al., 2003), V396 Hya (Steeghs et al., in prep.), SDSS J1240–01 (Roelofs et al., 2005) and AM CVn (Roelofs et al., 2006a).

7.4 SDSS J1240–01

SDSS J1240–01 was the first of the AM CVn stars found in the SDSS (Roelofs et al., 2004, 2005). Its spectrum shows strong triple peaked He I emission lines. The system has an orbital period of 37.36 minutes. Photometrically it had never been seen to vary from its quiescent value around V=19.7 (Roelofs et al., 2005; Woudt, Warner and Pretorius 2004). Establishing whether or not it belongs to the class of quiescent systems (GP Com and V396 Hya) or the outbursting systems is important to be able to assess at what mass-transfer rate dwarf-nova-like outbursts occur in He-dominated discs. In quiescence the optical spectrum of SDSS J1240–01 is dominated by a ∼20 000 K DB white dwarf, presumbly the accretor (Roelofs et al., 2005). Episodes of dwarf novae instabilities may keep the accretor hot through increased mass accretion onto it (Bildsten et al., 2006).

We here report the first detection of SDSS J1240–01 at a brightness well above the quiescent value. SDSS J1240–01 was observed for 5 nights in white light using the SAAO 74-inch telescope at Sutherland, SA. An overview of the observations is given in Table 7.2. Standard data reduction and analysis techniques were used as detailed in e.g. Woudt et al. (2004).

The lightcurve of SDSS J1240–01, scaled to approximate V-band magnitudes, is shown in Fig. 7.6. It is clear from this figure that SDSS J1240–01 was *not* in quiescence during the observations, but stayed rather constant at a level ∼1.7 magnitude brighter than the quiescent value (see e.g. Woudt et al., 2004). The constancy of the average level shows that it was probably caught in a so-called 'cycling' state, which is known to occur in e.g. CR Boo and V803 Cen (Patterson et al., 1997, 2000). During this state the system 'hovers' between the genuine outburst level and the quiescent state. The photometric behaviour in this cycling state is characterized by superhump variations as well as longer duration (∼1 day) variations on a level of tenths of magnitudes. This is very similar to the behaviour displayed by SDSS J1240–01 in our data set. The superhump variations are clearly visible on all nights, and the slow daily variation is most obviously seen in the light curve of the last night.

To search for short-term periodicity the data of each individual night (or stretch of night) have

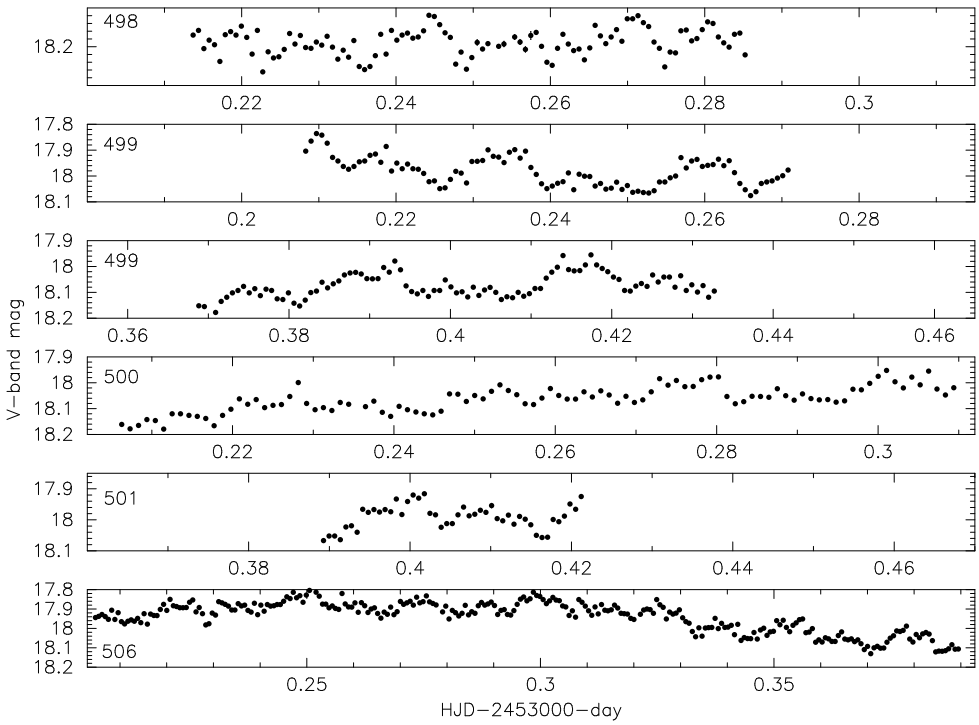

FIGURE 7.6: Light curve of SDSS J1240–01 from the observations with the SAAO 74-inch telescope in May 2005. The last three digits of the heliocentric date are used to identify the night in the upper left hand corner of each panel. Each panel shows 0.11 day, except for the bottom panel whose time-series is twice as long. Errors are plotted, but are generally smaller than the symbol.

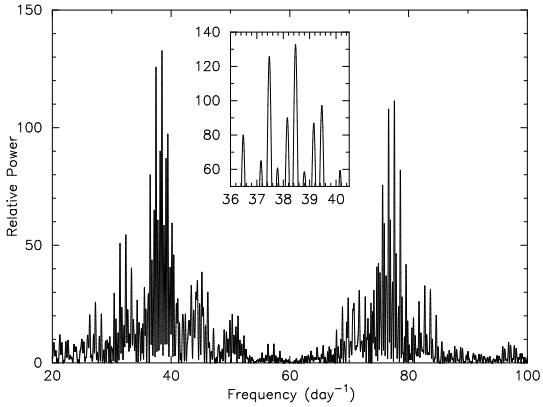

FIGURE 7.7: Fourier power spectrum of the detrended light curve of SDSS J1240–01, using the PERIOD package. The insert is a zoom-in of the region around the main peaks near 38 cycles day^{-1}.

been detrended using a polynomial of, at maximum, third order. The STARLINK PERIOD package and the EAGLE program by D. O'Donoghue were used to Fourier transform the detrended light curve, and to obtain the Lomb-Scargle and phase dispersion minimization statistics. All three techniques gave virtually identical results regarding the dominant frequencies, in each program, but a marked difference exists between the two programs. In Fig. 7.7 we show the Fourier transform of the detrended light curve over the frequency range from 20 cycles day^{-1} to 100 cycles^{-1}, as obtained with the PERIOD package. The two highest peaks are at 38.47 cycles day^{-1} (37.43 minutes) and 37.47 cycles day^{-1} (38.43 minutes). The EAGLE package provided a very similar Fourier spectrum, but the main peak is shifted to 37.55 minutes and is clearly preferred over the longer period, due to the coincidence of the next highest peaks with the harmonics of this frequency. Adopting half of the 0.12 minute shift between the determination of the highest peaks in the two packages as an error estimate we cannot make a significant distinction between the photometric period found here, 37.49±0.06 minute, and the spectroscopically determined orbital period, at 37.36 minutes (Roelofs et al., 2005). We do note that in quiescence no detection of any photometric variability was made (Woudt et al., 2004).

7.5 Discussion & Conclusions

7.5.1 The classification of SDSS J1208+35

The spectroscopic and photometric behaviour of AM CVn stars appears to be quite consistent, with a rough division in three classes (excluding the ultrashort period systems ES Cet, HM Cnc and V407 Vul). The high mass transfer rate systems (AM CVn and HP Lib) have periods $\lesssim$20 minutes and show shallow, broad absorption lines on top of a hot (T$\sim$30 000K) blue

continuum in their spectra and low-amplitude photometric variability with the main period close to, but not on the orbital period, which is generally attributed to a superhump behaviour. On the other side of the period range the systems GP Com and V396 Hya at orbital periods $\gtrsim$ 40 minutes show strong He I emission lines on a blue, T$\sim$10 000 K continuum in their spectra and no photometric variability on short or long times scales. In the orbital period range in between, the systems show both short as well as long term photometric variability. In their spectra they resemble the high-state, short-period systems when they are bright or in outburst and the low-state, long-period systems when they are faint or in quiescence.

Based on its spectrum we would classify SDSS J1208+35 as belonging to the class of systems with an orbital period longer than 20 minutes, and most likely on the longer period end of this due to its cold continuum and strong presence of the central spike. The weak photometric period at $\sim$18 minutes would be at odds with this, unless it is the first harmonic of a superhump period (as in SDSS J1240–01), which would put its orbital period around $\sim$36 minutes. However, future photometry will have to establish the reality of the $\sim$18 minute variation and future spectroscopy will have to reveal the orbital period of the system.

7.5.2 SDSS J1411+48

With an orbital period of 46$\pm$2 minutes SDSS J1411+48 would be the 'orbital twin' of GP Com. Although its spectrum resembles the low-state systems, SDSS J1411+48 shows a higher continuum temperature than GP Com, also evidenced by the presence of the DB absorption wings in the He I lines. These absorption wings only become prominent at temperatures above 15 000 K. This is the first indication that the continuum temperature in AM CVn stars is not monotonically decreasing with increasing orbital period. More detailed modelling will have to establish the reality of a temperature increase between the discovery SDSS spectrum (taken on March 17, 2005) and our MMT data slightly less than one year later. If found to be correct, it would imply that a photometric outburst took place in the time in between and thereby temporarily heating the white dwarf atmosphere by a few thousand degrees. The consequence of this would be that SDSS J1411+48 is still in the unstable region, whereas GP Com has never been seen to deviate from its quiescent photometric level. Both the higher continuum temperature (with respect to GP Com) as well as the possible presence of a photometric outburst may be a consequence of a higher mass accretor (see e.g. Fig. 2 in Bildsten et al., 2006). A more extensive spectroscopic and photometric campaign on SDSS J1411+48 will have to establish the occurrence of photometric outbursts (which are only suggested here), and to determine the orbital period as well as the temperature of an underlying DB white dwarf accretor more accurately.

7.5.3 SDSS J1240–01

The detection of SDSS J1240–01 at a photometric level well above its quiescent level implies that photometric outbursts occur up to orbital periods of a least 37 minutes. The strongest peak

in the outburst light curve corresponds with a 37.49 ±0.06 minutes period, slightly longer than the spectroscopic orbital period of 37.36 minutes. Detecting a longer photometric period is common in these systems and attributed to a slow prograde precession of a distorted accretion disc. In this scenario the orientation of the accretion disc takes slightly longer than the orbital period of the system to align itself again with the observer. However, due to the limited single-site dataset presented here, the photometric period found here is not significantly different from the spectroscopic orbital period found by Roelofs et al., 2005. Therefore, at present we cannot test the applicability in helium dominated systems of the superhump excess - mass ratio relation found for hydrogen rich systems by Patterson and co-workers (e.g. Patterson et al., 2005).

7.5.4 Conclusions

The new AM CVn star SDSS J1208+35 as found in Data Release 5 of the SDSS shows strong He I emission lines with a prominent 'central spike' on top of a blue, 13 000 K, continuum that is equally well represented by a blackbody fit as well as a DB model atmosphere. It shows short term photometric variability, but any periodicity in this needs to be confirmed.

The spectroscopic orbital period of SDSS J1411+48 is 46±2 minutes, deduced from the S-wave displayed by the hot-spot in the system. A further refinement of the orbital period was not possible due to the short time interval of our observations. SDSS J1411+48 also shows a clear central spike, which maps to zero-velocity in a Doppler tomogram. Its continuum spectrum is well represented by a 16 000 K DB white dwarf atmosphere or a blackbody spectrum of the same temperature. This continuum temperature is higher than that of GP Com, which has the same orbital period, hinting at a different evolutionary history for the two systems or a higher accretor mass in SDSS J1411+48. In our MMT spectra SDSS J1411+48 also appears to display a higher continuum temperature than in the discovery SDSS spectrum, leading to the suggestion that the system may have endured an, unseen, period of higher mass accretion in between the times of the two sets of data (see e.g. Piro, Arras & Bildsten, 2005).

We have detected SDSS J1240–01 in a state about 1.7 magnitude brighter than its quiescent level. It displayed superhump variation on a period slightly longer than, but not significantly different from, the orbital period and a cycling behaviour on a ∼1 day time scale as has been detected before in V803 Cen and CR Boo. The outburst of SDSS J1240–01 indicates that 'dwarf nova'-like outbursts occur to at least an orbital period of 37 minutes (and possibly longer if indeed SDSS J1411+48 underwent an unseen outburst). Renewed spectroscopic observations of SDSS J1240–01 may prove the ability for enhanced accretion heating during photometric outbursts to raise the atmospheric temperature in AM CVn primaries on short time scales.

Chapter 8

The population of AM CVn stars from the Sloan Digital Sky Survey

G. H. A. Roelofs, G. Nelemans and P. J. Groot

Submitted to MNRAS

Abstract. The AM Canum Venaticorum stars are rare interacting white dwarf binaries, whose formation and evolution are still poorly known. The Sloan Digital Sky Survey provides, for the first time, a sample of 6 AM CVn stars (out of a total population of 18) that is sufficiently homogeneous that we can start to study the population in some detail.

We use the Sloan sample to 'calibrate' theoretical population synthesis models for the space density of AM CVn stars. We consider optimistic and pessimistic models for different theoretical formation channels, which yield predictions for the local space density that are more than two orders of magnitude apart. When calibrated with the observations, all models give a local space density $\rho_0 = 1 - 3 \times 10^{-6}$ pc^{-3}, which is lower than expected.

We discuss the implications for the formation of AM CVn stars, and conclude that at least one of the dominant formation channels (the double-degenerate channel) has to be suppressed relative to the optimistic models. In the framework of the current models this suggests that the mass transfer between white dwarfs usually cannot be stabilized. We further explore evolutionary effects that have so far not been considered in population synthesis models, including the recent suggestion that long-period systems may be lost from the population when their donor stars cool and contract below their Roche-lobe radii, causing them to become detached white dwarf binaries with one extremely low mass component ($M_2 = 0.01 - 0.02\,M_\odot$).

8.1 Introduction

The Sloan Digital Sky Survey (SDSS; York et al. 2000) is the largest photometric and spectroscopic sky survey ever carried out, consisting of imaging in five broad-band filters (u, g, r, i, z) and follow-up spectroscopy of a large fraction of targets outside the stellar (main-sequence) locus. The first phase, SDSS-I (i.e. Data Release 5, Adelman-McCarthy et al. 2007) contains photometry of 8000 square degrees concentrated on the northern Galactic cap, down to a limiting magnitude of about $g = 22$, and spectroscopy of about 70% of that area (we shall refer to these as the 'photometric database' and the 'spectroscopic database', and we shall use the dereddened magnitudes according to Schlegel et al. (1998) throughout this paper). The spectroscopic database contains more than 1 million objects, which have been obtained in about 1700 pointings ('tiles') using a 640-fibre multi-object spectrograph. Although the spectroscopic follow-up to the imaging is mainly tailored towards finding quasars and galaxies, Galactic sources off the main sequence also make their way into the spectroscopic sample, serendipitously or sometimes targeted as white dwarfs (WDs) and hot standard stars.

Among the serendipitous targets are AM Canum Venaticorum stars: ultra-compact binaries that consist of a white dwarf accreting helium-rich matter from a (semi-)degenerate donor star. They are most easily picked up as helium-emission-line objects in the SDSS spectroscopic database. To date, six such systems have been found in the SDSS (Roelofs et al. 2005; Anderson et al. 2005; Groot et al. 2006), a significant increase in the number of systems – only 10 AM CVn stars were known prior to the SDSS, and another two were recently discovered as supernova candidates (Woudt et al., 2005; Prieto et al., 2006). The spectroscopic sample of emission-line systems from the SDSS is the first that is sufficiently large, complete, and homogeneous that a study of the AM CVn population can be attempted. Since it is still a small sample, the approach in this paper shall be to combine this observed sample with theoretical predictions for the AM CVn stars (Nelemans et al., 2001, 2004), in order to 'calibrate' the model populations.

This will hopefully give us more insight into the as yet uncertain formation and evolution of these binaries. In addition, the AM CVn stars are of particular interest for gravitational-wave astrophysics: they are the only *known* objects that can be detected with space-borne gravitational-wave detectors such as the proposed *Laser Interferometer Space Antenna (LISA)* mission (Stroeer et al., 2005; Roelofs et al., 2006c; Stroeer & Vecchio, 2006). Depending on their space density, as many as $\sim$10,000 AM CVn stars can be resolved throughout the Galaxy by a *LISA*-type instrument (Nelemans et al., 2004).

8.2 Calibrating population synthesis models for the AM CVn stars

8.2.1 Formation channels

Three formation channels have been proposed to contribute to the population of AM CVn stars. In the first of these, the 'WD channel', a close pair of detached white dwarfs is formed via two common-envelope phases, which is subsequently driven towards Roche-lobe overflow by gravitational-wave emission (e.g. Nather et al. 1981; Tutukov & Yungelson 1996; Nelemans et al. 2001). After the onset of Roche-lobe overflow at an orbital period of a few minutes, the system evolves towards longer orbital periods as the degenerate donor star expands upon mass loss.

In the second scenario, the 'He star channel', a white dwarf accretes from an initially non-degenerate helium star, while the binary evolves to shorter orbital periods. The helium burning in the core of the donor star quenches as a result of the mass loss and the system reaches an orbital period minimum around $\sim$10 minutes, at which point the donor star has become semi-degenerate and the system starts to evolve towards longer orbital periods again (Tutukov & Fedorova, 1989; Iben & Tutukov, 1991; Nelemans et al., 2001).

The third, 'evolved-CV channel' was suggested more recently by Podsiadlowski et al. (2003) and involves a Cataclysmic Variable star (CV) in which the mass transfer starts by the time the donor star starts to evolve off the hydrogen main sequence. Depending on the level of hydrogen depletion that is reached, such a system may shift its orbital period minimum from about one hour (the normal orbital period minimum for degenerate hydrogen-rich matter) down to the orbital period minimum for helium-rich matter at $\sim$10 minutes, with most such systems reaching intermediate orbital period minima due to remaining fractions of hydrogen in their cores.

The objects emerging from each of these channels are expected to look like helium-rich, ultra-compact AM CVn stars that evolve towards longer orbital periods and lower mass transfer rates, driven by angular momentum losses due to the emission of gravitational waves.

8.2.2 Recent observational & theoretical results

Bildsten et al. (2006) have recently shown that, at long orbital periods, the AM CVn stars are expected to be dominated in the optical by an accretor that cools as if it were a stand-alone white dwarf. This is due to the exponentially decreasing mass accretion rate losing control over the thermal state of the accretor, and the accretion luminosity dropping below the luminosity of the accretor. The steep decrease in mass transfer rate with orbital period, which is a consequence of the gravitational-wave losses being a steep function of orbital period, should cause the transition from disc-dominated to accretor-dominated spectra to occur over a fairly small range in orbital period. Observationally, this transition from a disc-dominated optical spectrum to an accretor-dominated spectrum is seen to occur at orbital periods of about 30 minutes, with

systems at longer orbital periods spending most of their time in a 'low' state characterized by helium emission lines from the disc and a continuum that is apparently dominated by the photosphere of the accretor, while systems at shorter orbital periods spend most of their time in a 'high' state characterized by an absorption-line spectrum dominated by the accretion disc. Two recent additions to the AM CVn family, SDSS J1240 (Roelofs et al., 2005) and 'SN 2003aw' (Woudt & Warner, 2003; Nogami et al., 2004; Roelofs et al., 2006a) at $P = 37$ and 34 min respectively, appear to spend most of their time in an emission-line state dominated by the accretor's photosphere, going into outburst not more than about once a year. Shorter-period systems such as CR Boo and V803 Cen at 25 and 27 minutes, on the other hand, spend most of their time in a high(er) state characterized by an accretion-disc-dominated absorption-line spectrum; they are seen to spend less than 10 per cent of their time in a low, emission-line state (Patterson et al., 1997, 2000).

Assuming that, statistically, there is a transition from disc-dominated to accretor-dominated spectra at $P_{\rm min} = 30$ minutes, and knowing the thermal evolution of the accretor-dominated systems, we can parameterize the colours and absolute magnitudes of all 'long-period' AM CVns at $P > 30$ min with their orbital period. This allows us to determine the completeness of spectroscopic follow-up in the SDSS as a function of orbital period, by measuring the completeness as a function of colour. If we further assume a certain orbital period distribution for the AM CVn stars based on population synthesis studies, we can convolve this distribution with the completeness as a function of orbital period to obtain the total number of emission-line AM CVn stars present in the SDSS-I, from which we can derive the surface and space densities of these stars.

Population synthesis studies of AM CVn stars have yielded predictions about their space density, but they are thought to be uncertain to two orders of magnitude (Nelemans et al., 2001, 2004). Interestingly, the distribution of orbital periods is relatively well-known; it is mainly the absolute number of systems that is uncertain. One of the important reasons for that is the fact that the angular momentum loss due to gravitational waves, which directly drives the evolution towards longer orbital periods in these systems, is a steep function of the orbital period. This causes the fraction of systems at long orbital periods ($P > 30$ min), for instance, to be very similar for different population synthesis models since the evolution from the start of Roche-lobe overflow to this long-period regime is relatively instantaneous – it takes only about 10^8 years. For all model populations the fraction of systems at short orbital periods ($P < 30$ min) is therefore $\leq 2\%$.

This allows us to calibrate the total space density of AM CVn stars based on the emission-line population in the SDSS and the predicted orbital period distributions from population synthesis studies. To assess the influence of the exact shape of the orbital period distribution, we can calculate the total space density for different model populations and see how they differ.

8.2.3 Formal method

We wish to determine the space density of emission-line AM CVn stars from the observed $N_{\rm spec} = 6$ systems in the spectroscopic database of SDSS-I. To this end we simulate observations of model populations to see how many AM CVn stars we would have found in the SDSS-I if this population corresponded to the true population. The expected number of AM CVns in the spectroscopic database is given by an integral over the sampled volume, multiplied by the modelled space density ρ' and by the completeness of spectroscopic follow-up C. The efficiency for identifying emission-line AM CVn stars once they have made their way into Sloan's spectroscopic database is assumed to be (nearly) 100%. The completeness of spectroscopic follow-up, i.e. the fraction of AM CVn stars in the photometric database of which a spectrum was taken, is expected to be far from 100%, and in addition it is expected to be a function of colour and apparent magnitude. One of our main concerns shall therefore be to determine this completeness.

We express the expected number $N'_{\rm spec}$ of emission-line AM CVn stars in the spectroscopic database of the SDSS, for a given model population, as an integral over the orbital period P and the distance d, while summing over all spectroscopic pointings (primed quantities indicate model predictions):

$$N'_{\rm spec} = \sum_{\rm tiles} \int_{P_{\rm min}}^{\infty} {\rm d}P \int_{0}^{d_{\rm max}(P)} {\rm d}d \; \Omega_{\rm tile} d^2 \; C(P, b_{\rm tile}, d) \; \rho'(P, b_{\rm tile}, d) \tag{8.1}$$

Here, $C(P, b_{\rm tile}, d)$ is the completeness of spectroscopic follow-up as a function of orbital period P (which we link to effective temperature and thus colour via a certain prescription), as a function of distance d (linked to apparent magnitude g via a certain prescription), and as a function of Galactic latitude b. We determine this completeness *a posteriori* from the Sloan spectroscopic database by counting the fractions of objects that have spectroscopic follow-up in colour, magnitude and Galactic latitude intervals. The quantity $\rho'(P, b_{\rm tile}, d)$ is the population synthesis prediction for the space density of systems as a function of orbital period, Galactic latitude and distance. The distance $d_{\rm max}(P)$ is the distance at which an object of orbital period P would have an apparent magnitude $g_{\rm max}$, where $g_{\rm max}$ is a suitably chosen magnitude limit. Finally, $\Omega_{\rm tile}$ is the solid angle covered by each spectroscopic tile (pointing), over which we take the sum to get the total area covered by the spectroscopic database. Thus the integral $\int \Omega_{\rm tile} d^2 {\rm d}d$ expresses the volume corresponding to a pointing. We will assume that the effective solid angle covered by each spectroscopic pointing is equal to $\Omega_{\rm tile} = \Omega_{\rm spec}/N_{\rm tiles}$, where $\Omega_{\rm spec} = 5700$ square degrees is the total solid angle covered by the spectroscopic database, and $N_{\rm tiles} = 1700$ is the number of spectroscopic tiles over which we take the sum.

The observed local space density ρ_0 at Galactic height $z = 0$, based on the observed $N_{\rm spec} = 6$, is then given by

$$\rho_0 = \frac{N_{\rm spec}}{N'_{\rm spec}} \rho'_0 \tag{8.2}$$

where ρ'_0 is the local space density of the model population.

The total number of emission-line AM CVn stars in the photometric database of SDSS-I down to $g = g_{\rm max}$ is obtained by setting $C(P, b_{\rm tile}, d) = 1$ in eq. 8.1 and multiplying by $\Omega_{\rm phot}/\Omega_{\rm spec}$, where $\Omega_{\rm phot} = 8000$ square degrees is the solid angle on the celestial sphere covered by the photometric database:

$$N_{\rm phot} = \frac{N_{\rm spec}}{N'_{\rm spec}} \frac{\Omega_{\rm phot}}{N_{\rm tiles}} \sum_{\rm tiles} \int_{P_{\rm min}}^{\infty} {\rm d}P \int_0^{d_{\rm max}(P)} d^2 \, {\rm d}d \; \rho'(P, b_{\rm tile}, d) \tag{8.3}$$

This value $N_{\rm phot}$ divided by the area covered by the photometric database $\Omega_{\rm phot}$ gives the surface density σ of emission-line AM CVn stars down to $g = g_{\rm max}$ at the typical Galactic latitudes covered by the SDSS-I.

8.2.4 Population synthesis models

The double-degenerate WD channel and the single-degenerate He star channel are thought to be the dominant contributors to the AM CVn population, with the evolved-CV channel contributing at the $< 2\%$ level (Nelemans et al., 2004). As in Nelemans et al. (2001) we model two scenarios for the total population of AM CVn stars, an 'optimistic' and a 'pessimistic' model, each taking into account the two dominant channels. In the optimistic model, there is a strong tidal coupling between white dwarf binaries in the WD channel, which helps to stabilize the mass transfer by feeding back angular momentum accreted by the primary star to the orbit. Furthermore, carbon-oxygen (CO) white dwarfs accreting from a He star are not easily destroyed by edge-lit detonations (ELDs) in this model. In the pessimistic model we assume no tidal coupling between white dwarfs, causing many to merge and few to survive as stably accreting AM CVn stars. In this model we furthermore include a favourable scenario for ELDs to destroy AM CVn progenitors in the He star channel, although this has only a limited effect on the number of AM CVn stars emerging from this channel. See Nelemans et al. (2001, 2004) for a more quantitative description of the two scenarios.

In order to allow for the possibility that one of these two formation channels is shut off completely for some (as yet unknown) reason, we furthermore model optimistic and pessimistic populations for each of these channels individually.

All these population synthesis models include a more or less realistic Galactic model as in Nelemans et al. (2004), which assumes a star formation rate that depends on position and time as modelled by Boissier & Prantzos (1999). All the stars that are formed are evolved using the latest version of the `SeBa` evolution code (Portegies Zwart & Verbunt, 1996; Nelemans et al., 2001, 2004). The resulting population of AM CVn stars at a distance $R = 8.5$ kpc from the Galactic centre and at time $t = 13.5$ Gyr is analysed. The only change we make to the model is that we assume a Galactic scale height of 300 pc for the AM CVn stars as in Roelofs et al. (2006c), instead of the 200 pc used in Nelemans et al. (2004). This is more appropriate for a population that is, on average, several Gyr old.

8.2.5 Practical considerations

The aforementioned parameterization of effective temperature with orbital period P, from which we derive the colours as a function of orbital period, is taken to be

$$T(P) = 19{,}000\,\mathrm{K} \times e^{-0.025(P-P_{\min})} \tag{8.4}$$

based on figure 2 of Bildsten et al. (2006), with P in minutes and $P_{\min} = 30$ min as before. From the same figure we parameterize the absolute magnitude as a function of orbital period as

$$M_g(P) = 10.5 + 0.075\,(P - P_{\min}) \tag{8.5}$$

with an estimated root-mean-square scatter of 0.5 magnitude. There are two emission-line AM CVn stars for which there is a parallax measurement: GP Com and V396 Hya. GP Com at $P = 46$ min has absolute magnitude $M_V = 11.5$ (Roelofs et al., 2006c) and V396 Hya at $P = 65$ min has $M_V = 13.3$ (J. Thorstensen, as quoted by Roelofs et al. 2006c). Both match well with the above parameterization.

For the completeness C as well as for the model population ρ' we have to construct a three-dimensional grid of values as a function of P, b and d. Since the modelled space density ρ' will (to a good approximation) only be a function of P and Galactic height $z = d\sin(b)$, this reduces to a two-dimensional grid in P and z. We bin the modelled systems with a resolution of 5 minutes in P and 50 pc in z, from which we then fetch a population density at arbitrary P and z via bilinear interpolation. To give an idea of the model population, figure 8.1 shows the number of systems as a function of orbital period P and Galactic latitude b, integrated up to $g_{\max} = 21$. At high Galactic latitudes, the population is suppressed relative to the low-latitude population as an effect of the population scale height. This suppression is stronger at short orbital periods due to the systems' higher brightness at short periods, shifting the peak in the distribution to longer-period, fainter (and thus closer) systems. We see that above $b \simeq 30°$, which is where the sky coverage of the SDSS-I is concentrated, the effect of Galactic latitude on the expected population is modest.

The completeness of spectroscopic follow-up $C(P, b, d)$ turns out to be insensitive to the Galactic latitude b over the area covered by the SDSS-I and we thus determine the completeness only as a function of colour, $u - g$ and $g - r$, and apparent magnitude, g. Colour and apparent magnitude are again linked to orbital period and distance according to eqs. 8.4 and 8.5. See figure 8.2 for the completeness as a function of colour, integrated up to $g_{\max} = 21$. To the lower left of the blackbody track in this figure we see the targeted DA white dwarfs, which deviate from blackbodies due to their strong hydrogen absorption lines, while the spectroscopic follow-up to the right of the blackbody track is mostly targeted at quasars. The six AM CVn stars from the SDSS-I are seen to lie close to the blackbody curve; we model their cooling track parallel to but very slightly offset from it, so that it runs through the middle of the bunch of observed systems. Figure 8.3 shows the completeness along the modelled cooling track as a function of apparent magnitude g. It is seen to depend strongly on apparent magnitude, and on colour in the 'cool' blackbody regime where the colours aproach the main sequence at $P \approx 70$ min. We

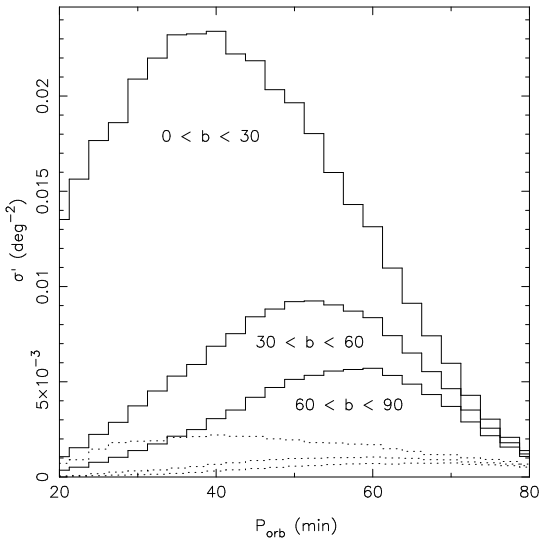

FIGURE 8.1: Modelled surface density σ' (per square degree) of AM CVn stars as a function of orbital period, down to $g = 21$, for three Galactic latitude ranges. The solid line shows the 'optimistic' model, the dotted line the corresponding 'pessimistic' model.

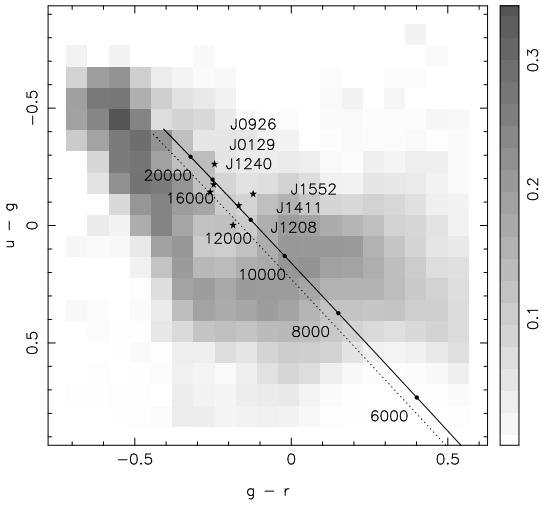

FIGURE 8.2: Completeness of spectroscopic follow-up (grey-scale) as a function of $u-g$ and $g-r$ colours, to a limiting magnitude $g = 21$. The stars indicate the known AM CVn stars from SDSS-I. The solid line is the assumed cooling track for the AM CVn stars, closely following the blackbody cooling track (dotted line). Black dots indicate the effective temperature (K).

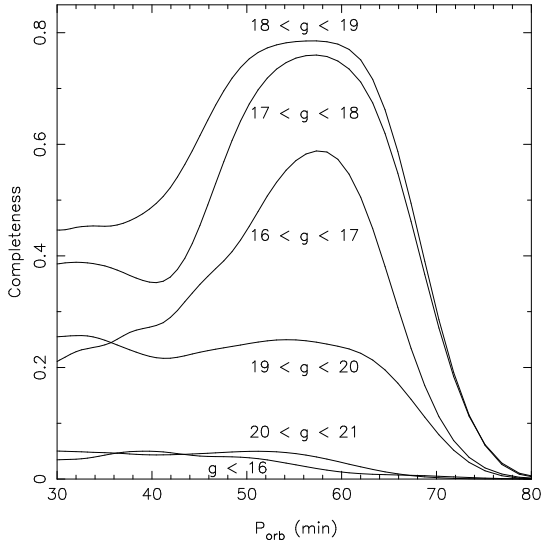

Figure 8.3: Completeness of spectroscopic follow-up $C(P, g)$ as a function of the modelled orbital period P and for different intervals in apparent magnitude g.

construct a two-dimensional grid for the completeness C in intervals of 0.5 magnitude in g and 5 minutes in orbital period P from which we again get C at arbitrary P and g via bilinear interpolation. Since the SDSS has five colour bands, $u\,g\,r\,i\,z$, the completeness of spectroscopic follow-up is not uniquely defined for each point in $(u-g, g-r)$ space, but may in principle depend on the iz colours. In the hot blackbody regime where the AM CVn stars are, however, it is unlikely that the iz colours are of much influence. We verify this by determining the completeness as a function of $r-i$ and $i-z$ for the objects in a strip along the modelled cooling track from about 20,000–10,000 K, which includes the 6 AM CVn stars found in the SDSS. It turns out to be a very flat distribution; in other words the completeness along the cooling track in $(u-g, g-r)$ is only weakly dependent on the $(r-i, i-z)$ colours of the corresponding objects.

Finally, we need to determine a suitable limit $g_{\rm max}$ to delimit a well-defined sample of AM CVn stars. We choose $g_{\rm max} = 21$ for two reasons: first, the completeness of spectroscopic follow-up in the SDSS plummets between $g = 20.5$ and $g = 21$ (see also figure 8.3), and second, up to this brightness limit we can still be confident that our efficiency for identifying emission-line AM CVn stars in the SDSS spectroscopic database is (nearly) 100%.

8.2.6 Results

Table 8.1 shows the expected number of emission-line AM CVn stars in the SDSS spectroscopic database based on the different population synthesis models. From this we obtain the 'observed'

Model	Modelled # ($N'_{\rm spec}$)	Total in SDSS-I ($N_{\rm phot}$)	Modelled ρ'_0 (pc^{-3})	Observed ρ_0 (pc^{-3})	Observed σ (deg^{-2})
Optimistic	107	52	2.6×10^{-5}	1.5×10^{-6}	6.5×10^{-3}
Pessimistic	12	67	6.2×10^{-6}	3.2×10^{-6}	8.4×10^{-3}
He star only, optimistic	16	67	8.8×10^{-6}	3.4×10^{-6}	8.4×10^{-3}
He star only, pessimistic	11	68	5.9×10^{-6}	3.3×10^{-6}	8.5×10^{-3}
WD only, optimistic	91	50	1.7×10^{-5}	1.1×10^{-6}	6.2×10^{-3}
WD only, pessimistic	0.85	57	2.4×10^{-7}	1.7×10^{-6}	7.1×10^{-3}

TABLE 8.1: Observed space densities of AM CVn stars for different assumptions regarding their populations; the observed ρ_0 is obtained by multiplying the modelled ρ'_0 by $N_{\rm spec}/N'_{\rm spec}$ where $N_{\rm spec} = 6$. 'Optimistic' and 'pessimistic' models from Nelemans et al. (2001) with the Galactic model of Nelemans et al. (2004). The total $N_{\rm phot}$ is the number of emission-line AM CVn stars in the SDSS-I photometry down to $g_{\rm max} = 21$. The measured surface density σ down to $g = 21$ holds for Galactic latitudes $b \gtrsim 30°$. The observed ρ_0 and σ are accurate to an estimated factor of 2.

local space density ρ_0 by multiplying the modelled ρ'_0 with $N_{\rm spec}/N'_{\rm spec}$ (eq. 8.2), where $N_{\rm spec} = 6$. We see that all models predict more systems than are observed, except for the pessimistic model in which additionally there are no AM CVns from the He star channel. Although the space densities in the different models vary by more than two orders of magnitude, the observed space density based on these input populations varies only by a factor of 3, from $\rho_0 = 1 - 3 \times 10^{-6}$ pc^{-3}. As mentioned in section 8.2.2, this is because the variation in the total number of systems produced in the different models is far larger than the variation in the orbital period distribution, and the latter is the only thing that causes a variation in the calibrated (observed) space density.

The uncertainties in the values in table 8.1 are dominated by the Poisson statistics of the observed sample ($N_{\rm spec} = 6$) and the uncertainties in the parameterization of the temperature and absolute magnitude with orbital period (eqs. 8.4 and 8.5). The small sample of 6 systems contributes an intrinsic uncertainty of order $6^{-1/2} \approx 40\%$ to the measured values in table 8.1. We shift the parametrization of absolute magnitude with orbital period (eq. 8.5) up and down by 0.3 magnitudes as an estimated uncertainty; this yields a variation of 32% in the observed space densities. Similarly we vary the effective temperature as a function of orbital period with $\pm 20\%$ and find a variation of 3–10% in the resulting space densities. Adding up all the numbers, we thus estimate a total uncertainty in the derived space densities that is close to a factor of 2 for each of the model populations.

Note that the pessimistic model from Nelemans et al. (2001), when calibrated with the observed systems from the SDSS, actually yields a *larger* space density than the optimistic model. This is due to the fact that the pessimistic model is dominated by AM CVns from the He star channel, which is on average a 'faster' channel that follows the star formation more closely. These systems are thus on average older and at longer orbital periods (and therefore fainter), causing the average completeness of spectroscopic follow-up to be lower and the resulting space

density to be higher.

8.3 Discussion

8.3.1 Previous space density estimates

Warner (1995) estimates a local space density $\rho_0 = 2 \times 10^{-6}\,\mathrm{pc}^{-3}$, identical to our result. Interestingly though, he arrives at this value for the wrong reasons: his estimate is essentially based on the short-period systems, and fails to take into account the large population of long-period systems that should accompany them (as mentioned before, the fraction of short-period systems is expected to be $\leq 2\%$). But this is exactly offset by his assumption that the short-period systems have an absolute magnitude $M_V = 9.5$, which from *HST* parallax measurements we now know is actually $M_V \simeq 6$ (Roelofs et al., 2006c).

The estimate for the space density based on the short-period AM CVn stars was recently updated in Roelofs et al. (2006c) based on the updated absolute magnitudes from parallax measurements, giving $\rho_0 \sim 1 \times 10^{-5}\,\mathrm{pc}^{-3}$. Although a reasonable estimate, it is uncertain due to the unknown completeness limits for the small sample of short-period AM CVns. The value found here is therefore smaller than the estimate in Roelofs et al. (2006c), but not significantly so. We note that the higher space density derived from the short-period systems, although tentative at present, is extremely interesting since it could point towards a destruction of systems during their evolution from short to long orbital periods.

8.3.2 Population synthesis results

When comparing the observed space density to the models, one has to keep in mind that there are two different factors of uncertainty in the models: (a) the formation and evolution of AM CVn stars, and (b) the Galactic model containing the position- and time-dependent star formation history. This makes it more difficult to draw conclusions about one of the two based on the observed space densities.

Fortunately the uncertainties due to the Galactic model are expected to be limited. We are looking at the local population of AM CVn stars, and what matters thus is the local star formation history, which is calibrated observationally with for instance the local stellar density, giving the integrated star formation history (Boissier & Prantzos, 1999). Inclusion of a star formation history that is a function of both time and distance from the Galactic center, versus one where the time-dependence is independent of position, has lowered the space density of AM CVn stars by a factor 2.7 (Nelemans et al., 2001, 2004). This is due to the fact that the AM CVn star progeny are relatively old populations; the delay in the star formation at $R = 8.5$ kpc relative to the centre of the Galaxy reduces the number of systems in the solar neighbourhood that have already evolved to become AM CVn stars. We estimate that the remaining room for variations in the modelled space density of AM CVn stars due to the local star formation history is less than a factor of 2.

What could further be of influence is the assumed scale height $h_z = 300$ pc of the AM CVn stars above the Galactic plane. We show in figures 8.4 and 8.5 the modelled and observed distributions in apparent magnitude g for different scale heights of $h_z = 200, 300$ and 400 pc. The effect on the total number of expected systems in the SDSS-I is clearly very small, indicating that the discrepancy between the observed and the modelled space densities is not due to the assumed scale height of the model population. Note also that the larger scale heights appear to be slightly (though not significantly) preferred based on the observed sample.

We conclude that a substantial part of the overoptimism in the 'optimistic' model (which yields a factor 18 higher space density than observed, see table 8.1) is due to the evolutionary model of the AM CVn stars. The easiest explanation is that the initial mass transfer between white dwarfs in the WD channel cannot be stabilized in the majority of cases, but rather leads to merger events (Nelemans et al., 2001; Marsh et al., 2004). The pessimistic model for the WD channel however, which assumes no stabilizing effect on the mass transfer from feedback of angular momentum due to tidal coupling between white dwarfs, yields predictions for the space density that are too low. This means that there is either a contribution from the He star channel, which by itself produces modelled space densities that are compatible with the observed value, or that there is probably some stabilizing effect due to tidal coupling in the WD channel.

The two most viable scenarios in the framework of the current models are therefore:

1. There is a mild tidal coupling between white dwarfs, which helps to stabilize the mass transfer in up to 10% of all cases in which this could work, while the He star channel is inactive;

2. The He star channel is active and there is no efficient tidal coupling between white dwarfs in the WD channel, causing the WD channel to be of negligible influence.

8.3.3 Implications for AM CVn star evolution

If we look outside the box of the current models, the relatively low number of observed emission-line AM CVn stars may most readily be explained by assuming that long-period AM CVn stars do not always exhibit the helium emission lines by which they were identified from the SDSS-I. It has been suggested from donor star model calculations (Deloye et al., 2005) that in AM CVn stars with hot, semi-degenerate donors, these donors may cool and contract, so that they no longer fill their Roche lobes. This would eliminate them from the sample studied here. Essentially, such semi-degenerate donors cool down when their (large) thermal timescale (Savonije et al., 1986; Tutukov & Fedorova, 1989) finally catches up with the (exponentially increasing) timescale of angular momentum loss from the system due to the emission of gravitational waves. Calculations of the thermal evolution of the donor stars in AM CVns (Deloye in preparation; private communication) indicate that this could happen at $P \approx 45$ min. Observationally, it has recently been found that the donor stars in short-period AM CVns ($P < 30$ min)

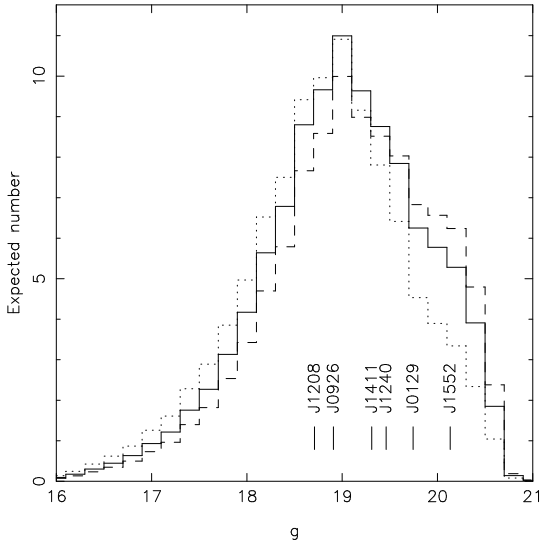

Figure 8.4: Modelled distribution of spectroscopically identifiable AM CVn stars in SDSS-I as a function of apparent magnitude g, in the *optimistic* model. The dotted, solid and dashed lines represent model population scale heights of 200, 300 and 400 pc, respectively.

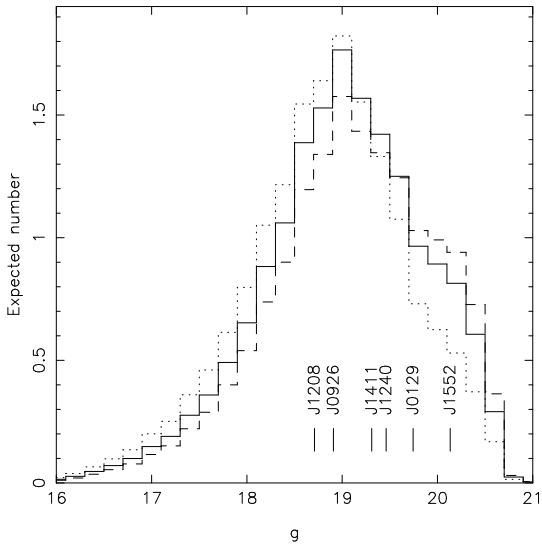

Figure 8.5: Modelled distribution of spectroscopically identified AM CVn stars in SDSS-I as a function of apparent magnitude g, in the *pessimistic* model. The dotted, solid and dashed lines represent model population scale heights of 200, 300 and 400 pc, respectively.

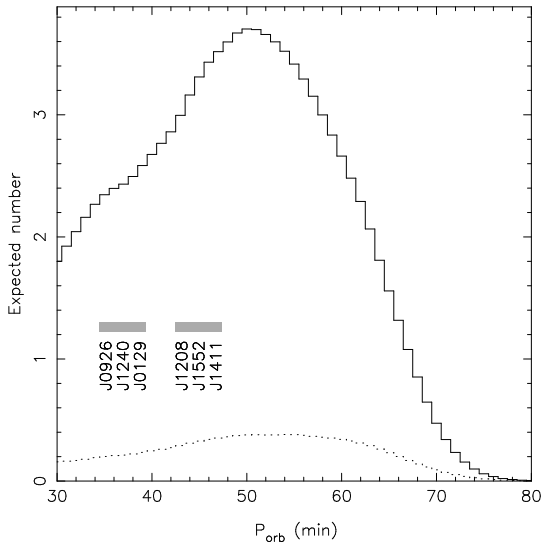

FIGURE 8.6: Modelled distribution of spectroscopically identifiable AM CVn stars in SDSS-I as a function of orbital period, along our modelled cooling track. The periods of the 6 detected AM CVns are *not* their measured orbital periods, but their modelled values based on their colours. The solid and dotted lines are the optimistic and pessimistic models, respectively.

appear to be mostly semi-degenerate (Roelofs et al., 2006c). It would thus appear that this scenario is possible.

Looking at figure 8.2 it is striking that there are no systems found at temperatures of 12,000–7,000 K, which corresponds to orbital periods $45 \lesssim P \lesssim 70$ min in our model, even though the completeness of spectroscopic follow-up in this regime is at least as large as for the hotter, shorter-period systems. Since cooler systems are also fainter, we have to fold in their brightness to get the expected orbital period distribution of AM CVn stars in the spectroscopic database of SDSS-I. This is shown in figure 8.6. The observed 'distribution' of six systems appears to be very well compatible with a fall-off of the number of systems at $P > 45$ min, but it is clear from the modelled distribution in this figure that such an effect can only explain a reduction of the observed emission-line population by at most a factor of 3. It should also be noted that the small sample of six observed systems implies that the observed distribution does not at present deviate significantly from the modelled distributions without a fall-off at $P \approx 45$ min. In addition, the orbital periods shown in figure 8.6 are those derived from the broad-band colours; orbital periods have only actually been measured for three of the six SDSS sources at present (29 minutes for SDSS J0926, 37 minutes for SDSS J1240, and 46 minutes for SDSS J1411; Anderson et al. 2005; Roelofs et al. 2005; Groot et al. 2006). The measured orbital periods are so far quite compatible with the modelled values.

The He star models take into account optimistic and pessimistic estimates for the destruction

of AM CVn stars by edge-lit detonations of the accreting CO white dwarf (Nelemans et al., 2001). Although recent studies question the existence of such ELDs altogether (e.g. Yoon & Langer 2004), their possible non-existence is irrelevant for the AM CVn population since it is of relatively little influence on the number of AM CVn stars produced in the He star channel. What could be of influence is the suggestion that the He star channel may hardly work at all due to the poor efficiency for ejecting the common envelope in such a configuration. This is thought to be due to the hydrodynamics of the relatively weak density gradient between the He burning core and its hydrogen mantle, which together form the He star progenitor (see Sandquist et al. (2000) for a study of how this may prevent the formation of low-mass ($< 0.2 M_{\odot}$) He WDs from a common envelope).

In the WD channel, the issue of the unknown tidal coupling between the accretor and the donor (Nelemans et al., 2001; Marsh et al., 2004) has been taken into account by modelling an optimistic (perfect coupling) and a pessimistic (no coupling) scenario. In the latter case, the WD channel is so much suppressed due to the mass transfer becoming unstable that the observed space density is too high for this channel to be the only contributor. An additional, relatively unstudied effect is the possible ignition of He core white dwarfs upon accretion of a substantial layer of helium from their helium white dwarf donors, either through a series of inward-moving helium flashes (Saio & Jeffery, 2000) or via an inward-moving burning front (Bildsten in preparation; private communication). Such He+He WD binaries represent up to 20% of the AM CVn star progenitors in the WD channel for the optimistic model (but note again the arguments by Sandquist et al. (2000) against the formation of low-mass He WDs in such binaries); the possible non-existence of AM CVns descending from He+He WD binaries should therefore be of limited influence. In the pessimistic model, only WD binaries of extreme mass ratio survive the initial mass transfer, leaving no AM CVn stars from He+He white dwarf binaries anyway.

With the lower space densities reported in this paper, we note that the evolved-CV channel for the formation of AM CVn stars (Podsiadlowski et al., 2003), which was previously estimated to contribute at the $< 2\%$ level (Nelemans et al. 2004), might become important. However, AM CVns from this channel should either (a) pile up more strongly at long orbital periods due to the fact that most systems are not sufficiently hydrogen-depleted to shift their orbital period minima all the way down to $\sim$10 minutes, or (b) look like 'ordinary' CVs due to their remaining hydrogen, implying that there should be many CVs with orbital periods well below one hour. Neither of that appears to be observed. Nevertheless the observational challenge of finding an AM CVn star with traces of hydrogen in its accretion disc remains.

8.3.4 Implications for the AM CVn stars as *LISA* sources

AM CVn stars are thought to be among the most important sources for future space-borne gravitational-wave detectors such as *LISA* (e.g. Nelemans et al. 2004). In addition, it is currently the only class of sources for which known, resolvable sources exist (Stroeer et al., 2005; Roelofs et al., 2006c; Stroeer & Vecchio, 2006). Current estimates for the number of AM CVn stars

resolvable with a *LISA*-type gravitational-wave detector are based on the 'optimistic' model for their formation and evolution (Nelemans et al., 2004). The results presented here suggest that these estimates are indeed a bit optimistic. If we allow for a factor of three loss of systems during their evolution from the *LISA* band ($P \lesssim 20$ min) to the emission-line regime at $P > 30$ min as discussed in the previous section, the space density measured here falls short of the optimistic model by a factor of 6. Although the possible differences between the short-period and long-period populations (if any) are far from clear at present, it would seem reasonable to lower the estimate of 10,000 Galactic AM CVn stars that can be resolved with *LISA* to about 1,000–2,000.

8.4 Conclusion

We have investigated the population of helium-emission-line AM CVn stars based on the sample of six new systems from the Sloan Digital Sky Survey. We have compared the observed sample to predicted samples as obtained from population synthesis models. For different model populations we have derived *observed* local space densities of $1 - 3 \times 10^{-6}$ pc^{-3}. In addition to the variations in observed space density for the different models, we estimate uncertainties of a factor of 2 due to Poisson noise and (assumed) uncertainties in the colours and absolute magnitudes of the emission-line AM CVn stars. In the standard evolutionary picture, where all AM CVn stars evolve to become emission-line systems at orbital periods above $\sim$30 minutes, this corresponds to a space density of the entire population that is very nearly identical to this value (within 2%).

The observed space density presented here is lower than expected from the population synthesis models, which predict 6×10^{-6} pc^{-3} for the most pessimistic to 3×10^{-5} pc^{-3} for the most optimistic models. This suggests that at least one of the proposed dominant formation channels, the double-degenerate WD channel, has to be suppressed by at least an order of magnitude compared to the optimistic models, which assume that the mass transfer between white dwarfs can be stabilized in many cases due to a strong tidal coupling of spin and orbital angular momentum. A significant effect of tidal coupling on the survival rate of AM CVns from the WD channel is possible only if the second dominant formation channel, the single-degenerate He star channel, is also severely suppressed.

We have presented an inventory of ideas, based on current theory, of how the formation channels may be suppressed relative to the models we have used. Most of these (detachment of long-period AM CVns, ignition of He+He WD accretors) have only a limited effect, but inefficient common-envelope ejection in the He star channel could potentially be effective in shutting down the He star channel completely.

Bibliography

Adelman-McCarthy J.K., et al., 2007, ApJS, submitted
Anderson S.F., et al., 2005, AJ, 130, 2230
Armitage P.J., Livio M., 1998, ApJ, 493, 898
Avni Y., 1976, ApJ, 210, 642
Benedict G.F., et al., 2002a, AJ, 123, 473
Benedict G.F., et al., 2002b, AJ, 124, 1695
Benedict G.F., McArthur B.E., 2005, IAU Colloq. 196: Transits of Venus: New views of the Solar system and the Galaxy, 333
Bergeron P., Saffer R.A., Liebert J., 1992, ApJ, 394, 228
Bessell M.S., Brett J.M., 1988, PASP, 100, 1134
Bildsten L., Townsley D., Deloye C.J., Nelemans G., 2006, ApJ, 640, 466
Boissier S., Prantzos N., 1999, MNRAS, 307, 857
Burbidge E.M., Strittmatter P.A., 1971, ApJL, 170, 39
Cardelli, J.A., Clayton, G.C., & Mathis, J.S. 1989, ApJ, 345, 245
Cox A.N., 2000, Allen's astrophysical quantities, 4th ed. Publisher: New York: AIP Press, Springer, 2000. Edited by Arthur N. Cox. (AQ2000)
Chornock R., Filippenko A.V., 2003, IAU Circular, 8084
Deloye C.J., Bildsten L, Nelemans G., 2005, ApJ, 624, 934
El-Khoury W., Wickramasinghe D., 2000, A&A, 358, 154
Elvius, M., 1975, A&A, 44, 117
Espaillat C., Patterson J., Warner B., Woudt P., 2005, PASP, 117, 189
Goodchild S., Ogilvie G., 2006, MNRAS, 368, 1123
Greenstein J.L., Matthews M.S., 1957, ApJ, 126, 14
Groot P.J., Nelemans G., Steeghs D., Marsh T. R., 2001, ApJL, 558, 123
Groot P.J., Roelofs G.H.A., Woudt P., Nelemans G., Liebert J., Steeghs D., Marsh T.R., 2006, MNRAS, submitted
Harvey D.A., Skillman D.R., Kemp J., Patterson J., Vanmunster T., Fried R.E., Retter A., 1998, ApJ, 493, 105
Hirose M., Osaki Y., 1990, PASJ, 42, 135
Horne K., 1985, MNRAS, 213, 129

Hulse R.A., Taylor J.H., 1975, ApJ, 195, 51
Humason M.L., Zwicky F., 1947, ApJ, 105, 85
Iben I.Jr., Tutukov A.V., 1991, ApJ, 370, 615
Iben I.Jr., Tutukov A.V., Fedorova A.V., 1998, ApJ, 503, 344
Larson S.L., Hiscock W.A., Hellings R.W., 2000, Phys. Rev. D, 62, 062001
Lubow S.H., Shu F.H., 1975, ApJ, 198, 383
Lubow S.H., Shu F.H., 1976, ApJL, 207, 53
Israel G.L. et al., 2002, A&A, 386L, 13
Landau L.D., Lifschitz E.M., 1971, The Classical Theory of Fields. Addison-Wesley, Reading, MA
Lutz T.E., Kelker D.H., 1973, PASP, 85, 573
Marsh T.R., Horne K., 1988, MNRAS, 235, 269
Marsh T.R., 1999, MNRAS, 304, 443
Marsh T.R., Horne K., Rosen S., 1991, ApJ, 366, 535
Marsh T.R., Nelemans G., Steeghs D., 2004, MNRAS, 350, 113
Marsh T.R., Duck S.R., 1996, New Astron., 1, 97
Marsh T.R., Steeghs D., 2002, MNRAS, 331, 7
McArthur B.E., et al., 2001, ApJ, 560, 907
Morales-Rueda L., Marsh T.R., Steeghs D., Unda-Sanzana E., Wood J.H., North R.C., 2003, A&A, 405, 249
Nasser M.R., Solheim J.-E., Semionoff D.A., 2001, A&A, 373, 222
Nather R.E., Robinson E.L., Stover R. J., 1981, ApJ, 224, 269
Nelan E., Makidon R., in HST Data Handbook, version 4.0, ed. B. Mobasher, Baltimore, STScI
Nelemans G., Steeghs D., Groot P.J., 2001, MNRAS, 326, 621
Nelemans G., Portegies Zwart S.F., Verbunt F., Yungelson L.R., 2001, A&A, 368, 939
Nelemans G., Yungelson L.R., Portegies Zwart S.F., 2004, MNRAS, 349, 181
Nelemans G., Jonker P. G., Marsh T. R., van der Klis M., 2004, MNRAS, 348, 7
Nelemans G., 2005, in ASP Conf. Ser. 330, The Astrophysics of Cataclysmic Variables and Related Objects, ed. J.-M. Hameury & J.-P. Lasota (San Francisco: ASP), 27
Nelemans G., et al., 2005, A&A, 440, 1087
Nogami D., Monard B., Retter A., Liu A., Uemura M., Ishioka R., Imada A., Kato T., 2004, PASJ, 56L, 39
O'Donoghue D., Menzies J.W., Hill P.W., 1987, MNRAS, 227, 347
O'Donoghue D., Kilkenny D., 1989, MNRAS, 236, 319
O'Donoghue D., et al., 1990, MNRAS, 245, 140
O'Donoghue D., Kilkenny D., Chen A., Stobie R.S., Koen C., Warner B., Lawson W.A., 1994, MNRAS, 271, 910
Paczynski B., 1967, AcA, 17, 287
Paczynski B., 1976, in Eggleton P., Mitton S., Whelan J., eds, Structure and Evolution of Close Binary Systems. Kluwer, Dordrecht, p. 75
Panei J.A., Althaus L.G., Benvenuto O.G., 2000, A&A, 353, 970

Patterson J., 2001, PASP, 113, 736
Patterson J., Walker S., Kemp J., O'Donoghue D., Bos M., Stubbings R., 2000, PASP, 112, 625
Patterson J., et al., 1997, PASP, 109, 1100
Patterson J., et al., 2002, PASP, 114, 65
Patterson J., Sterner E., Halpern J.P., Raymond J.C., 1992, ApJ, 384, 234
Patterson J., Halpern J., Shambrook A., 1993, ApJ, 419, 803
Patterson J., et al., 2005, PASP, 117, 1204
Pearson K.J., 2003, MNRAS, 346, L21
Podsiadlowski Ph., Han Z., Rappaport S., 2003, MNRAS, 340, 1214
Portegies Zwart S.F., Verbunt F., 1996, A&A, 309, 179
Prendergast K.H.. Burbidge G.R., 1968, ApJ, 151, 83
Prieto J., Anderson S., Becker A., Marriner J., Sako M., Jha S., 2006, Central Bureau Electronic Telegrams, 692, 1
Provencal et al., 1995, ApJ, 445, 927
Ramsay G., Hakala P., Cropper M., 2002, MNRAS, 332L, 7
Rappaport S.A., Joss P.C., 1984, ApJ, 283, 232
Roelofs G.H.A., Groot P.J., Steeghs D., Nelemans, G., 2004, Proc. IAU Coll. 194, Compact Binaries in the Galaxy and Beyond, Rev. Mex. AA, 20, 254
Roelofs G.H.A., Groot P.J., Marsh T.R., Steeghs D., Barros S.C.C, Nelemans G., MNRAS, 361, 487
Roelofs G.H.A., Groot P.J., Marsh T.R., Steeghs D., Nelemans G., 2006a, MNRAS, 365, 1109
Roelofs G.H.A., Groot P.J., Marsh T.R., Steeghs D., Nelemans G., 2006b, MNRAS, 371, 1231
Roelofs G.H.A., Groot P.J., Benedict F., McArthur B., Steeghs D., Marsh T.R., Morales-Rueda L., Nelemans G., 2006c, ApJ, submitted
Roelofs G.H.A., Groot P.J., Nelemans G., Marsh T.R., Steeghs D., 2006d, MNRAS, submitted
Ruiz M.T., Rojo P.M., Garay G., Maza J., 2001, ApJ, 552, 679
Saio H., Jeffery C.S., 2000, MNRAS, 313, 671
Sandquist E.L., Taam R.E., Burkert A., 2000, ApJ, 533, 984
Savage B.D., Mathis J.S., 1979, Ann. Rev. Astron. Astrophys., 17, 73
Savonije G.J., de Kool M., van den Heuvel E.P.J., 1986, A&A, 155, 51
Schlegel D.J., Finkbeiner D.P., Davis M., 1998, ApJ, 500, 525
Schmidt M., 1975, ApJ, 202, 22
Simpson J.C., Wood M.A., 1998, ApJ, 506, 360
Skillman D.R., Patterson J., Kemp J., Harvey D.A., Fried R.E., Retter A., Lipkin Y., Vanmunster T., 1999, PASP, 111, 1281
Soderblom D.R., Nelan E., Benedict G.F., McArthur B., Ramirez I., Spiesman W., Jones B.F., 2005, AJ, 129, 1616
Solheim et al., 1998, A&A, 332, 939
Smak J., 1967, Acta Astron., 17, 255
Smak J., 1975, Acta Astron., 25, 227
Steeghs D., Harlaftis E.T., Horne K., 1997, MNRAS, 290, 28

Stroeer A., Vecchio A., Nelemans G., 2005, ApJ, 633, 33
Stroeer A., Vecchio A., 2006, Class. Qu. Grav., 23, 809
Thorstensen J.R., 2003, AJ, 126, 3017
Timpano S.E., Rubbo L.J., Cornish N.J., 2006, Phys. Rev. D, 73, 122001
Tsugawa M., Osaki Y., 1997, PASJ, 49, 75
Tutukov A.V., Fedorova A.V., 1989, Soviet Astron., 33, 606
Tutukov A.V., Yungelson L., 1996, MNRAS, 280, 1035
van Altena W.F., Lee J.T., Hoffleit E.D., 1995, Yale Parallax Catalog (4th ed.; New Haven, CT: Yale Univ. Obs.) (YPC95)
Warner B., Robinson E.L., 1972, MNRAS, 159, 101
Warner B., Woudt P. A., 2002, PASP, 114, 129
Warner B., 1995, Cataclysmic Variable Stars. Cambridge Univ. Press, Cambridge
Whitehurst R., 1988, MNRAS, 232, 35
Whitehurst R., King A., 1991, MNRAS, 249, 25
Wood M.A., et al., ApJ, 1987, 313, 757
Wood-Vasey W.M., Aldering G., Nugent P., Li K., 2003, IAU Circular, 8077
Woudt P. A., Warner B., Rykoff E., 2005, IAU Circular, 8531, 3
Woudt P.A., Warner B., 2004, MNRAS, 351, 1051
Woudt P.A., Warner B., 2003, MNRAS, 345, 1266
Woudt P.A., Warner B., 2002, MNRAS, 328, 159
Yoon S.-C., Langer N., 2004, A&A, 419, 654
York D.G., et al., 2000, AJ, 120, 1579
Zapolsky H. S., Salpeter E. E., 1969, ApJ, 158, 809